Transient Liquid-Phase Infiltration of a Powder-Metal Skeleton

by

Adam Michael Lorenz

B.S., Mechanical Engineering
Cornell University, 1996

M.S., Mechanical Engineering
Massachusetts Institute of Technology, 1998

Submitted to the Department of Mechanical Engineering
in Partial Fulfillment of the Requirements for the Degree of
Doctor of Philosophy in Mechanical Engineering

at the

Massachusetts Institute of Technology
June 2002

Signature of Author: .....
Department of Mechanical Engineering

Certified by: .....
Emanuel Sachs
Fred Fort Flowers '41 and Daniel Fort Flowers '41
Professor of Mechanical Engineering

Certified by: .....
Samuel Allen
POSCO Professor of Physical Metallurgy

Accepted by: .....
Ain Sonin
Chairman, Department Committee on Graduate Students

Transient Liquid-Phase Infiltration of a Powder-Metal Skeleton

by

Adam Michael Lorenz

Submitted to the Department of Mechanical Engineering on May 24, 2002
in Partial Fulfillment of the Requirements for the Degree of
Doctor of Philosophy in Mechanical Engineering

ABSTRACT

Transient Liquid-Phase Infiltration (TLI) is a new method for densifying a powder-metal skeleton that produces a final part of homogeneous composition without significant dimensional change, unlike traditional infiltration and full-density sintering. Fabrication of direct metal parts with complex geometry is possible using TLI in conjunction with Solid Freeform Fabrication (SFF) processes such as Three-Dimensional Printing, which produce net-shape skeletons of powdered metal directly from CAD models. The infiltrant used in TLI is typically composed of the skeleton material plus a melting point depressant in order to facilitate homogenization after the liquid metal fills the void space. Parts over 20 cm tall with final compositions of Ni–4wt%Si and Ni–40wt%Cu were made by TLI from powder skeletons of pure nickel. Tensile tests after HIP treatment compared favorably with cast material of the same composition.

A basic understanding of the materials system requirements for TLI and the role of various parameters was developed using nickel–silicon and nickel–copper as test cases. Upon introduction of the liquid infiltrant to the skeleton, the melting point depressant begins to diffuse into the skeleton causing isothermal solidification of the infiltrant. This solidification chokes the flow of liquid and can limit the infiltration distance. A capillary-driven fluid flow model was developed to predict the infiltration rate and freeze-off limit based on a variable permeability. The rate of diffusional solidification was measured via quenching experiments, compared to theory and simulations, and subsequently used to define the change in permeability of the skeleton. For various skeletons of powder sizes ranging from 60 to 300 μm, the infiltration rate was measured via mass increase and compared to the flow model. The predicted horizontal infiltration freeze-off limits were proportional to the square root of $d^3\gamma / \mu D\beta^2$ where d is the average powder diameter, γ and μ are the infiltrant surface tension and viscosity, D is the solid diffusivity, and β is a function of the solidus and liquidus concentrations. These relations can be used for selection of processing parameters and for development of new material systems.

Thesis Supervisor: Emanuel M. Sachs
Title: Fred Fort Flowers '41 and Daniel Fort Flowers '41 Professor of Mechanical Engineering

Acknowledgments

Working with professors Ely Sachs and Sam Allen has been a privilege and their guidance has been critical to the success of this work. In addition, professors Mert Flemings and Yet-Ming Chiang were very helpful in discussing some finer points of solidification processes.

Several fellow graduate students have graciously provided assistance on the project, specifically Vinay Prabhakar conducted some of the oil permeametry and infiltration tests, Calvin Yuen and Ratchatee (Ae) Techapiesancharoenkij provided the Thermo–Calc data, and Lukas Rafflenbeul was helpful in preparing some samples. In addition, Jeanie Cherng was always a good neighbor to bounce ideas off.

Toby Bashaw was especially helpful in melting custom alloys in the MIT foundry.

Gerry Wentworth and Mark Belanger in the LMP machine shop were always helpful with various fabrication projects.

Financial support for this work was provided by the Office of Naval Research, under Contract #N00014-99-1-1090.

Jim Serdy, Laura Zaganjori and the rest of the folks in the 3DP lab have been great to work with over the years. It has truly been a pleasure!

Table of Contents

ABSTRACT **2**

ACKNOWLEDGMENTS **3**

TABLE OF CONTENTS **4**

LIST OF FIGURES **6**

LIST OF TABLES **8**

CHAPTER 1: INTRODUCTION **9**

1.1 Background 9

1.2 Description of Transient Liquid-Phase Infiltration 10

1.3 Important issues for TLI 11

1.3.1 Materials selection *12*

1.3.2 Infiltration distance limits due to freeze-off *13*

1.3.3 Erosion *14*

1.3.4 Uniformity of composition throughout the part *14*

1.3.5 Final microstructure and mechanical properties *14*

1.4 Review of related research 14

CHAPTER 2: DIFFUSIONAL SOLIDIFICATION THEORY **17**

2.1 Solidification theory by mass transport 17

2.1.1 Fick's laws and diffusivity *17*

2.1.2 Diffusional solidification and solution of the moving-interface problem *18*

2.1.3 Material system characteristics controlling solidification rate *21*

2.2 Numerical simulation 23

2.2.1 General description and effect of finite boundary conditions *23*

2.2.2 Diffusivity variation with composition *25*

2.2.3 Extension to cylindrical and spherical coordinates *29*

2.3 Free energy release during solidification and homogenization 31

2.4 Uniform composition throughout the final part 35

CHAPTER 3: EXPERIMENTAL RESULTS AND DISCUSSION **39**

3.1 Diffusion couple to verify diffusivity 39

3.2 Measurement of solidification rate 40

3.2.1 Quenching experiments to observe solidification *40*

3.2.2 Quantification of the solidification rate *44*

3.2.3 Discussion of observed solidification rate *45*

3.2.4 Relating observed eutectic width to original liquid width *47*

3.3 Gated infiltration 48

3.4 Erosion and melt saturation methods 49

3.5 Measurement of variation in composition 53

3.6 General dependence of penetration distance with powder size 53

3.7 Homogenization, porosity and mechanical testing 54
3.7.1 Homogenization 54
3.7.2 Residual porosity and measurement of density 55
3.7.3 Tensile test results and HIP Treatment 57

CHAPTER 4: INFILTRATION OF LIQUID INTO POROUS MEDIA 59
4.1 Surface tension and capillarity 59
4.2 Viscous flow and permeability 60
4.2.1 General theory of flow in porous media 60
4.2.2 Liquid flow model 62
4.2.3 Permeability prediction based on pore geometry 62
4.3 Infiltration model incorporating freezing 63
4.3.1 Growth of a sphere within a unit cell 63
4.3.2 Change in permeability 65
4.3.3 Numerical simulation of infiltration rate with variable permeability 67

CHAPTER 5: INFILTRATION RATE RESULTS AND ANALYSIS 71
5.1 Oil permeametry 71
5.2 Oil infiltration and comparison with flow model 73
5.3 Fluid properties of liquid metal 75
5.3.1 Density 75
5.3.2 Surface tension 76
5.3.3 Viscosity 76
5.3.4 Summary 77
5.4 Experimental setup for measuring liquid metal infiltration rate 77
5.5 Dipping experiments to measure local permeability change 80
5.6 Infiltration rate curves and analysis 83
5.7 Implications of the TLI rate model 89

CHAPTER 6: CONCLUSIONS 92
6.1 Overview 92
6.2 Materials conclusions 92
6.3 Infiltration limits from freeze-off 94
6.4 Recommendations for future work 97

APPENDICES 102
Appendix A: Matlab M-file simulation of diffusional solidification 102
Appendix B: Matlab M-file of liquid flow model using variable permeability 104
Appendix C: Properties of Multitherm 503 heat transfer oil 107
Appendix D: Preparation for sintered skeletons of well-defined void fraction 108
Appendix E: Physical properties of liquid metals at melting point[13] 109
Appendix F: Viscosity measurement of liquid metal by capillary method 110

BIBLIOGRAPHY 113

List of Figures

Figure 1.1: Densification of metal powder skeletons made by Three-Dimensional Printing..... 9

Figure 1.2: Generic equilibrium phase diagram with labeled components of TLI..... 11

Figure 1.3: Schematic illustration of the stages of Transient Liquid-Phase Infiltration..... 11

Figure 1.4: Infiltration of a powder skeleton with simultaneous diffusional solidification. 13

Figure 2.1: Schematic of the moving interface problem. 19

Figure 2.2: Dependence of the solidification rate coefficient β on concentration ratio. 21

Figure 2.3: Equilibrium phase diagrams for Ni–Si and Ni–Cu 22

Figure 2.4: One-dimensional diffusional solidification of Ni–Si at 1185°C with finite (simulation) and semi-infinite (analytical) boundary conditions..... 24

Figure 2.5: Decrease in solidification rate due to finite boundary conditions at long time..... 25

Figure 2.6: Numerical simulation of diffusional solidification in Ni–Cu at 1100°C using a concentration dependent diffusivity. 26

Figure 2.7: Numerical simulation of diffusional solidification in Ni–Cu at 1200°C using a concentration dependent diffusivity. 27

Figure 2.8: Effective diffusivity controlling interface motion for Ni–Cu infiltrations. 28

Figure 2.9: Comparison of diffusional solidification for planar, cylindrical and spherical geometry. 29

Figure 2.10: Interface motion for diffusional solidification with curved interface geometry. 30

Figure 2.11: Deviation distance from planar interface motion for diffusional solidification with curved interface geometry. 31

Figure 2.12: Determination of equilibrium phase based on Gibbs free energy. 32

Figure 2.13: Enthalpy for a binary mixture of Ni–Si at 1185°C used to determine heat released during solidification and homogenization. 33

Figure 2.14: Schematic of TLI into a capillary channel explaining how melt saturation ensures uniform bulk composition. 36

Figure 2.15: Ternary phase diagrams of Ni–Cr–Si and Ni–Fe–Si illustrating how solidification can result in a change of composition in remaining liquid. 37

Figure 3.1: Microprobe analysis of diffusion couple for 1 hr at 1200°C and estimated $\widetilde{\boldsymbol{D}}$ 39

Figure 3.2: Schematic of quenching experiments designed to observe diffusional solidification rate. 40

Figure 3.3: Ni powder infiltrated with Ni–Si at 1180°C and quenched. 41

Figure 3.4: Ni wire bundles infiltrated with Ni–Si at 1180°C and quenched..... 42

Figure 3.5: Microprobe concentration measurements of wire bundle quenching tests. 44

Figure 3.6: Estimation of solidification rate coefficient from interface motion in quenched samples. 45

Figure 3.7: Generic phase diagram used to relate eutectic width to liquid width..... 48

Figure 3.8: This large rectangular part composed of 50-150 μm powder was made in March of 2000 as a proof of concept for TLI. 49

Figure 3.9: Erosion of part on left caused by dissolution of skeleton material by unsaturated melt pool. Part on right shows no evidence of erosion infiltrated using saturated liquid, with some dendrites stuck to the part from the semi-solid infiltrant pool. 50

Figure 3.10: Presaturation of infiltrant supply to prevent dissolution. 51

Figure 3.11: Reduced part erosion through better mixing of infiltrant. 51

Figure 3.12: Set of infiltrated nickel powder skeletons showing more erosion on skeletons of smaller powder size. 52

Figure 3.13: Infiltrated part sectioned and tested for compositional variation. 53

Figure 3.14: Infiltration heights achieved using progressively larger powder sizes 54

Figure 3.15: Homogenization of 250–300 μm infiltrated powder. 55

Figure 3.16: Microprobe analysis of homogenization in samples from previous figure. 55

Figure 3.17: Tensile bars of homogenized Ni – 4 wt% Si after elongation and failure. 58

Figure 4.1: Influence of inertial body forces on flow through porous media given by the Forchheimer extension of Darcy's Law. 61

Figure 4.2: Growth of sphere of radius r within cubic unit cell with side length equal to the initial sphere diameter, $2R_o$. 64

Figure 4.3: Volume fraction v_f, normalized surface area to volume ratio S, and normalized permeability K as a function of sphere growth (solidification) in a simple cubic unit cell. .. 65

Figure 4.4: Predictions of $K(t)$ during skeleton solidification (D=100 μm, β=1, $\widetilde{\boldsymbol{D}}=10^{-13}$ m^2/s) and curve fits of equation 4.18 estimating permeability change. 66

Figure 4.5: Definition of terms for variable permeability within a skeleton. 69

Figure 4.6: Sample results of TLI numerical simulation and effect of including spatial change in permeability. 70

Figure 5.1: Permeametry using oil flow through cylindrical plug sample. 71

Figure 5.2: Ni powder made by the hydrometallurgical process. 73

Figure 5.3: Photo and schematic of infiltration rate measurement of Multitherm oil into 125–150 μm nickel skeleton. 73

Figure 5.4: Infiltration rate of oil into nickel powder and corresponding rate model. 74

Figure 5.5: Surface tension measurements from dipping nickel plate into Ni – 10.2 wt% Si at 1200°C. 76

Figure 5.6: Setup used to measure infiltration rate inside furnace through mass increase. 78

Figure 5.7: Raw data from dipping experiment to measure local permeability change 81

Figure 5.8: Local permeability change from dipping experiments for skeletons of two different powder size. 82

Figure 5.9: Continuous infiltration rate experiments, comparison with model and permeability curve fits 85

Figure 5.10: Infiltration rate experiments with Ni–Si and model ($\tau = 3.6/T$, $\alpha = 1.4$). 88
Figure 5.11: Infiltration rate experiments with copper and model ($\tau = 3.6/T$, $\alpha = 1.4$). 89
Figure 5.12: Dependence of infiltration limits on powder size based on TLI model. 90
Figure 5.13: Influence of void fraction on vertical infiltration limits generated from model to include the effect of gravity. 91
Figure 6.1: Equilibrium phase diagrams for Fe–C and Fe–Si.[17] 99
Figure 6.2: Prediction of size limitations due to freeze-off in TLI for steel parts. 100
Figure F.1: Apparatus for measurement of viscosity of liquid metal. 110

List of Tables

Table 2.1: Dependence of solidification rate coefficient β on temperature for two infiltrants. ... 23
Table 3.1: Tensile test results and density measurements. 57
Table 5.1: Permeametry using Multitherm 503 oil and skeletons of nickel powder. 72
Table 5.2: Fluid properties of oil and liquid metal infiltrants. 77
Table 5.3: Fitted parameters for Ni–Si infiltrations using $\beta = 1.3$ and $\widetilde{\boldsymbol{D}} = 8.35 \times 10^{-14}$ m^2/s..... 86
Table 5.4: Fitted parameters for copper infiltrations using $\beta = 1.65$ and $\widetilde{\boldsymbol{D}} = 2.2 \times 10^{-13}$ m^2/s.... 86
Table C.1: Properties of Multitherm 503 107
Table E.1: Properties of liquid metals 109
Table F.1: Viscosity measurement of water used to calibrate the diameter of capillary tube. 112
Table F.2: Viscosity measurement of liquid Ni – 11.3 wt% Si at 1200°C. 112

Chapter 1: Introduction

1.1 Background

Over the past decade, the ability to manufacture complex-shaped metal parts has been significantly enhanced through synergy between the fields of Powder Metallurgy (PM) and Solid Freeform Fabrication (SFF). Formerly, the geometric complexity of PM parts was limited by the traditional pressing of the powder into a mold. Likewise, the usefulness of parts made by SFF (also called Rapid Prototyping) was limited by their material composition. The adaptation of SFF processes such as Three-Dimensional Printing to create net-shape metal parts from powder has freed manufacturers from prior geometric constraints and enabled the design of parts with superior functionality. A prime example is the fabrication of tooling with cooling channels that are conformal to the mold surface for enhanced heat transfer.[1] Considerable opportunities exist in the direct fabrication of metal parts by SFF, but current materials do not satisfy the requirements for many potential applications.

PM-based SFF processes typically produce a skeleton of the final part that is only ~60% dense, with void space remaining between the powder particles. The materials challenge lies in the further processing of the part skeleton to achieve full density and the desired mechanical properties. In practice, this is accomplished either by full-density sintering or by liquid infiltration of the void space with another metal. Examples of each method are shown in Figure 1.1 below.

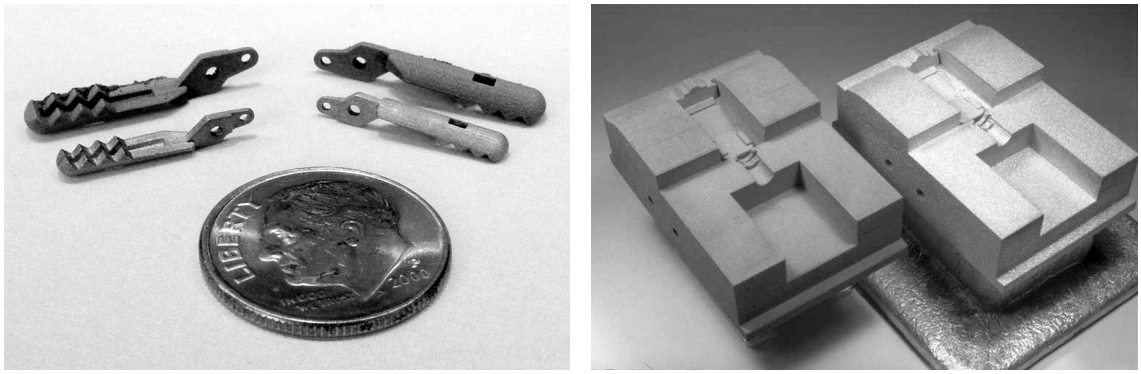

Figure 1.1: Densification of metal powder skeletons made by Three-Dimensional Printing. Left-hand figure shows stainless steel parts sintered to full density in front of the initial skeletons to illustrate shrinkage. Right-hand figure shows a larger (~15 cm) part skeleton before and after infiltration with bronze.

Sintering powder to full density consists of heating to near its melting temperature, causing the powder to consolidate by thermally activated mass transport processes. Since no additional material is added during densification, the final part's material composition matches the initial powder composition and materials choice is very good. However, a skeleton undergoes significant dimensional change of ~15% during full-density sintering. For this reason, it is typically only used for smaller (< 5 cm on a side) parts, for which shrinkage is uniform and distortion is not a problem.

Capillary infiltration of a powder skeleton with liquid metal fills the void space with negligible dimensional change, making this the method of choice for larger parts. The final material composition in this case is a heterogeneous mixture of the powder material and the lower melting temperature infiltrant. The composite material often has poor corrosion resistance and machinability and is not familiar to part designers.

This thesis describes a new method for densification of powder-metal skeletons without significant dimensional change, in contrast to full-density sintering, and that achieves a homogeneous final part composition, in contrast to traditional infiltration. This capability allows Solid Freeform Fabrication of large metal parts in an extended range of materials. In particular, the potential to match the final part composition to existing commercial alloys will prove useful for critical applications (structural, aerospace, military) which require material certification.

1.2 Description of Transient Liquid-Phase Infiltration

Transient Liquid-Phase Infiltration (TLI) uses an infiltrant material that is similar in composition to the powder skeleton and also contains a melting point depressant such that the initial skeleton filled with infiltrant is not at equilibrium. Figure 1.2 provides an example using a generic equilibrium phase diagram. The powder skeleton in this case is pure metal A, with an alloy of metal A and a melting point depressant (MPD) used as an infiltrant. At the infiltration temperature shown, T_i, the liquid infiltrant fills the void space of the skeleton achieving an average bulk composition that is not in equilibrium. The difference in MPD concentration between the infiltrant and skeleton causes solidification of the infiltrant as the MPD diffuses into the skeleton. This isothermal solidification is followed by homogenization and results in a final part composition equal to the average bulk composition after infiltration.

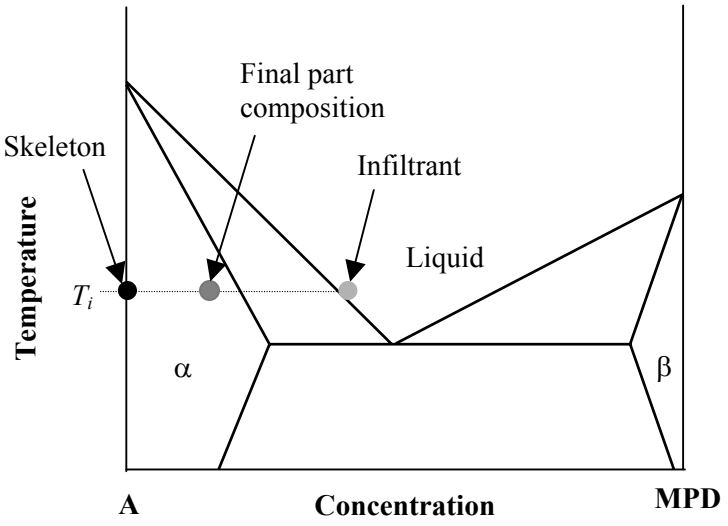

Figure 1.2: Generic equilibrium phase diagram with labeled components of TLI.

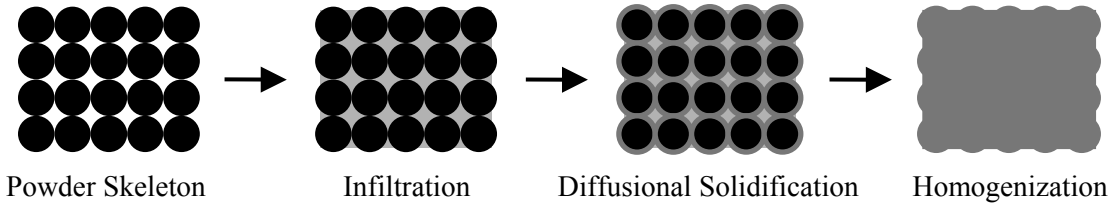

Figure 1.3: Schematic illustration of the stages of Transient Liquid-Phase Infiltration.

A schematic illustration of a powder skeleton is shown in Figure 1.3 followed by the three main stages in transient liquid-phase infiltration. The TLI process owes its name to the liquid-to-solid phase transition of the infiltrant during the diffusional solidification stage. The time scale of each stage can vary considerably under different conditions, but ideally the infiltration occurs quickly so that the liquid fills the part before the infiltrant solidifies. The diffusion should be slow enough to prevent freeze-off, but fast enough to allow homogenization in a reasonable time period. The study of how each of these stages is influenced by the materials, processing conditions and part geometry constitutes a major part of this thesis.

1.3 Important issues for TLI

Outlined below are several important issues or challenges which must be understood for successful development of TLI. Chapters 2 and 3 present the theoretical background and experimental work, respectively, that deal with the materials challenges. The issue of infiltrant freeze-off is presented separately in Chapters 4 and 5, with a model of fluid flow in porous media presented first, followed by comparison with experiments and analysis.

1.3.1 Materials selection

The TLI concept is generally applicable to a high melting temperature powder material and a lower melting temperature infiltrant material that combine to form a homogeneous alloy. For simplicity, the experimental work in this thesis uses two-component systems of a pure metal powder skeleton and a single element as a melting point depressant. The understanding gained from these systems can then be applied to more complex and useful materials systems. For complete homogenization, the final part composition must lie in a single equilibrium phase. In Figure 1.2, the high solubility of MPD in the α phase allows the final part to homogenize into solid solution. If the bulk composition were to lie in the two-phase field between the solid and liquid, then some liquid would remain at equilibrium until the part was cooled. This could actually provide an advantage since the liquid would never completely freeze-off, but the final material resulting from this partial TLI would not be completely homogeneous.

Based on a desired final material composition, skeleton and infiltrant compositions can be chosen based on the volume fraction of the skeleton. Since it is generally desirable to minimize the infiltration temperature and maximize the melting temperature of the skeleton, the MPD is concentrated in the infiltrant. For a skeleton containing no MPD with 40% void fraction, the concentration of MPD in the infiltrant should be ~2.5 times the desired final concentration, varying slightly if the skeleton and infiltrant densities are different. The infiltrant composition determines the minimum temperature at which liquid infiltration can occur.

Diffusivity of the MPD in the skeleton material plays an obvious role in how quickly solidification of the infiltrant occurs as well as how long it takes before the part is homogenized. The width of the two-phase field between the solid and liquid also plays a significant role in determining the solidification rate. These factors are largely established by the choice of materials, but also vary with temperature and the presence of other alloying elements. For a given solidification rate, the powder size and therefore the length scale of diffusion can be selected to adjust the solidification and homogenization time.

A nickel-based materials system was chosen for initial development of the TLI concept because transient liquid-phase nickel brazing alloys are commonly used in the aerospace industry and nickel alloys are of interest in some DoD applications. Silicon was chosen as the melting point depressant because it has a higher solubility and lower diffusivity than boron and phosphorous,

the other common melting point depressant in nickel brazing alloys. Some experiments were also conducted using pure copper as an infiltrant into similar skeletons of pure nickel powder. In this case, copper serves as the MPD and the concentration difference is more extreme. This was done primarily as an additional test case for the model of infiltration rate with simultaneous solidification.

1.3.2 Infiltration distance limits due to freeze-off

A fundamental challenge of transient liquid-phase infiltration is that the liquid infiltrant begins to undergo diffusional solidification as soon as it contacts the skeleton. If this freezing occurs too quickly, it can prevent the liquid from filling the entire skeleton, as illustrated in Figure 1.4. The sequence of images illustrates how the solidification chokes off the flow of liquid during infiltration, with the infiltrant supply completely cut off in the third image. This maximum penetration distance is referred to as the infiltration distance limit for TLI, which for the vertical case shown is corresponds to an infiltration height limit. A TLI infiltration rate model is presented in Chapter 4 based on fluid flow through a powder skeleton with changing permeability. Experimental verification of this model is then presented in Chapter 5.

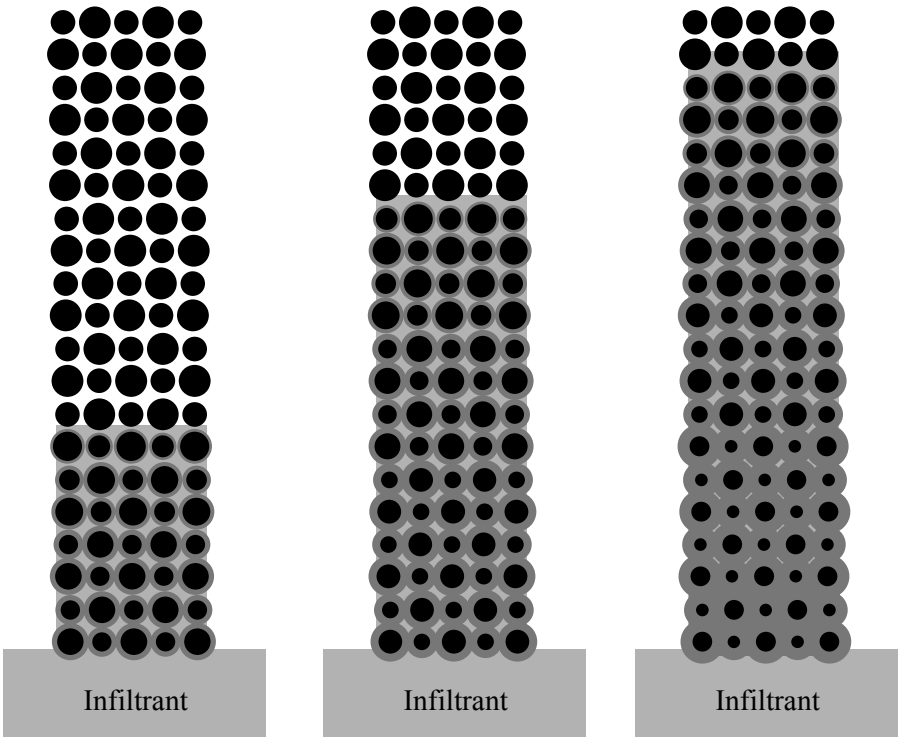

Figure 1.4: Infiltration of a powder skeleton with simultaneous diffusional solidification (progression from left to right) can cause premature freeze-off, limiting the distance the liquid penetrates into the skeleton.

1.3.3 Erosion

In TLI, the same mass transport that causes diffusional solidification when MPD moves into the skeleton can also cause erosion if skeleton material is absorbed into the liquid. Due to the high diffusivity of liquid metals, dissolution tends to occur very quickly if the liquid is not in equilibrium with the solid material. The infiltrant can be supplied at its equilibrium liquidus composition for the infiltration temperature to eliminate the initial propensity to absorb solid. However, subsequent heat generation during the exothermic solidification can offset this initial equilibrium. More detailed discussion of erosion is presented in Chapter 2 with corresponding experimental methods and observations in Chapter 3.

1.3.4 Uniformity of composition throughout the part

Due to simultaneous microscopic mass transport and bulk fluid transport during TLI, the possibility exists that different regions of a part could have variable composition. This would occur if the liquid changed composition while flowing through the part. If liquid infiltrant was supplied at an initial MPD concentration and the concentration was depleted as the liquid flowed through the part, the remote regions farthest from the point of liquid entry would have a lower bulk concentration of MPD. This problem is discussed in more detail in Chapter 2 and is easily addressed for binary alloys. Ensuring uniform bulk composition in ternary and higher alloys is presented briefly, but can be much more complicated and is generally left for further research.

1.3.5 Final microstructure and mechanical properties

In addition to material composition, many other aspects of microstructure play an important role in determining mechanical properties. Just as a forged part and a cast part of identical composition will not behave the same, the properties of a part made by TLI will depend on the grain size, porosity level and homogeneity of the material. Chapter 3 covers the homogenization and resulting microstructure of parts made by TLI including tensile test comparisons to cast parts of identical composition.

1.4 Review of related research

Two prior studies from the early 1980's attempted TLI in iron-based materials systems to create a useful steel part. Thorsen *et al*[2] was reasonably successful in infiltrating a sintered steel skeleton with a Fe-C-P alloy, but an interconnected network of phosphides resulted in a very brittle final

part. Banerjee *et al* [3] chose to rely on carbon as the primary MPD and used cast iron to infiltrate compacts of pure iron powder. This was met with limited success due to the high diffusivity of carbon and subsequently fast freeze-off. In their experimental work using various powders in the size range of ~100 μm, less than 1 cm of liquid penetration was achieved.

This thesis attempts to explain TLI in terms of fundamental physical concepts and well-defined theory. Chapters 2 and 4 provide considerable background in diffusional solidification and flow through porous media in support of this goal. The same physical concepts play a similar role in the closely related fields of research described below. Review of these research areas was beneficial in understanding the physics of transient liquid-phase infiltration.

The flow of liquid into a medium during solidification occurs in many processes, such as forcing liquid into a cold preform in the manufacture of metal-matrix composites and even in the feeding of liquid from risers in traditional casting. In these cases the solidification is due to heat flow rather than mass transport, but the effect on fluid flow is the same. Flemings[4] discusses how interdendritic liquid flow in casting can be compared to flow through porous media. A more closely related example is the reactive infiltration of liquid silicon into a porous carbon preform. Messner and Chiang[5] modeled the flow into a porous skeleton with variable permeability to determine the maximum penetration distance. The permeability in this case was estimated using a simpler model based on effective pore radius that decreased with time, but they presented similar infiltration rate curves where the height is truncated due to the freezing of the liquid. The silicon carbide formation is highly exothermic and is dominated by a solution–reprecipitation mechanism.[6] This required a different freezing model than the diffusional solidification mechanism controlling the motion of the solid/liquid interface for TLI. Further research with SiC–metal systems addresses the compositional variation throughout an infiltrated part that can occur in ternary systems.[7]

Transient liquid-phase brazing is commonly used to repair cracks and bond materials together. This traditional process involves the similar mechanism of a melting point depressant diffusing into a base material and undergoing isothermal solidification. Narrow gaps are necessary for the nickel brazing alloys to fill the capillary channel and solidify in a reasonable amount of time. The solidification time is determined by the diffusion of the melting point depressant into the base metal, and gaps wider than ~50 μm would result in excessively long solidification times. Filling larger gaps with powder similar to the base material allows the liquid brazing alloy to wick into

these larger gaps and solidify faster. These wide-gap brazing[8] techniques have been developed to allow brazing of gaps in excess of 100 μm.

Sintering of powder is often done above the melting point of some of the constituents, such that presence of liquid aids in the consolidation of the powder compact.[9,10] This liquid-phase sintering can either involve pre-alloyed powder with a wide freezing range or a mixture of different powders, with the sintering temperature above the melting temperature of one of the constituent powders. In both cases, liquid of one composition surrounds the remaining solid particles. For some materials, the liquid phase is transient and the diffusion of a MPD into the solid causes isothermal solidification.[11] These cases involve similar mechanisms for the homogenization of the final material.

Chapter 2: Diffusional Solidification Theory

2.1 Solidification theory by mass transport

2.1.1 Fick's laws and diffusivity

Mass transport resulting from a one-dimensional concentration gradient within a material can be described by Fick's first law of diffusion:

$$J_A = -D_A \frac{\partial C_A}{\partial x} \tag{2.1}$$

where J_A is the net flux of atoms per unit area, C_A is the concentration of metal A in atoms or moles per unit volume, and D_A is the intrinsic diffusion coefficient of the metal A in the given material. In a binary alloy of two metals A and B with a gradient in concentration, this mass transport results in a change in concentration over time at each position given by Fick's second law of diffusion:

$$\frac{\partial C_A}{\partial t} = \frac{\partial}{\partial x} \widetilde{D} \frac{\partial C_A}{\partial x} \tag{2.2}$$

where $\widetilde{D}$ is the chemical diffusion coefficient representing the interdiffusion of the two metals.[12] It varies with material composition, but is often assumed constant for small concentration differences. The chemical diffusion coefficient follows an Arrhenius temperature dependence and is typically reported in literature for a given composition range in terms of a frequency factor D_o and an activation energy Q.

$$\widetilde{D} = D_o \cdot e^{-\frac{Q}{RT}} \tag{2.3}$$

where R is the universal gas constant, 8.314 J-mol^{-1}-K^{-1}, and T is the temperature in degrees Kelvin. For diffusion of silicon in pure nickel, D_o = 1.5 cm^2/s and Q = 258.3 kJ/mol,[13] resulting in $\widetilde{D}$ = 8.35e^{-14} m^2/s at 1185°C. This diffusivity can be reasonably applied to the fairly narrow concentration range of interest for Ni–Si infiltrations. For wider ranges in concentration, this assumption may not be valid. The interdiffusion of nickel and copper provides an example of a system in which the concentration dependence of $\widetilde{D}$ is more significant and is discussed in more detail in section 2.2.2.

2.1.2 Diffusional solidification and solution of the moving-interface problem

The isothermal solidification of infiltrant can be characterized by the motion of the solid-liquid interface resulting from diffusion. The interface motion is determined using the Stefan condition, applying conservation of mass at the interface in conjunction with Fick's first law[14]:

$$\left(C_l - C_s\right)\cdot\frac{dX}{dt} = \widetilde{D}_{solid}\cdot\left.\frac{dC}{dx}\right|_{x=X_s} - \widetilde{D}_{liquid}\cdot\left.\frac{dC}{dx}\right|_{x=X_l} \tag{2.4}$$

where C_l and C_s are the equilibrium liquidus and solidus concentrations, X is the position of the interface, and the right hand terms are the mass flux due to the concentration gradient on the solid and liquid sides of the interface, respectively. Generation of heat could influence the liquidus and solidus concentrations as well as the diffusivities, but is ignored for the isothermal case presented here. The self-diffusivity in both liquid Ni and liquid Cu at their respective melting points is ~$4e^{-9}$ m^2/s, [15] and the diffusivity of smaller solute atoms is likely to be even higher. Since the liquid diffusivity is four orders of magnitude higher than the solid, the interface motion can typically be separated into two distinct regimes. For a brief initial dissolution period, the right hand side of equation 2.4 is dominated by the second term containing $\widetilde{D}_{liquid}$ and the interface moves into the solid until all of the liquid reaches its equilibrium liquidus composition. Once the gradient in the liquid reaches zero, the interface begins to move back into the liquid and the same term can be neglected during the subsequent diffusional solidification since there is no mass flux to the interface from the liquid. To prevent erosion, as discussed further in Chapter 3, the infiltrant is typically supplied at its equilibrium liquidus concentration so the initial dissolution period is avoided. The corresponding initial conditions are illustrated by the solid line in Figure 2.1. Specifically, the initial conditions are $C=C_o$ in the solid, $C=C_l$ in the liquid and initial interface position $X=0$ and the concentration is that of the melting point depressant.

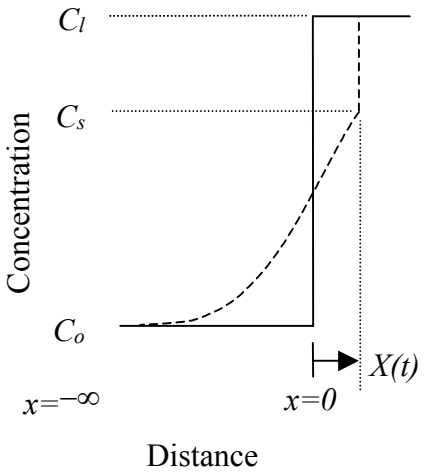

Figure 2.1: Schematic of the moving interface problem showing the concentration profile for a given time after interface has moved to *X(t)*.

The dashed line represents the concentration profile after some diffusional solidification has occurred and the interface has moved to position *X(t)*. Conservation of mass requires that the solute taken from the liquid (the area above the dashed line and to the right of the initial interface) is absorbed into the initial solid (the area below the dashed line and to the left of the initial interface), so the two areas must be equal. The concentration profile is found by application of Fick's second law in the solid and can be satisfied by a solution of the form:

$$C(x,t) = A + B \cdot \mathrm{erf}\left(\frac{x}{\sqrt{4\tilde{D}t}}\right) \tag{2.5}$$

where A and B are constants to be determined by the following boundary conditions

$$C(-\infty,t) = C_0 = A - B$$

$$C(X(t),t) = C_s = A + B \cdot \mathrm{erf}\left(\frac{X(t)}{\sqrt{4\tilde{D}t}}\right)$$

To satisfy the second boundary condition, the argument of the error function must be a constant, therefore *X(t)* must be directly proportional to the denominator.

$$X(t) = \beta \cdot \sqrt{4\tilde{D}t} \tag{2.6}$$

where the constant β will be determined by mass conservation at the moving interface. The solution for the concentration profile for the given conditions is obtained using the following constants:

$$B = \frac{C_s - C_0}{(1 + \mathrm{erf}(\beta))}$$

$$A = C_0 + \frac{C_s - C_0}{(1 + \mathrm{erf}(\beta))}$$

$$C(x,t) = C_0 + \frac{C_s - C_0}{(1 + \mathrm{erf}(\beta))} + \frac{C_s - C_0}{(1 + \mathrm{erf}(\beta))} \cdot \mathrm{erf}\left(\frac{x}{\sqrt{4\tilde{D}t}}\right) \tag{2.7}$$

The derivatives of concentration and interface position are therefore:

$$\frac{dC(x,t)}{dt} = \frac{C_s - C_0}{(1 + \mathrm{erf}(\beta))} \cdot \frac{2}{\sqrt{\pi}\sqrt{4\tilde{D}t}} \cdot \exp\left(-\left(\frac{x}{\sqrt{4\tilde{D}t}}\right)^2\right)$$

$$\frac{dX(t)}{dt} = \beta\sqrt{\frac{\tilde{D}}{t}}$$

and can be substituted into equation 2.4 to solve for β. Once again, since the liquid is all at its equilibrium concentration, the flux is determined solely by the concentration gradient in the solid at the interface.

$$(C_l - C_s) \cdot \beta\sqrt{\frac{\tilde{D}}{t}} = \tilde{D} \cdot \frac{C_s - C_0}{(1 + \mathrm{erf}(\beta))} \cdot \frac{2}{\sqrt{\pi}\sqrt{4\tilde{D}t}} \cdot \exp(-\beta^2) \tag{2.8}$$

Rearrangement and cancellation of terms allows β to be determined directly from the given concentration ratio.[14,16]

$$\sqrt{\pi} \cdot \beta \cdot (1 + \mathrm{erf}(\beta)) \cdot \exp(\beta^2) = \frac{C_s - C_o}{C_l - C_s} \tag{2.9}$$

The dependence of β on the concentration ratio is shown graphically in Figure 2.2.

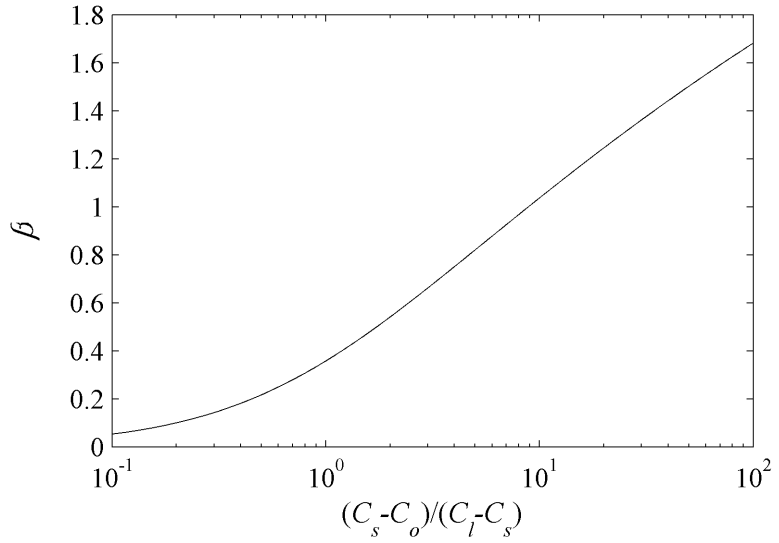

Figure 2.2: Graphical representation of equation 2.9 illustrating the dependence of the solidification rate coefficient β on the given concentration ratio.

2.1.3 Material system characteristics controlling solidification rate

Equilibrium phase diagrams for both Ni–Si and Cu–Ni are presented in Figure 2.3 for reference in discussing how β varies with MPD solubility and the width of the two-phase field. For a pure nickel skeleton, the numerator is equal to the maximum solubility and represents the scale of the concentration gradient. A steeper gradient provides greater driving force for diffusion and therefore a faster solidification rate. The denominator of the concentration ratio is equal to the width of the two-phase field between solid and liquid. For a given solidification distance, a larger difference between the liquidus and solidus corresponds to a greater amount of MPD that must be absorbed into the skeleton. Similarly, for a fixed diffusion rate, a wider two-phase field will slow down the solidification.

Ni-Si

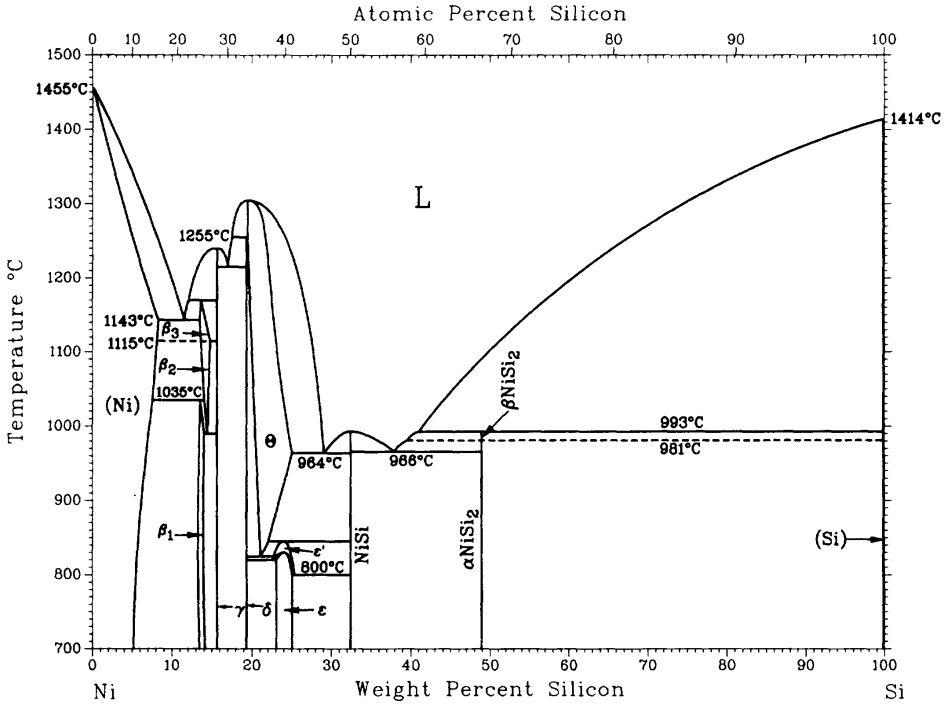

Cu-Ni

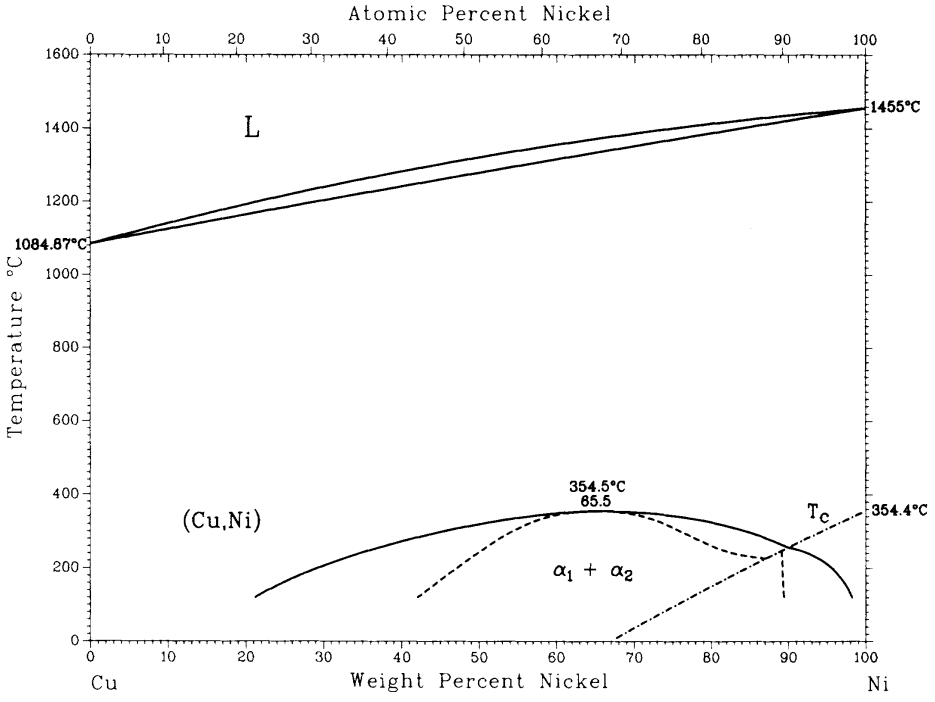

Figure 2.3: Equilibrium phase diagrams[17] for Ni–Si and Ni–Cu .

The Ni–Si phase diagram demonstrates the case when the partition coefficient, defined as $k \equiv C_s / C_l$, is relatively constant with temperature. For an initial skeleton concentration of C_o=0% Si, the concentration ratio of equation 2.9 can be expressed solely as a function of k because the solidus and liquidus are approximately linear.

$$\frac{C_s - C_o}{C_l - C_s} = \frac{1}{\frac{1}{k} - 1} \tag{2.10}$$

The Cu–Ni phase diagram demonstrates the case when the concentration ratio can vary significantly with temperature because the denominator approaches zero at the melting point of copper. Table 2.1 shows how the resulting value of β decreases as the infiltration temperature increases. Since the solidification rate is proportional to $\beta\sqrt{\widetilde{D}}$ and diffusivity generally increases with temperature, selecting an optimum infiltration temperature in this system can minimize the solidification rate and prevent infiltrant freeze-off. A further complication in the copper-nickel system is that the diffusivity is strongly dependent on composition as well as temperature. The interdiffusion coefficients listed reflect the changing solidus concentration and represent the effective diffusivity that controls the solidification rate. These values were determined using a numerical simulation discussed in greater detail in section 2.2.2.

Infiltrant	Temp (°C)	C_s (at %)	C_l - C_s (at %)	β	$\widetilde{D}$ (10^{-13} m^2/s)	$\beta\sqrt{4\widetilde{D}\cdot(100\,\mathrm{sec})}$ (μm)
Ni–Si	1160	15.0 (Si)	5.7	0.62	0.58	3.0
	1200	13.0	5.8	0.58	1.04	3.7
	1250	10.3	5.6	0.52	2.07	4.7
	1300	8.0	5.0	0.48	3.97	6.0
Cu–Ni	1085	99.9 (Cu)	0.05	2.33	3	26
	1100	95.9	1.08	1.65	2.2	15
	1150	82.7	4.87	1.20	1.6	9.6
	1200	68.9	9.04	0.95	1.5	7.4
	1250	55.9	10.1	0.85	1.7	7.0
	1300	42.2	11.4	0.73	2.1	6.7

Table 2.1: Dependence of solidification rate coefficient β on temperature for two infiltrants.

2.2 Numerical simulation

2.2.1 General description and effect of finite boundary conditions

The two-phase moving-interface problem can be solved analytically for semi-infinite boundary conditions in one dimension, but numerical methods are necessary to study several special cases of interest: finite boundary conditions, diffusivity change with composition, and spherical

geometry. The method described by Tanzilli and Heckel[18] was carried out using MATLAB, with the code included in Appendix A. At each time step, the interface motion is determined using a finite-difference version of equation 2.4, and then Fick's second law is applied to the bulk of each phase using a variable-grid space transformation to account for the interface motion and corresponding stretching of the grid.

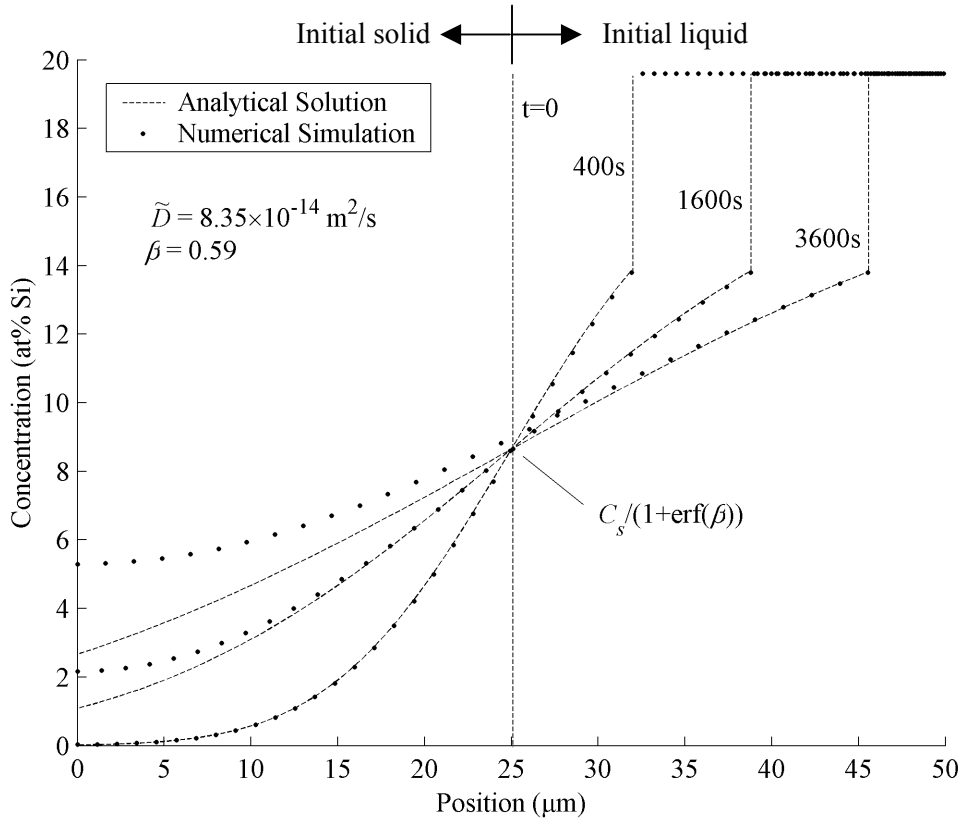

Figure 2.4: One-dimensional diffusional solidification of Ni–Si at 1185°C with finite (simulation) and semi-infinite (analytical) boundary conditions.

The concentration profile of the numerical simulation matches the analytical solution at 400 seconds, when the width of the simulation is effectively semi-infinite because the concentration reaches zero prior to the edge. For longer times, the concentration at the edge is higher in the simulation because the zero mass-transfer boundary allows buildup of solute. Despite this interior buildup of solute, the interface motion for the finite case is identical to the interface motion for the semi-infinite analytical solution for the time range shown. The solidification rate is expected to decrease for the finite boundary conditions, but this does not occur until the solid becomes nearly saturated. Figure 2.5 shows the solidification behavior of the same solid thickness

for longer times. The solid width was kept constant at 25 μm, thus interface motion greater than 25 μm corresponds to an average composition in the solid greater than $C_l/2$, nearly 75% of the solidus concentration. The effect of the finite boundary conditions depends on the relative liquidus and solidus concentrations for a given material system. For skeleton material that is not near saturation, the finite boundary condition has little effect on the initial motion of the interface, which is the time of concern for determining liquid flow in TLI.

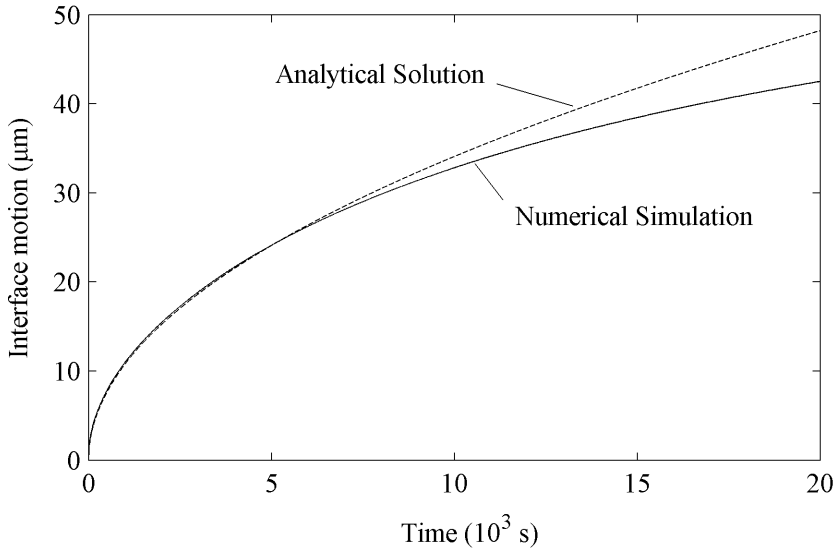

Figure 2.5: Decrease in solidification rate due to finite boundary conditions at long time.

2.2.2 Diffusivity variation with composition

Transient liquid-phase infiltration of nickel powder with copper infiltrant is the most extreme case of variation in concentration between the skeleton and infiltrant. For diffusion of nickel in pure copper, D_o = 1.4 cm^2/s and Q = 228.2 kJ/mol, resulting in $\widetilde{D}_{Ni}$ = 2.9e^{-13} m^2/s at 1100°C. For diffusion of copper in pure nickel, D_o = 0.4 cm^2/s and Q = 257.9 kJ/mol, resulting in $\widetilde{D}_{Cu}$ = 6.2e^{-15} m^2/s at the same temperature, nearly 50 times lower. The Tanzilli–Heckel numerical simulation presented in the previous section assumed a constant diffusivity in each phase, but the model was adapted to accommodate variable diffusivity for the nickel-copper system. In the interface mass-balance equation (equation 12 of T–H), the diffusivity at the solidus concentration was used to determine the interface velocity. The diffusion coefficient used in the solution to Fick's second law in the solid (equation 10 of T–H) was determined locally as a function of concentration and used to evaluate the second derivative. Specifically, $\widetilde{D}\cdot\left(C_{n-1}-2C_n+C_{n+1}\right)$ was replaced by $\widetilde{D}_n\left(C_{n-1}-C_n\right)-\widetilde{D}_{n+1}\left(C_n-C_{n+1}\right)$, where $\widetilde{D}_n$ is the diffusion coefficient at the concentration C_n.

The chemical diffusion coefficient for each concentration was determined by extrapolation of data presented in Smithells,[13] Table 13.18 for interdiffusion of Ni–Cu at 1066°C. A semilog quadratic curve fit to the data for the given temperature was adjusted for a desired temperature based on the frequency factor and activation energy for interdiffusion in pure nickel.

$$\widetilde{D}(C,T)=\left(4\times10^{-5}\cdot\exp^{-\frac{257{,}900}{RT}}\right)\cdot10^{0.2912\cdot C+1.6596\cdot C^2} \tag{2.11}$$

where T is in degrees Kelvin, C is the atomic fraction copper, and the diffusivity is in m^2/s. The implicit assumption that the concentration dependence of $\widetilde{D}$ is independent of temperature is of questionable validity, but the approximation is useful for investigating whether the solidification rate is more dependent upon the diffusivity in the bulk solid or the diffusivity in the Cu–enriched solid near the interface.

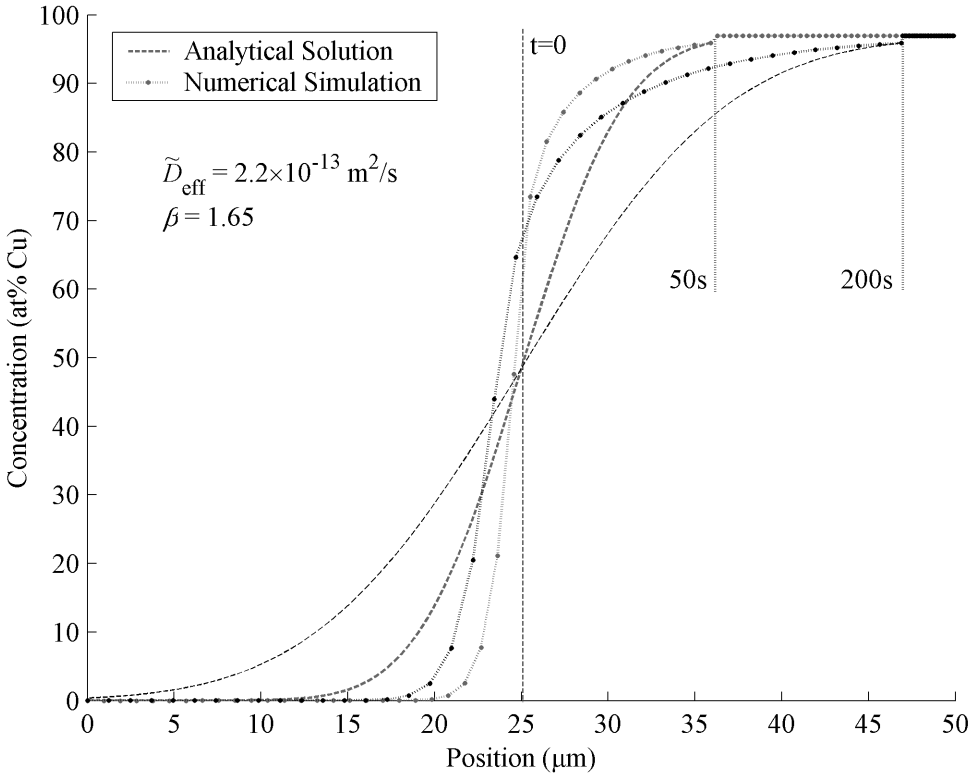

Figure 2.6: Numerical simulation of diffusional solidification in Ni–Cu at 1100°C using a concentration dependent diffusivity.

The concentration profile using concentration dependent diffusivity is asymmetric to reflect the higher diffusivity in the solute-rich region of the solid. The Ni–Cu case also further illustrates the

discussion of section 2.1.3, where the narrow two-phase field at 1100°C allows faster interface motion because very little solute absorption is required as the interface advances. The effect of variable diffusivity during solidification at a higher infiltration temperature where the two-phase field is wider is presented in Figure 2.7. A similar result is obtained with slightly less asymmetry in the concentration profile as compared with Figure 2.6.

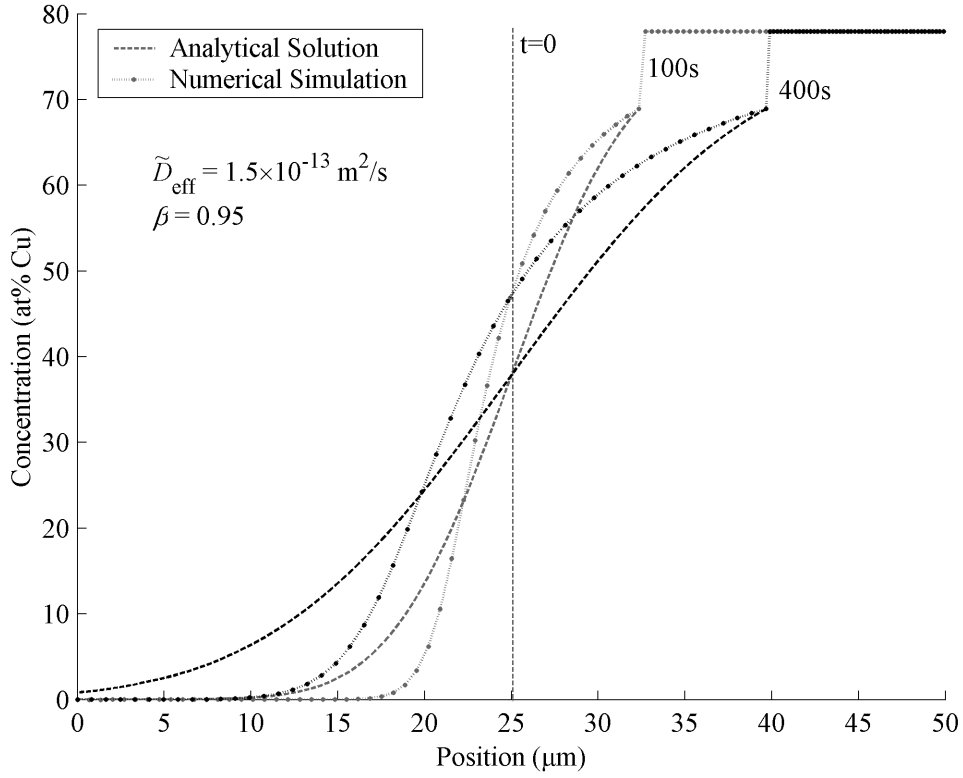

Figure 2.7: Numerical simulation of diffusional solidification in Ni–Cu at 1200°C using a concentration dependent diffusivity.

The interface motion in both Figure 2.6 and Figure 2.7 is linear when plotted against the square root of time. This suggests that the interface motion can be sufficiently described using an effective diffusivity applied uniformly throughout the solid.

$$\widetilde{D}_{eff} = \left(\frac{X}{2\beta\sqrt{t}} \right)^2 \tag{2.12}$$

where X is the interface motion at time t, and $\widetilde{D}_{eff}$ is determined by a least squares fit to the interface motion of the simulation. The interface motion depends on the diffusivity at the solidus concentration, but the corresponding concentration gradient at the interface is lower for the case of variable diffusivity. The solute is unable to penetrate very far into the pure nickel because of the lower diffusivity, and it builds up near the interface as a result. The difference between the diffusivity at the solidus composition and the effective diffusivity relates to the difference in interface slope between the simulation using variable diffusivity and the analytical solution based on the assumption of uniform diffusivity. The mass flux that controls the interface motion is the same in both cases by definition of the effective diffusivity.

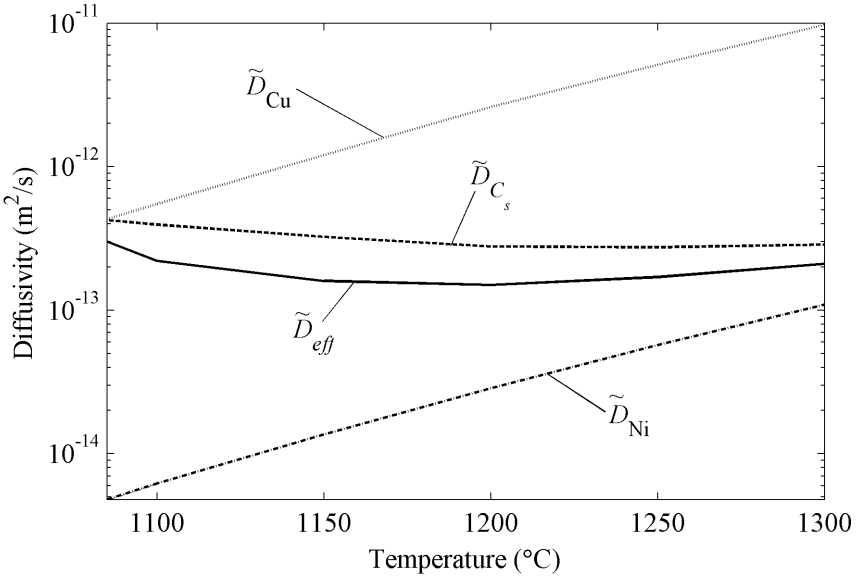

Figure 2.8: Effective diffusivity controlling interface motion for Ni–Cu infiltrations.

The decrease in diffusivity at the solidus concentration for increased temperature is the result of the strong dependence on concentration expressed in equation 2.11 along with changing solidus concentration as shown in Table 2.1. The effective diffusivity falls between the diffusivity in the bulk solid (pure nickel) and the diffusivity at the solidus concentration, generally weighted heavily towards the solidus concentration. The specific weighting depends both on the equilibrium solidus and liquidus concentrations and the dependence of diffusivity on concentration, so the weighting is difficult to characterize universally. When confronted with a material system with significant variation in diffusivity, the solidification rate depends more strongly on the diffusivity near the interface, rather than in the bulk material. The solid material

at the interface quickly reaches the solidus concentration to maintain equilibrium and the localized diffusivity determining interfacial mass flux is therefore based on the solidus concentration. The local concentration gradient also determines the mass flux and will be affected by the diffusivity farther from the interface, but this appears to be a secondary effect.

2.2.3 Extension to cylindrical and spherical coordinates

The numerical simulation of Tanzilli and Heckel allows study of the effect the geometry of the solid interface has on the solidification behavior. The appropriate modifications to the interface mass balance and Fick's second law for cylindrical and spherical interfaces are provided in their paper. The initial width of the solid phase (positions 0–25μm on the left side) in these cases corresponds to the radius of the cylinder or sphere. The width of the initial liquid phase on the right corresponds to the shell thickness of the liquid.

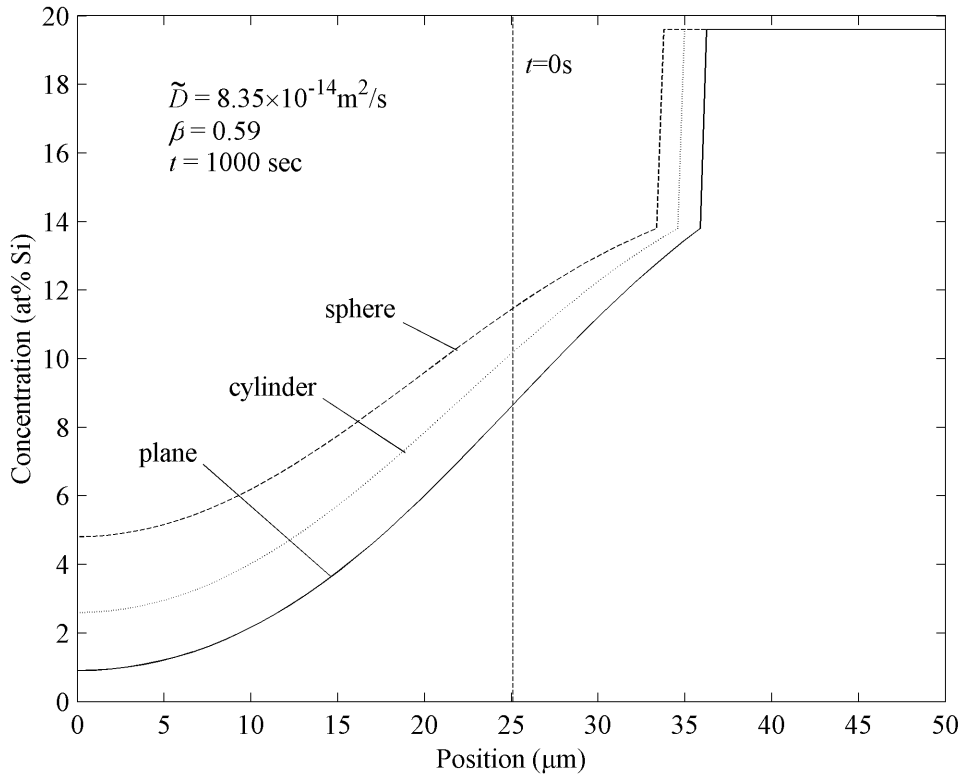

Figure 2.9: Comparison of diffusional solidification for planar geometry, 50 μm diameter cylinder, and 50 μm diameter sphere.

The solidification rate decreases for the curved geometries because the solid has a diminished capacity to absorb solute in proportion to the interface motion. For the planar case, 5 μm of interface motion results in a 20% growth of a 25 μm slab. The same interface motion considered for curved geometry results in a 20% increase in radius. This corresponds to a 44% increase in volume for a cylinder or a 73% increase for a sphere. When using a single sphere to model the geometry of a packed powder bed, one method is to relate the thickness of a spherical shell to the void fraction of the powder bed by

$$v_f = \frac{R^3}{(R+X)^3} = 1-\varepsilon \qquad \text{or} \qquad X = R\left(\frac{1}{\sqrt[3]{1-\varepsilon}} - 1\right) \tag{2.13}$$

where R is the initial radius, X is the shell thickness or solidification distance, and ε is the void fraction. For a bed of 50 μm diameter powder with 40% void fraction, equation 2.13 would require a shell thickness of only 4.5 μm. This relation should be used only as a rough approximation since this single-sphere model can not be stacked to fill space, and is therefore not truly analogous to the geometry of a powder bed.

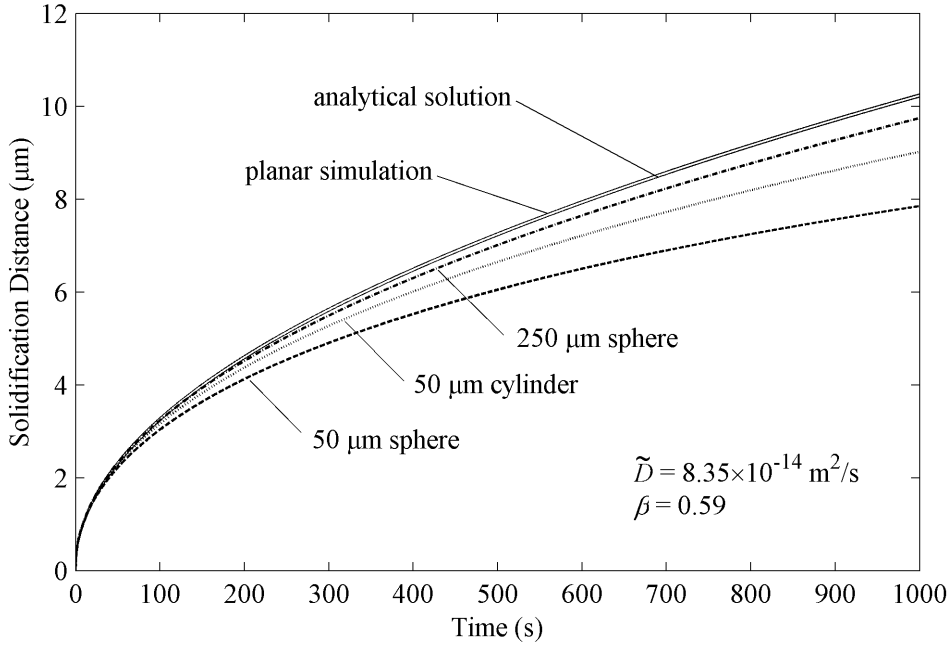

Figure 2.10: Interface motion for diffusional solidification with curved interface geometry.

The solidification distance for planar geometry matches the analytical solution. The deviation from the planar solution seen for the curved geometry can be represented by a second term added to equation 2.6.

$$X(t) = \beta\sqrt{4\tilde{D}t} + \Delta X \tag{2.14}$$

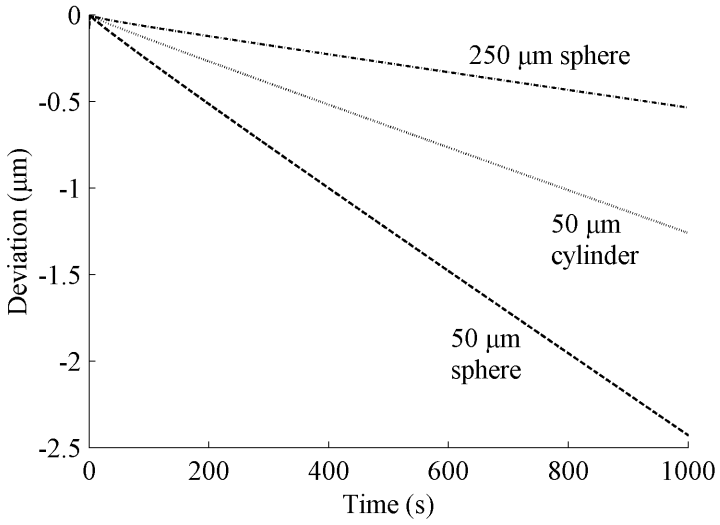

Figure 2.11: Deviation distance from planar interface motion for diffusional solidification with curved interface geometry.

From the numerical simulation results of Figure 2.11, the deviation is seen to increase linearly with time for all three cases. The deviation for the spherical case is twice that of the cylindrical case of the same geometry, and the deviation for the 250 μm sphere is one fifth that of the 50 μm sphere. Further, a doubling of the diffusion coefficient resulted in twice the deviation with all other factors equal. Based on these observed relationships, the deviation can be said to vary linearly with curvature, diffusivity and time.

$$\Delta X \propto \left(\frac{1}{r_1} + \frac{1}{r_2}\right) \cdot \tilde{D} \cdot t \tag{2.15}$$

where r_1 and r_2 are the two principal radii of curvature. For a cylinder, r_1 would equal the cylinder radius and r_2 would be infinite. For a sphere, both r_1 and r_2 would be equal to the sphere radius. Based on the results of Figure 2.11, a constant of proportionality 0.374 would precede the right hand side of equation 2.15 to equal the observed deviation. Since other factors might also influence the deviation, this observation should not be treated as universal.

2.3 Free energy release during solidification and homogenization

In thermodynamic terms, a material at equilibrium is by definition in its lowest energy state. This is illustrated in Figure 2.12, where the minimum free energy determines the equilibrium phase at a given concentration. Between the solidus and liquidus concentrations, the minimum Gibbs free

energy is achieved with a mixture of solid at the solidus concentration and liquid at the liquidus concentration, where a tie line connecting the common tangents defines the energy of the mixture.[19,20]

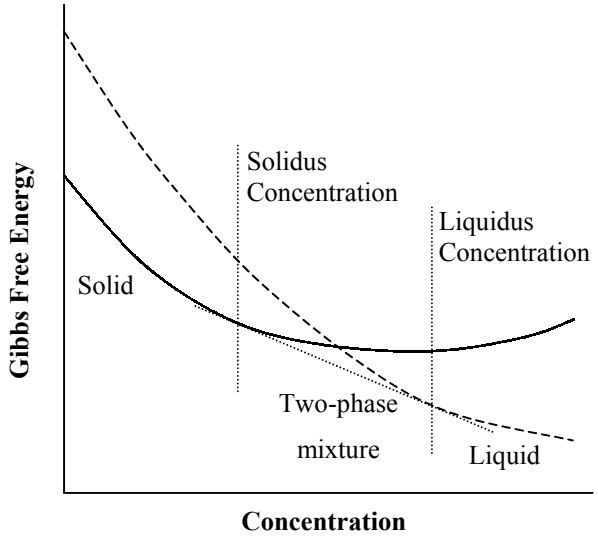

Figure 2.12: Determination of equilibrium phase based on minimum thermodynamic potential or Gibbs free energy.

In transient liquid-phase infiltration, the initial condition of the material consists of a solid skeleton and liquid infiltrant. During the solidification and homogenization processes, the material moves toward a state of lower free energy. The amount of heat released during the transformation is given by the change in enthalpy of the system, ΔH. A plot of enthalpy for mixtures of nickel and silicon at 1185°C is shown in Figure 2.13. The liquidus concentration at this temperature is approximately 20 at% Si, and if used to fill a pure nickel skeleton with 40% void fraction, the average bulk concentration would be ε times C_l or 8 at% Si. The enthalpy of the pure nickel is zero, so the initial enthalpy of an infiltrated part is equal to that of the liquid alone. The final enthalpy after homogenization is given by the solid at C_{final}. The net change in enthalpy can be represented by the vertical distance between the line representing the initial mixture and the solid at C_{final}. For this example, the enthalpy change is equal to:

$$\Delta H = \left(-14.5\,{}^{\text{kJ}}/_{\text{mol}}\right) - \left(-13.2\,{}^{\text{kJ}}/_{\text{mol}} \cdot 0.4\right) = -9.2\,{}^{\text{kJ}}/_{\text{mol}} \tag{2.16}$$

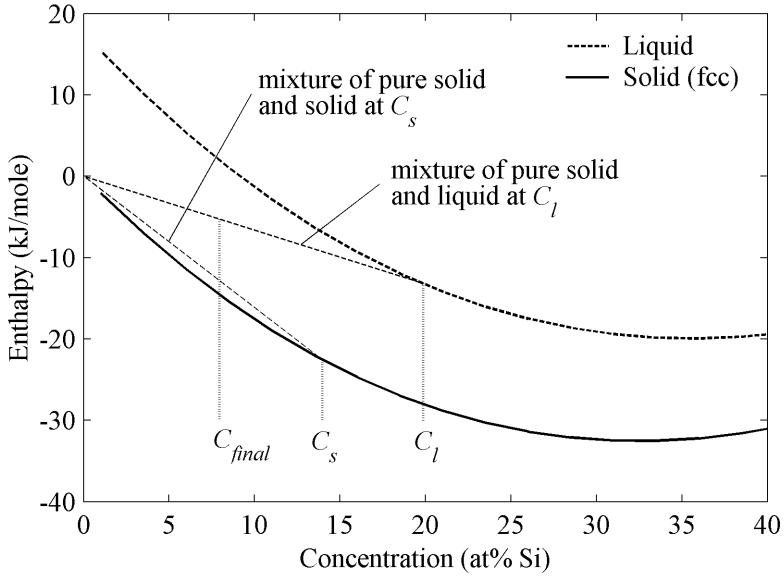

Figure 2.13: Enthalpy for a binary mixture of Ni–Si at 1185°C[21] used to determine heat released during solidification and homogenization.

For an adiabatic system, this release of enthalpy would heat up the material based on its molar heat capacity. As an approximation, the value for pure nickel is used:

$$\Delta T = \frac{-\Delta H}{C_p} = \frac{9200\ {}^{\mathrm{J}}/_{\mathrm{mol}}}{26\ {}^{\mathrm{J}}/_{\mathrm{mol\cdot K}}} = 354°\mathrm{C} \tag{2.17}$$

This would be a sufficient temperature increase to heat the entire part above the melting temperature of pure nickel. The release of enthalpy actually occurs over a period of time as the solidification progresses, so the system will not be adiabatic, but heat will be released to the surroundings at a rate that depends on the part geometry and heat transfer properties. The specific generation and dissipation of heat during the solidification happens over a continuum that is difficult to characterize, but some basic assumptions can provide a better idea of the effect of the latent heat release.

Heat loss at these high temperatures can be assumed to be dominated by radiation and can be estimated using a Taylor series expansion.

$$q = \left(4\varepsilon^{*}\sigma T^{3}\right)\cdot \Delta T = h_{rad}\Delta T \tag{2.18}$$

where q is the heat loss per unit area, ε^{*} is the emissivity (~0.2 for Ni), σ is the Stefan-Boltzmann constant, 5.6697e^{-8} W/m^{2}K^4, T is the surface temperature in Kelvin and ΔT is the increase in temperature of the part above its surroundings. The term in parenthesis can be treated as a

radiative heat transfer coefficient, h_{rad}, equal to 146 W/m^{2}K for the given emissivity at 1200°C. Taking the heat loss into consideration over a given time period t, the increase in temperature of equation 2.17 can now be described by:

$$-\Delta H - \frac{M}{\rho V}\left(h_{rad} A \Delta T\right) \cdot t = C_p \cdot \Delta T \tag{2.19}$$

where ρ and M are the material density and molecular weight, and V and A are the volume and surface area of the part. The appropriate time over which the heat is released, t, can be chosen to reflect various condition and is discussed later. The temperature difference on the left-hand side of the equation expresses the temperature of the part relative to its surrounding and the temperature difference on the right-hand side corresponds to the increase in part temperature due to heating, but they can be set equal because the part starts out at the temperature of the surroundings. The expected temperature increase can then be determined based on the part geometry and a given time.

$$\Delta T = \frac{-\Delta H}{\left(C_p + \frac{M \cdot h_{rad} A}{\rho V} t\right)} \tag{2.20}$$

For nickel, with M=58.7 g/mole and ρ=8.9 g/cc, and a cylindrical part geometry of 1 cm diameter, the coefficient of time in the denominator is ~0.4 W-mol^{-1}K^{-1}. If the total homogenization time were considered, which might be on the order of 1 hour, then the temperature rise would be only a modest 6°C. Macroscopically, the generation of heat occurs uniformly throughout the material during diffusional solidification, but the heat dissipation is dependent upon external geometry. Smaller cross-sections would release more heat per unit volume resulting in less temperature increase, and the opposite would be true for larger part cross-sections.

Most of the enthalpy is actually released during the phase change, which occurs much faster than the total homogenization time. With less time to dissipate heat, a greater temperature increase will cause a shift in the equilibrium liquidus concentration and cause dissolution of the skeleton. Erosion is most noticeable when the dissolution of the skeleton occurs while liquid is still flowing into the part because the dissolved material is transported away in the liquid. During this short period of time, only some of the solidification has occurred, and very little homogenization is likely to take place. The change in enthalpy during the infiltration is therefore only a fraction of that calculated in equation 2.16.

For a transient liquid-phase infiltration when the part dimensions are close to the limits of infiltrant freeze-off, the solidification time is of the same order as the infiltration time. The enthalpy change of the system immediately after solidification, but prior to homogenization, can be approximated using the line shown in Figure 2.13 between the pure solid and the equilibrium solidus concentration. This assumes that all of the solid is either pure nickel or saturated with solute, which is obviously not the case, but provides a rough estimate of the enthalpy released during solidification, as opposed to the subsequent mixing. From Figure 2.13, this line shows that the enthalpy change occurring during the change of phase is equal to 7.6 kJ/mol, more than 80% of the total enthalpy change. This lower enthalpy value and the solidification time for a given powder skeleton could be used in equation 2.20 to estimate the increase in temperature during infiltration for a given part. Since solidification times are typically on the order of one minute, the resulting predicted temperature increase could be substantial, perhaps exceeding 100°C.

As mentioned earlier, large rises in temperature can cause considerable erosion of the skeleton because the equilibrium liquidus concentration has more nickel at higher temperatures. The skeleton quickly absorbs nickel from the skeleton until it reaches equilibrium. Conservation of mass can be applied to determine how much of the skeleton is absorbed for a given change in liquidus concentration.

$$C_l(T)\cdot\varepsilon = C_l(T+\Delta T)\cdot(\varepsilon + f(1-\varepsilon)) \tag{2.21}$$

where f is the fraction of the skeleton that is dissolved and can be solved directly using:

$$f = \frac{\varepsilon}{1-\varepsilon}\cdot\frac{C_l(T)-C_l(T+\Delta T)}{C_l(T+\Delta T)} \tag{2.22}$$

An increase in temperature from 1185°C to 1285°C would change the liquidus concentration from ~20 at% Si to ~14 at% Si. For a skeleton with 40% void fraction, nearly 30% of the skeleton would be dissolved. Erosion is discussed further in section 3.4 along with discussion of experimental observations.

2.4 Uniform composition throughout the final part

As mentioned in the introduction, mass transport occurring simultaneously with fluid transport during transient liquid-phase infiltration can potentially lead to compositional gradients within the final part. This would occur if liquid changed composition while flowing into the part. In a binary system, this variation can be prevented by supplying the infiltrant at its equilibrium liquidus composition. This will ensure that any liquid present in the skeleton will be the same

composition — any loss of silicon must result in solidification. Indeed, this method is already applied in order to prevent erosion of the skeleton. Erosion and compositional variation are linked because composition variation would be the result of skeleton material being dissolved in one area and carried to another region of the part. Figure 2.14 helps to provide a more technical explanation of how uniform composition can be guaranteed using infiltrant at its liquidus composition.

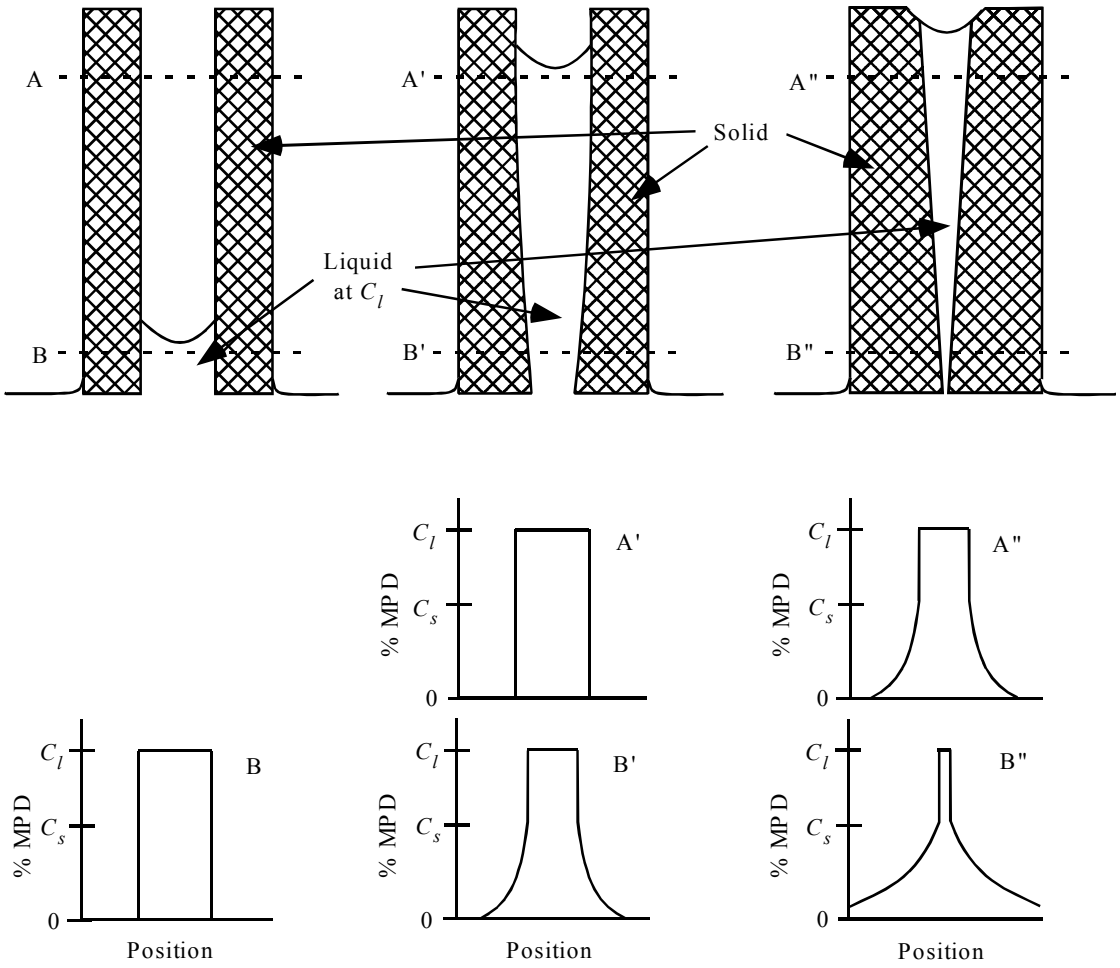

Figure 2.14: TLI into a capillary with infiltrant at its liquidus composition, C_l. Top sequence shows progression of solidification as liquid rises to the top of the capillary. Bottom sequence plots the concentration profile of the MPD at cross-sections A and B.

The top sequence shows infiltration into a one-dimensional capillary (two thin plates) with solidification of the infiltrant occurring as the liquid fills the channel. The scale is distorted to better illustrate the degree of solidification changing along the height. The bottom sequence shows the expected concentration profile corresponding to the cross-sections at the heights

marked A and B with primes denoting different times. Because the infiltrant is supplied at its liquidus composition, it remains constant at C_l throughout the infiltration. The composition profile at a point just behind the infiltration front (cross-section B) consists of pure nickel and infiltrant at its liquidus composition because very little time has elapsed to allow for diffusion. After a time interval of Δt, when the liquid has filled most of the capillary, a similar location just behind the infiltration front at cross-section A' has an composition profile identical to B. Some diffusional solidification will have occurred at B' since the liquid and solid have been in contact for the interval Δt. After another time interval Δt, the cross-section at A" will now have solidified to the same degree as cross-section B', and cross-section B" will have solidified even further. The point of this analysis is to show how the fixed composition of the liquid ensures the bulk or average composition will be the same at heights A and B — constant with both time and position.

Ensuring uniform composition during TLI with ternary and higher systems becomes more complicated because the solidification process can change the composition of the remaining liquid. As an extreme example of this concept, Hozer and Chiang[7] describe the rejection of metal during the reactive infiltration of carbon preforms with various metal alloys containing silicon. The rapid formation of SiC extracts the silicon from the liquid and leaves a higher concentration of the remaining metal. The same phenomenon occurs more subtly in material systems of interest for TLI.

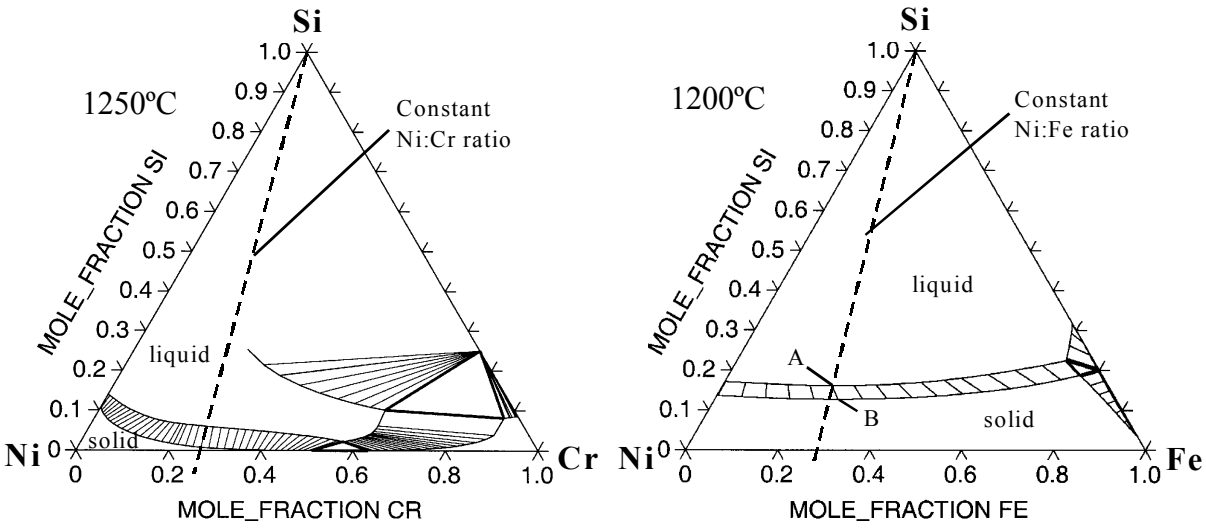

Figure 2.15: Ternary phase diagrams of Ni–Cr–Si and Ni–Fe–Si generated using Thermo–Calc with the Kaufman Binary Database. Solidification along tie lines not parallel to the line of constant ratio for non-MPD elements (from A to B in the Ni–Fe–Si system) results in a change of composition in remaining liquid.

Solidification in ternary systems progresses along tie lines that run from a liquidus curve to a solidus curve on the phase diagram. In the Ni–Fe–Si system in Figure 2.15, liquid at composition A would follow the tie line to composition B during solidification. Since the new composition at B has a higher ratio of nickel to iron, which it must draw from the melt, solidification along this path will deplete the remaining liquid of nickel. The effect is rather small in this case, and can be countered by diffusion of nickel from the melt supply to feed the depleted region, but the issue raises a concern about uniformity of composition in TLI of complex alloys. The Ni–Cr–Si has tie lines that run parallel to the line of constant Ni:Cr ratio, consequently solidification would not change the composition in the remaining liquid. In this manner, the appropriate selection of a materials system can be used to control the variation in composition. The additional limitation imposed on materials choice is an obvious disadvantage and would need to be weighed against the magnitude of the compositional variation and its resulting effect on properties.

Chapter 3: Experimental Results and Discussion

3.1 Diffusion couple to verify diffusivity

A diffusion couple was prepared between pure nickel and Ni – 9 at% Si to experimentally measure the interdiffusivity of Ni–Si. The two samples were polished to a mirror finish and then held together with the two smooth surfaces facing each other. The clamp mechanism was a C-shaped stainless steel block with a screw through one end to tighten against the samples, which had a contact area of ~0.2 cm^2. The entire assembly was heated at 5°C/min in a tube furnace under forming gas of 5% H_2 in argon and held at 1200°C for 1 hour, then cooled at the same rate. A perpendicular cross-section of the interface was polished and examined with an Electron Probe X-ray Microanalyzer. The results are shown in Figure 3.1, and the given diffusivity value of $1.5e^{-13}$ m^2/s was selected for the best fit of the experimental data to the theoretical error function solution for t = 3600s.

$$C = C_{ave}\left(1 + \operatorname{erf}\left(\frac{x}{\sqrt{4\tilde{D}t}}\right)\right) \tag{3.1}$$

The diffusivity value from literature at this temperature is $1.04e^{-13}$ m^2/s based on the parameters given in section 2.1.1. Some additional diffusion occurs during the slow heating and cooling, which could explain some of the difference. Considering the typical variability of diffusivity measurements, this agreement is fairly good. For consistency, further experiments are based on the predicted values from literature using D_o = 1.5 cm^2/s and Q = 258.3 kJ/mol and the relation $\tilde{D} = D_o \exp(Q/RT)$.

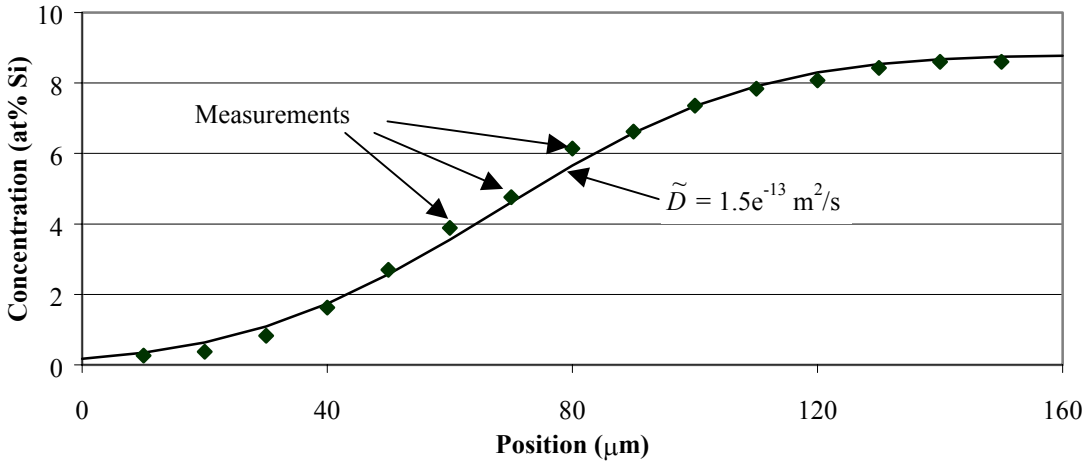

Figure 3.1: Microprobe analysis of diffusion couple for 1 hr at 1200°C and estimated $\tilde{D}$.

3.2 Measurement of solidification rate

3.2.1 Quenching experiments to observe solidification

The rate of solidification can be measured by observing the interface position in samples quenched at fixed time intervals. These experiments were conducted using a 1/8" diameter rod made of pure nickel, that housed a sample inside the tip. A small, ~1 cm deep hole was bored into the end of the rod, then the hole was filled with either loose Ni powder or a bundle of thin Ni wire and the assembly was fired to sinter the sample in place. The rod containing the sample was inserted through a fitting in the roof of a bench-top lab furnace so that the tip of the rod was held in the hot zone, a few centimeters above a crucible containing the infiltrant. After reaching the desired infiltration temperature, typically 1180°C, the rod was briefly dipped into the molten infiltrant so the liquid could wick into the void space of the sample as illustrated in Figure 3.2. Because the sample size is very small, the infiltration occurs nearly instantaneously. Diffusional solidification begins as soon as the liquid and solid come into contact with each other. After holding in the hot zone for a fixed period of time, the rod can be pulled directly out of the furnace. The rooftop fitting must have a slightly larger opening than the rod diameter to prevent the rod from getting stuck, particularly because some infiltrant may be attached to the rod. Upon removal, the rod continued to glow for only 2–3 seconds, giving an indication that the air quench caused the sample to cool at several hundred degrees per second. If a faster quench rate was desired, the sample could be dipped in an oil or water bath, but this was not deemed necessary.

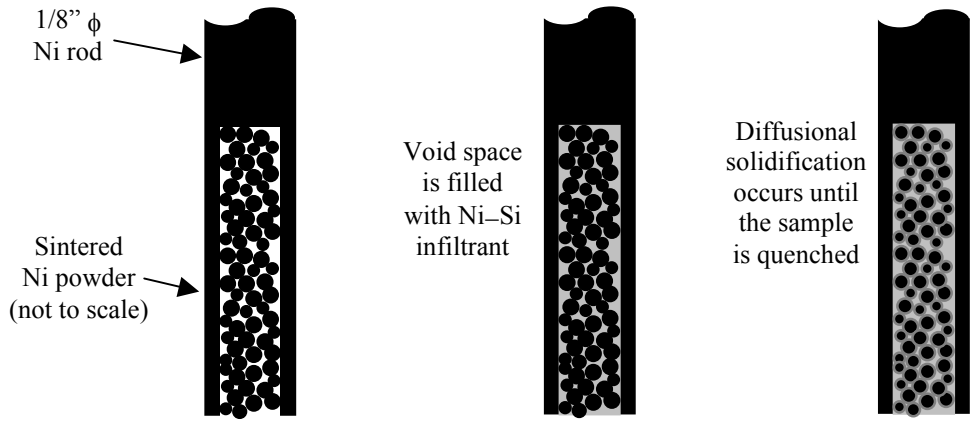

Figure 3.2: Schematic of quenching experiments designed to observe diffusional solidification rate.

The samples were cross-sectioned and examined metallographically to observe the location of the solid-liquid interface at the time of the quench. The microstructure is not visible after polishing alone, so an electrochemical etch (4:2:1 ratio of water:glacial acetic acid: hydrochloric acid) was used to facilitate viewing the microstructure. A current of 0.5 A applied for 5–10 seconds was sufficient to reveal the microstructure. Figure 3.3 shows two samples of infiltrated powder that were quenched after 10 seconds and 60 seconds of infiltration. The original Ni powder particles are clearly visible as the lighter colored circular shapes, and the regions with fine lamellar structure correspond to where liquid was present prior to the quench. The roughness of the interface is likely the result of the powder's original surface texture, as can be seen in Figure 5.2. The reaction zone visible between the powder and liquid is bordered by black lines. The outer line closest to the liquid corresponds to the location of the solid-liquid interface. Close examination shows a gradual darkening closer to the edge that matches an increasing silicon content when examined with a microprobe. The inner black line closest to the powder appears to have some depth when changing the focal plane of an optical microscope. This crevice seems to develop as a result of the electropolishing step, since it does not appear in the original polished samples.

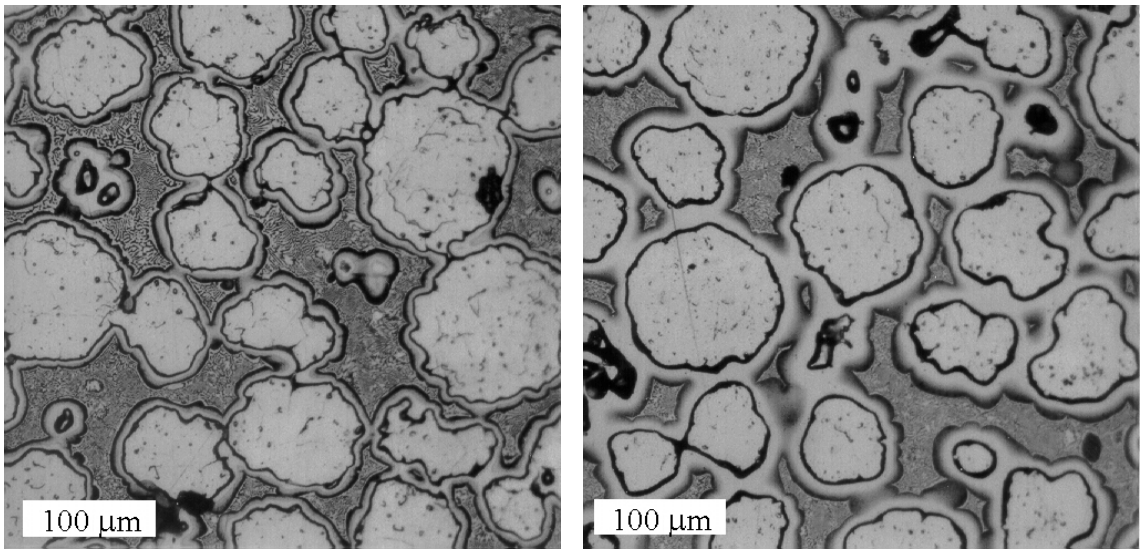

Figure 3.3: Ni powder infiltrated with Ni–Si at 1180°C and quenched after 10 sec (left) and 60 seconds (right).

There is a clear progression of the solidification between the two samples, which is observed most easily by an increasing width of the reaction zone between the liquid and powder. However, it can be difficult to interpret three-dimensional behavior when only looking at only two

dimensions. When viewing a cross-section through a sphere, one cannot assume that the cross-section cuts through the center of the sphere. The motion of the interface is likely not to be coincident with the viewing plane, in which case the results are difficult to interpret. Calculating the area fraction of the liquid, and therefore the volume fraction, would be the best method for measuring the solidification rate from a cross-section of powder. In lieu of this task, the quenching experiments were redesigned to infiltrate a bundle of thin wire, which allows simpler interpretation of the results by reducing the physical geometry to only two dimensions.

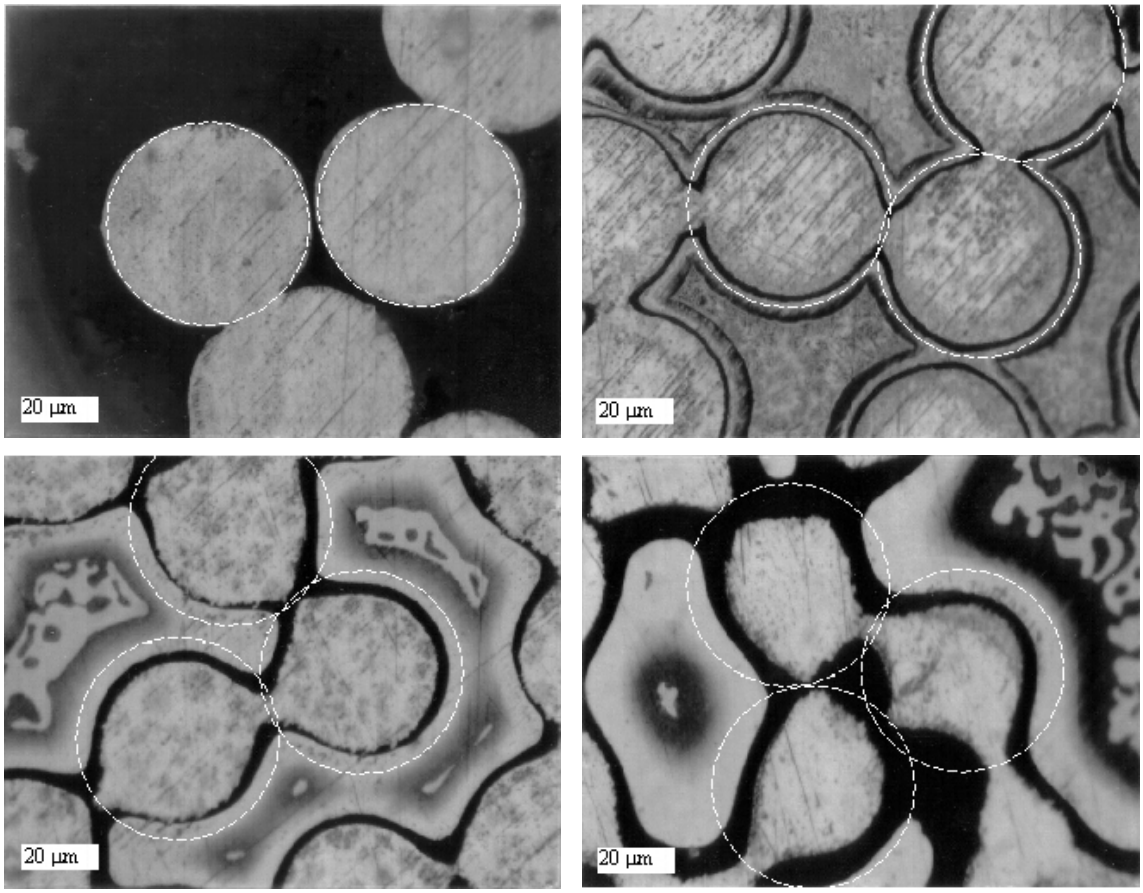

Figure 3.4: Ni wire bundles infiltrated with Ni–Si at 1180°C. Cross-sections of initial 50 μm wire embedded in epoxy (upper left), and infiltrated samples quenched after 10 seconds (upper right), 100 seconds (bottom left) and 300 seconds (bottom right).

Pure nickel wire was obtained from Alfa Aesar (stock# 10933) and wrapped numerous times around two ceramic posts held ~10 cm apart to form a bundle of the desired diameter. The bundle was twisted slightly to achieve relatively tight packing of the wires, and the assembly was lightly sintered to bond the wires together. Short segments of the bundle were then cut and placed into the end of a Ni rod as was done previously with powder. The results of these two-

dimensional quenching experiments are shown in Figure 3.4. The infiltrant was supplied at the eutectic composition of 21 at% Si, and a small amount of initial dissolution could occur because the liquidus concentration at 1180°C is only 19.8 at% Si. Using equation 2.22, this would cause 2–4% of the wire to be dissolved into the liquid depending on the packing fraction. For the 50 μm diameter wire, that corresponds to only a 0.5 μm interface motion, which is considered to be negligible in light of uncertainties in material composition and processing temperature.

The same electropolish was used to reveal the microstructure, and the interface motion can be easily determined and referenced to the initial wire diameter. The white dashed lines have been superimposed on each of the micrographs to designate the original diameter of the wire. The black crevice within the white circle is again an artifact of the electropolish. It generally coincides with the distance to which silicon has diffused towards the center of the wire. In the last sample in the time sequence, there is no liquid remaining between the close-packed wires, only a small region on the left and a larger region in the upper right where there was larger spacing between wires. The lamellar structure designating the presence of liquid appears slightly more coarse for the wire experiments in Figure 3.4 than for the experiments with powder in Figure 3.3, although they are shown at a higher magnification.

Microprobe analysis was conducted on these samples to examine the concentration profile of silicon across the diffusion zone. The plot below shows the results of linescans starting from the pure nickel interior, traversing perpendicular to the interface toward the liquid region. The original wire diameter was not referenced during the linescan, so the position is somewhat discretionary, but the plots have been adjusted to the left or right so that they cross the initial interface position near $C_s/(1+\mathrm{erf}(\beta))$, as predicted by the theory and shown in Figure 2.4.

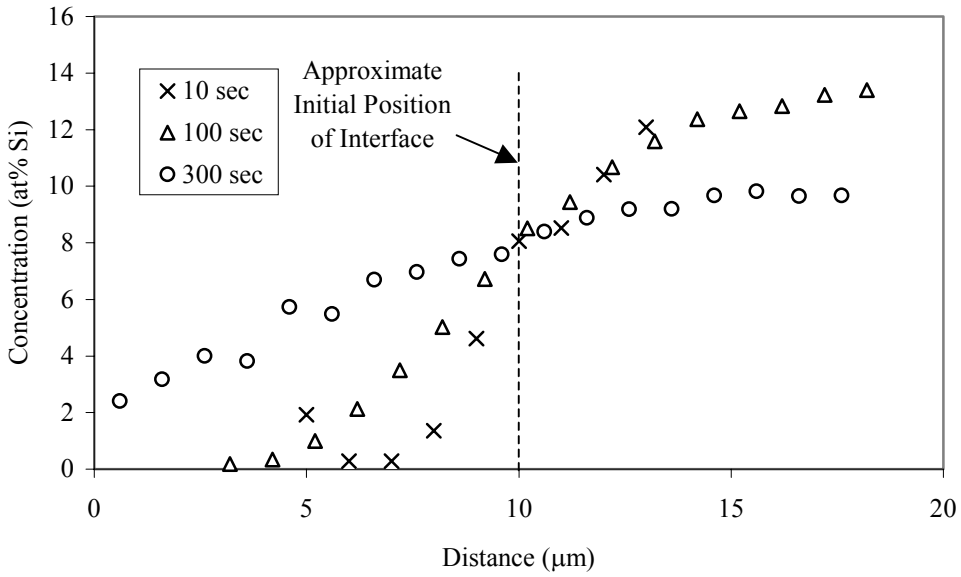

Figure 3.5: Microprobe concentration measurements of wire bundle quenching tests.

These measurements can be compared to the diffusional solidification predicted by theory and the numerical simulation results shown in Figure 2.4. The observed diffusion occurs slightly faster than expected, evidenced by the more gradual slope in Figure 3.5. After 400 seconds, the theory predicts a difference in concentration from 4% to 12% over the 10 μm centered around the initial interface. The observed concentration difference over the central 10 μm is roughly between 6% and 10%, suggesting that more interdiffusion has occurred despite the shorter time of only 300 seconds.

3.2.2 Quantification of the solidification rate

The solidification rate is most easily quantified by tracking the interface motion. For each of the 3 quenched samples, the motion of the interface was estimated by measuring its position relative to the original wire diameter using the micrographs in Figure 3.4. Several measurements were taken from different areas of each sample and the values averaged. The observed outward growth in wire radius was 3.4, 7.5, and 13.4 μm for the samples quenches at 10, 100 and 300 seconds. Since this growth should theoretically be equal to $\beta\sqrt{4\tilde{D}t}$ for planar motion, the results can be used to measure the effective solidification rate coefficient β for the material system.

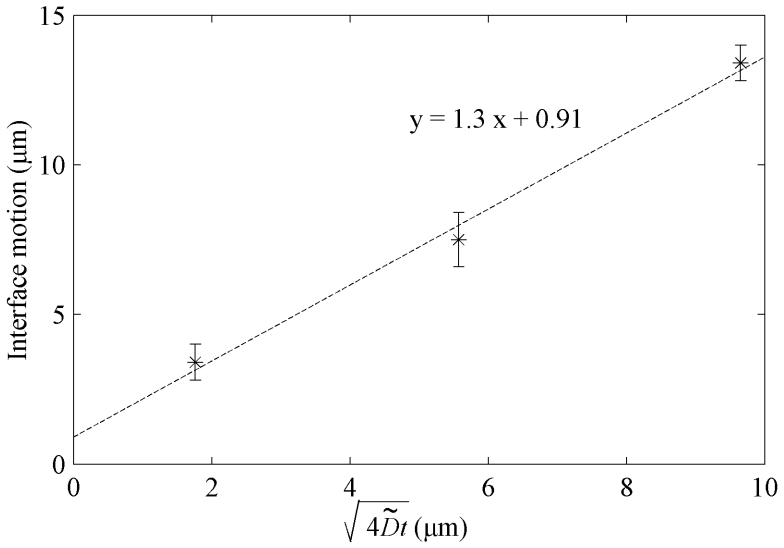

Figure 3.6: Estimation of solidification rate coefficient from interface motion in quenched samples. Error estimates are based on multiple measurements of interface motion at different locations.

The slope of the linear regression shows the measured value of β equal to 1.3, and the non-zero intercept could correspond either to an offset from the nominal wire diameter or a small amount of solidification that could occur during the quench. Forcing a zero intercept would result in only a small increase in β. These experiments show that the solidification rate is approximately twice as fast as expected at this temperature based on a diffusivity at this temperature of $7.76e^{-14}$ m^2/s and β of 0.59 calculated in Chapter 2.

3.2.3 Discussion of observed solidification rate

The solidification rate is specified in terms of both the coefficient β, which affects the rate linearly, and the diffusivity, which only has a square-root effect. When comparing experimental results with theory, it is most convenient to discuss the difference in terms of β, because the diffusivity can still be expressed in terms of temperature by the parameters in literature. However, it would also be possible to fix the β value predicted by the concentration ratio and determine an effective diffusivity that corresponds to the observed solidification rate. Indeed, this is more realistic since the value of β is determined by solid solubility and two-phase field width, both of which should not change. The diffusivity is more likely to vary under different material conditions, as discussed below. For simplicity, β is described as the adjusted term in matching

the observed solidification behavior to $\sqrt{4\widetilde{D}t}$, keeping in mind that the solidification rate is really characterized by the product of the two terms $\beta \cdot \sqrt{\widetilde{D}}$.

Several other researchers have observed significantly faster diffusional solidification than predicted by theory when analyzing interlayer width in transient liquid-phase bonding. Both Tuah-Poku *et al*[22] and MacDonald and Eagar[16] observed isothermal solidification times more than four times faster than expected in Cu–Ag sandwich joints. Due to the square-root dependence on time, this means the solidification rate is more than twice the expected value. The most likely explanation for the faster rate is the influence of grain boundaries on the effective diffusivity into the solid as well as grooving at the interface that increases the contact area. Several studies of diffusion bonding using both Ni–P and Ni–B filler metals have shown a significant increase in solidification rate as the grain size of the solid is decreased.[23,24] The presence of the liquid phase and its ability to penetrate grain boundaries and alter the surface characteristics make the effect even more pronounced than for diffusivity increase with grain refinement in solid alone. In a study by Saida *et al,*[25] the effective diffusion coefficient measured for solidification of Ni–P at 1423°K increased from $1.4e^{-14}$ m^2/s into both single-crystal and coarse-grained nickel, to $2.2e^{-14}$ m^2/s into nickel with a relatively fine grain size of 480 μm. The exact grain size of the wire is unknown, but it is likely polycrystalline and therefore smaller than the 50 μm wire diameter. Grain boundary effects are likely responsible for most of the observed increase in solidification rate.

Several other experimental factors may effect the observed solidification rate. The effect of cylindrical geometry is addressed in section 2.2.3 and would slightly reduce the predicted rate of solidification. For the 50 μm diameter cylinder, the deviation from the planar solution would be less than 10% over the solidification range studied. The cylindrical geometry can not explain any of the difference between observed solidification rate and the theoretical prediction because it influences the solidification rate in the opposite direction as the observed discrepancy.

Because the microstructure can transform during cooling, observations of a eutectic phase in a room-temperature micrograph do not necessarily represent the presence of liquid at the infiltration temperature. For slow cooling conditions, off-eutectic liquid will begin to solidify first in solid solution until the eutectic temperature is reached. The result would be an observed eutectic area that is smaller than the actual liquid area at the infiltration temperature. If the

sample were cooled instantaneously, the liquid would transform directly into a lamellar phase that would appear similar to the eutectic, but with an average composition equal to the original liquid, not the concentration at the eutectic. Saida *et al*,[25] observed different microstructure in samples quenched in air, oil, and water, with the water-quenched samples providing the closest match between the observed microstructure and the liquid width. The air and oil quenched samples followed more closely to the slow-cooling case, although the sample size was 1.2 cm diameter so the cooling rate associated with the air quench will be significantly less than for the 1/8" Ni rod. A description of the transformation from eutectic width to liquid width is provided for reference in the following section, and the difference in width becomes more significant as the liquid composition moves farther away from the eutectic. Since the wire quenching experiments were conducted close to the eutectic temperature and the concentration difference was small, no such transformation was necessary. For the images in Figure 3.3 and Figure 3.4, the eutectic areas can be assumed to represent all of the area that was liquid prior to quenching.

It is worth noting that the measurement of interface motion in the wire bundle experiments achieves the same objective of the planar measurements of isothermal solidification commonly presented in the context of diffusion bonding. In these cases, the eutectic width is measured and plotted against the square root of time to estimate the total solidification time. Since the eutectic and liquid widths are directly proportional, either plot would extrapolate to the same time. In the wire experiments, the growth of the solid phase is measured instead, since the remaining liquid or eutectic phase does not have a characteristic width, but would need to be measured as an area fraction. If quenching rates were insufficient and liquid concentration varied significantly from the eutectic, then the actual growth rate of the solid would be difficult to determine because it would need to account for the liquid to eutectic transformation. Failing to account for this difference would lead to overestimation of the initial solidification rate. In such cases, it might be preferable to design a planar experiment to determine the solidification rate.

3.2.4 Relating observed eutectic width to original liquid width

Due to material phase changes that occur during cooling, the observed microstructure at room temperature often does not correlate directly to the phases present at a given temperature. If the material has sufficient time to remain at equilibrium during the cooling process, then room temperature observations can be correlated to high temperature conditions based on the equilibrium phase diagram. Figure 3.7 shows a generic phase diagram and is used to illustrate how room temperature observations can be translated to conditions at elevated temperatures.

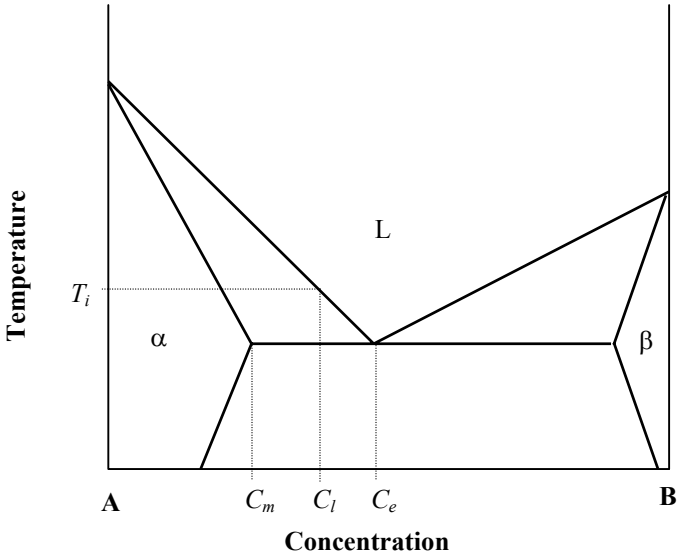

Figure 3.7: Generic phase diagram used to relate eutectic width to liquid width.

As the liquid of a concentration C_l is cooled below the infiltration temperature T_i, it begins to solidify as α and the remaining liquid increases in solute content by conservation of mass. For the one-dimensional case, when the eutectic temperature is reached the relative widths of the α phase w_α and the eutectic liquid w_e can be determined by the Lever rule.

$$\frac{w_\alpha}{w_e} = \frac{C_e - C_l}{C_l - C_m} \tag{3.2}$$

where C_m, C_l, and C_e are the concentrations of maximum solid solubility, the original liquid, and the eutectic. Since the width of the original liquid, w_l is equal to the sum $w_\alpha + w_e$, it can be estimated from the eutectic width, which is easily observed in micrographs at room temperature.

$$w_l = w_e\left(1 + \left(\frac{C_e - C_l}{C_l - C_m}\right)\frac{\rho_e}{\rho_l}\right) \tag{3.3}$$

where ρ_e and ρ_l are the density at the eutectic and original liquid concentrations.[26] The density ratio can be set to unity when concentration differences are small and the two densities are nearly equal. The two widths can be replaced by area fractions if the geometry is not one-dimensional.

3.3 Gated infiltration

Physical separation of the infiltrant and skeleton before the start of the infiltration prevents premature diffusion of the melting point depressant. Using some type of gate to actively control the introduction of the liquid to the skeleton allows the liquid to reach a thermal and chemical equilibrium prior to contacting the skeleton and enables very short infiltration times. The first

type of gating mechanism implemented was by suspending the part above the melt, and then dipping the part. This had the added benefit of allowing the measurement of the infiltration rate, but required modification to the part typically by drilling holes in it. Another gating mechanism that was successfully implemented was to place a movable wall between the part and the melt. The wall was made of ¼" thick bisque-fired alumina and was shaped to mate with the walls of the alumina crucible. Since both materials were non-wetting to the infiltrant, a gap of up to ~1 mm was tolerable without the liquid head to causing any leaks. The large rectangular part shown in Figure 3.8 was made using this gating mechanism. Many different methods can be envisioned, but one simple, robust method was tested by placing the melt inside a ceramic tube that rested vertically with one end facing flat on the bottom of the crucible, this successfully contained a melt and the tube could be lifted to introduce the melt to a skeleton resting nearby.

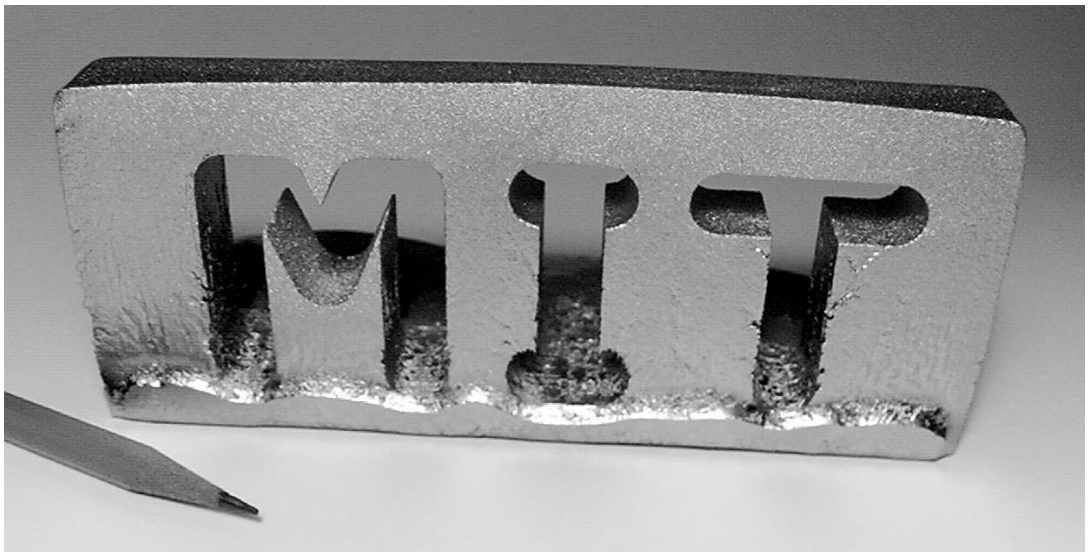

Figure 3.8: This large rectangular part composed of 50–150 μm powder was made in March of 2000 as a proof of concept for TLI.

3.4 Erosion and melt saturation methods

The root cause of erosion is the dissolution of the skeleton material in the liquid infiltrant. In order to reach an equilibrium state at the solid-liquid interface, the infiltrant wants to move towards its liquidus composition and the skeleton wants to move towards its solidus composition. Since the diffusivity is much faster in the liquid, it will absorb nickel from the skeleton until it is saturated and reaches its equilibrium liquidus composition. For a large melt pool, more nickel must be absorbed to achieve the same change in concentration, and the erosion is more severe.

Figure 3.9: Erosion of part on left caused by dissolution of skeleton material by unsaturated melt pool. Part on right shows no evidence of erosion infiltrated using saturated liquid, with some dendrites stuck to the part from the semi-solid infiltrant pool.

Saturating the melt before it contacts the skeleton can minimize the erosion as illustrated in Figure 3.9. Presaturation consists of ensuring the supply of liquid is already at the equilibrium liquidus concentration. Since it would be difficult to control the exact composition and temperature, Figure 3.10 shows how the proper amount of excess nickel can be chosen to allow for process variation. If the desired infiltration temperature were 1180°C, eutectic Ni–Si and excess nickel would be combined to allow for a generous window of +/- 20°C. The composition of the mixture would be chosen at the liquidus of the upper temperature limit and the quantity of the mixture would be chosen based on the Lever rule at the lower temperature, making sure that sufficient liquid would always be available to fill the skeleton. For the case in Figure 3.10, the infiltrant composition would be 9.9 wt% Si to ensure saturation even if the actual temperature reached 1200°C. If the actual temperature were only 1200°C, then approximately 70% of the supplied infiltrant would be liquid based on the lever rule. Note that since the liquid is saturated, there is no disadvantage to having extra infiltrant (other than wasted material).

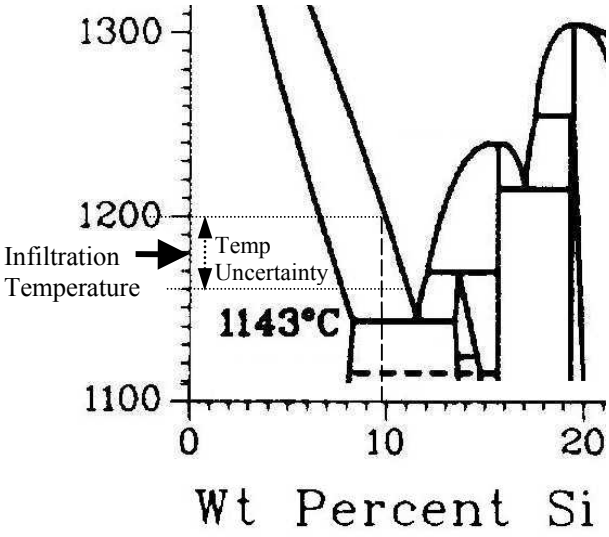

Figure 3.10: Presaturation of infiltrant supply to prevent dissolution.

Initially, the desired infiltrant composition was achieved by mixing pure nickel powder in with available chunks of infiltrant alloy at the eutectic composition. Once a consistent infiltration temperature was selected, typically 1185°C, a new batch of infiltrant was made at 10.2 wt% Si, slightly less Si than the equilibrium liquidus concentration. To promote uniform mixing of the infiltrant, the melt was heated above the infiltration temperature and then slowly cooled to below the liquidus. The top sample in Figure 3.11 was infiltrated with a presaturated melt containing excess nickel. The bottom sample used a similar presaturated melt, but was heated above its liquidus and then cooled to the infiltration temperature. Very little erosion can be seen on the bottom sample, perhaps due to better mixing within the melt.

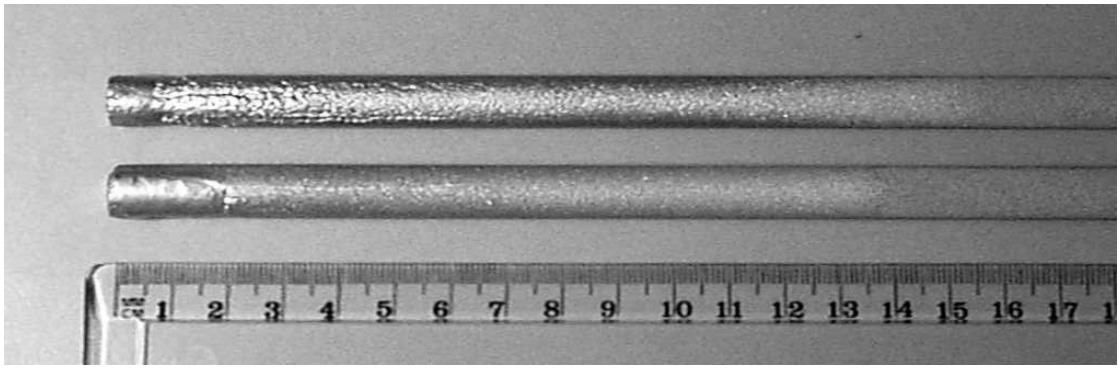

Figure 3.11: Reduced part erosion through better mixing of infiltrant. Bottom sample involved overshooting the infiltration temperature to enhance mixing.

In some cases, presaturating the infiltrant worked well to prevent dissolution at the base where the part is submerged in liquid, but did not eliminate the 'riverbeds' running up the part surface. Referring back to the discussion of heat release in section 2.3, equations 2.20 and 2.22 can be used to determine the expected increase in part temperature and corresponding dissolution for these experimental conditions. Using a solidification time of 60 seconds, which would be appropriate for smaller powder size, the temperature increase would be ~150°C causing dissolution of 50%. For a solidification time of 300 seconds, more appropriate for larger powder, the temperature increase would be ~50°C causing dissolution of only 7% of the skeleton. These numbers are only rough estimates, but are considerably higher than expected based on the degree of erosion visible on infiltrated parts. Figure 3.12 shows a sequence of infiltrations using successively larger powder sizes. The erosion is clearly more severe in the skeletons of small powder size.

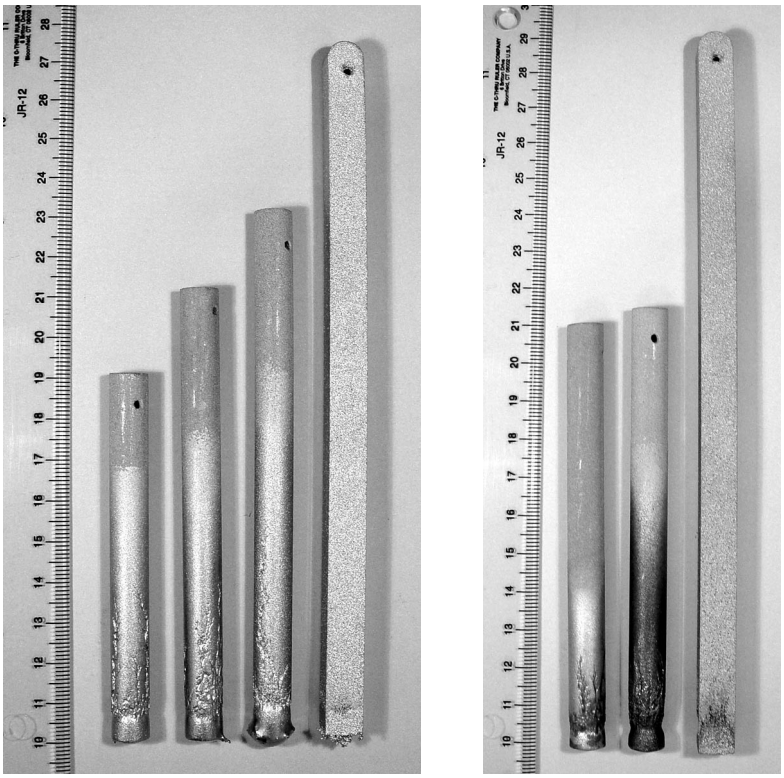

Figure 3.12: Set of infiltrated nickel powder skeletons showing more erosion on skeletons of smaller powder size. Left photo shows infiltration with Ni–Si (63–74, 90–104, 125–150 and 250–300 μm powder from left to right). Right photo shows infiltration with Cu (63–74, 90–104 and 250–300 μm powder from left to right).

3.5 Measurement of variation in composition

The resulting composition throughout an infiltrated part was measured by cutting small sections from different points along the infiltration path. The samples were sent to Massachusetts Materials Research in West Boylston, MA for analysis by Inductively Coupled Plasma (ICP). Figure 3.13 highlights the segments of the infiltrated part that were analyzed and the measured composition. The serpentine part shape was used to test longer infiltration distances inside of a small furnace chamber that was used at the time.

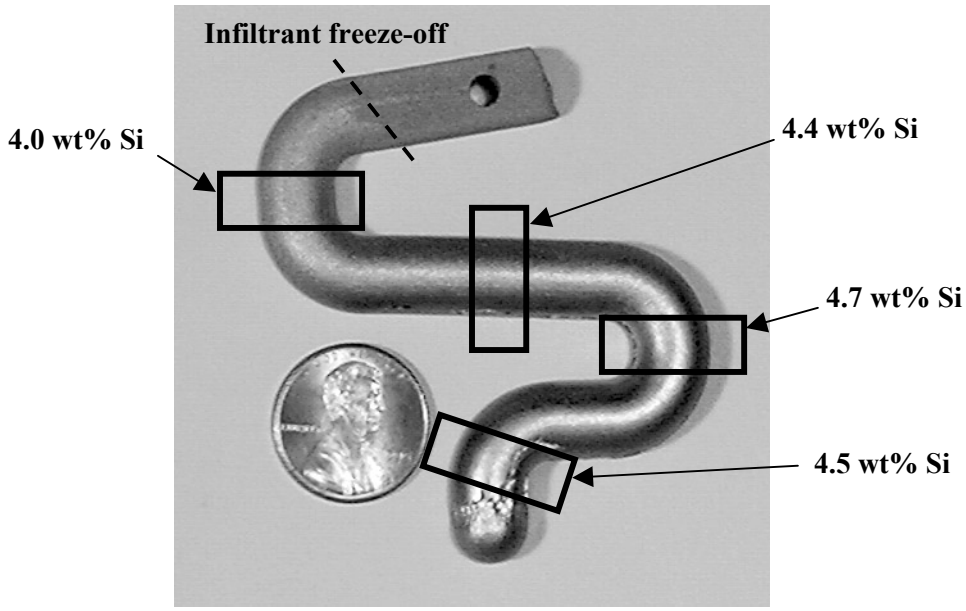

Figure 3.13: Infiltrated part sectioned and tested for compositional variation.

The part shown in Figure 3.13 used a 50–150 μm powder skeleton and was infiltrated at 1160°C using eutectic Ni–Si with excess Ni powder added to the melt for presaturation. With a spacing of ~3 cm between each tested specimen, the variation along the path of infiltration is fairly small. The farthest point along the infiltration path exhibits a slightly lower silicon concentration, but is also very near the point of infiltrant freeze-off. Greater residual porosity in this area would also cause a decrease in bulk silicon concentration, a different mechanism than that of mass transport in the liquid discussed in section **2.4**.

3.6 General dependence of penetration distance with powder size

The specific influence of powder size on the fluid flow and solidification rate is discussed in much greater detail in Chapters 4 and 5, but will be discussed briefly here along with experimental observations. The diameter of the powder affects both the fluid flow and the

amount of time before the infiltrant freezes. For both reasons, larger powder size provides a desirable effect of improving the distance that the infiltrant will penetrate. Larger powder lowers the viscous drag and allows the infiltrant to fill the skeleton faster, and it also decreases the surface area for diffusion providing more time before the porous network is closed off. Both Figure 3.12 and Figure 3.14 clearly show how the infiltration height can be controlled by the powder size of the skeleton. Through the use of progressively larger powder size, we have achieved infiltration heights greater than 20 cm in both the Ni–Si and the Ni–Cu materials systems.

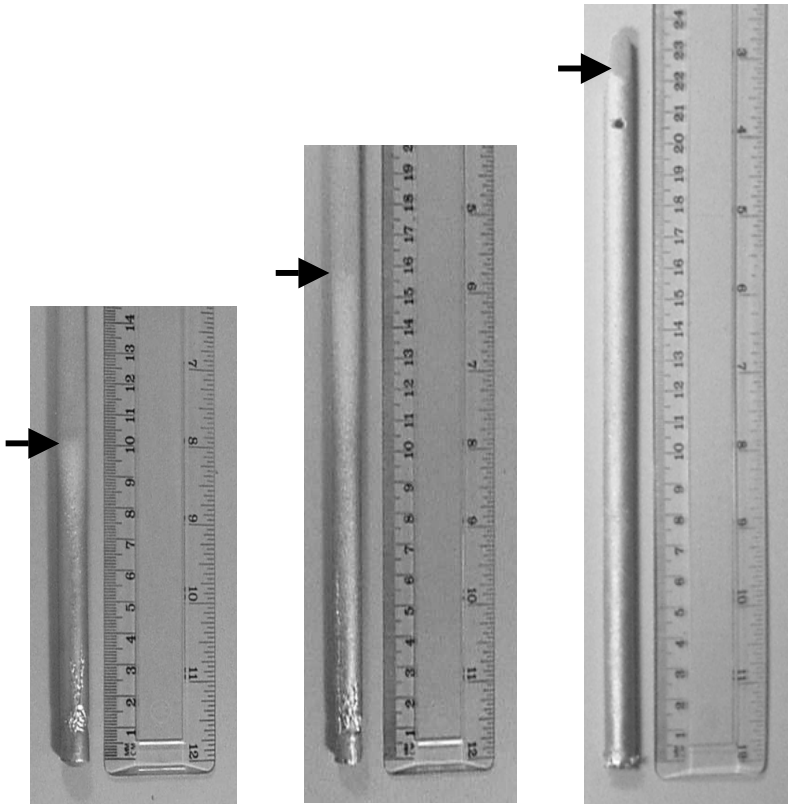

Figure 3.14: Infiltration heights achieved using progressively larger powder sizes: 50–150 μm, 150–300 μm, and >300 μm

3.7 Homogenization, porosity and mechanical testing

3.7.1 Homogenization

Samples were typically cooled at 5°C/min immediately after infiltration. Very little homogenization had taken place at this stage. Even after being held for 1 hour at the infiltration temperature, the left-hand image of Figure 3.15 shows how considerable microscopic variation in composition remains. After subsequent heat treatment at 1200°C for 5 hours, the material

appears homogeneous, but localized pockets of residual porosity remain in areas that could correspond with the original locations of powder particles. A similar sample was heat treated at the same temperature for 12 hours and appears to have become more homogeneous and does not show as much evidence of porosity. Microprobe analysis shown in Figure 3.16 confirms the optical microscope observations.

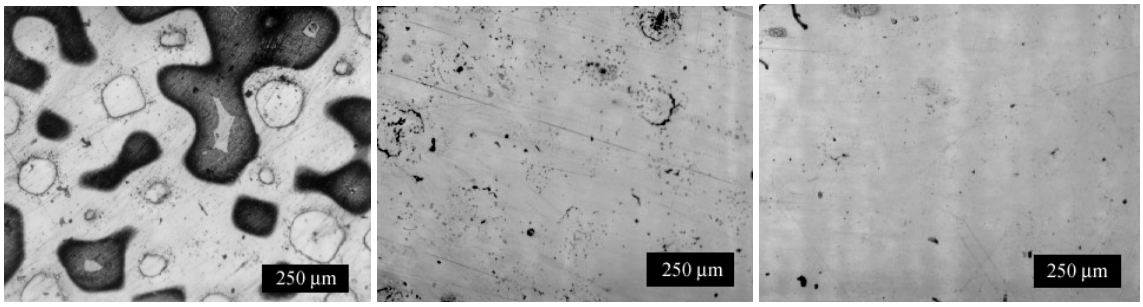

Figure 3.15: Homogenization of 250–300 µm infiltrated powder after 1 hr @ 1180°C, 5 hrs at 1200°C, and 12 hrs at 1200°C.

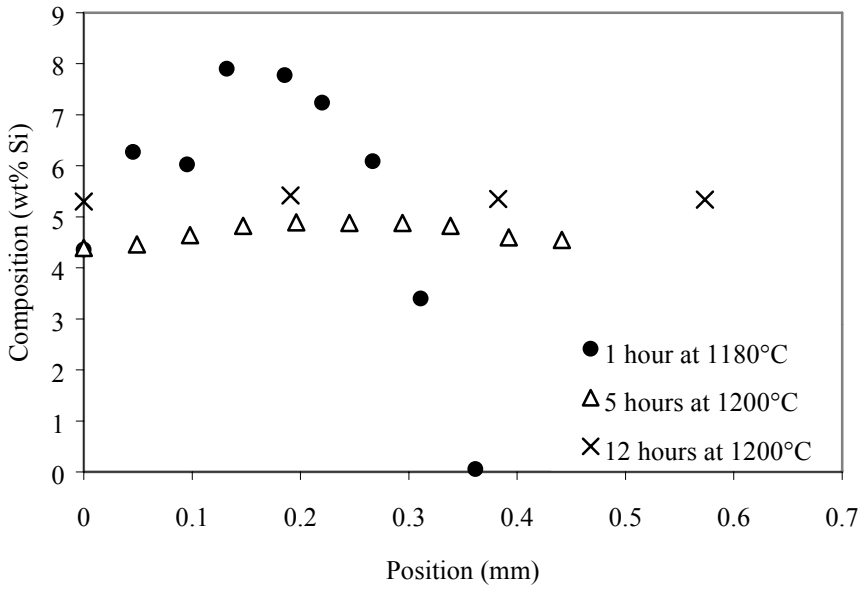

Figure 3.16: Microprobe analysis of homogenization in samples from previous figure.

3.7.2 Residual porosity and measurement of density

The existence of residual porosity in a final part can be detrimental to its mechanical properties.

Typical sources of porosity in castings include voids from solidification shrinkage and gas evolution. In TLI, the solidification shrinkage can not be fed from remaining liquid as occurs from risers in traditional casting. In addition, the mass transport of the melting point depressant into the skeleton during TLI could lead to Kirkendall porosity. For example, the differential diffusivities of Si and Ni results in more silicon being transported into the skeleton than nickel into the regions that were liquid. Fine-scale porosity could result and have an adverse impact on the mechanical properties of the final part.

The density of infiltrated samples as well as cast chunks of infiltrant where measured using fluid displacement and the Archimidean principle.[27] The infiltrated samples typically do not have any open porosity, so the density of a given sample can be determined by a dry mass measurement and the volume displaced when the sample is submerged in water, which is measured by change in weight and the known fluid density. The results of the density measurements are included in Table 3.1. Samples A and B were tensile tested before density measurements were taken, so no data is available for the specific sample. Three other samples in similar as-infiltrated condition had measured densities of 8.16, 8.01, and 8.02 g/cc.

Homogenized samples of Ni–Si were heat treated at 1200°C for 12 hours. Ni–Cu samples were heat treated at 1100°C for 12 hours and then at 1200°C for 12 hours. The initial heat treat was done at the infiltration temperature for copper to provide time to complete isothermal solidification and begin homogenization so that the higher temperature did not melt any portion of the sample. After homogenization treatment, some samples were additionally sent to Bodycote IMT in Andover, MA for a 4 hour Hot Isostatic Press (HIP) treatment at 104 Mpa (15 ksi) and 1163°C (2125°F). This process is typically used to help remove porosity in high-performance castings used in the aerospace industry. Parts are processed in large batches and the cost is typically a few dollars per pound.

3.7.3 Tensile test results and HIP Treatment

Sample	Material Composition	Condition	Elastic Modulus (GPa)	Yield Stress (MPa)	UTS (MPa)	Max Strain (%)	Density (g/cc)
A	Ni – 4 wt% Si	Infiltrated	230	156	250	4.6	
B	Ni – 4 wt% Si	Infiltrated	200	184	230	1.4	
C	Ni – 4 wt% Si	Homogenized	275	133	230	6.4	
D	Ni – 4 wt% Si	Homogenized	220	118	201	4.1	7.97
E	Ni – 4 wt% Si	Hot Isostatic Pressed	200	200*	423	34	8.49
F	Ni – 4 wt% Si	Hot Isostatic Pressed	210	152	436	41	8.50
G	Ni – 4 wt% Si	Cast	400	123	400	30	
H	Ni – 4 wt% Si	Cast and Homogenized	210	162	370	64	8.53
I	Ni – 10 wt% Si	Cast	300	n/a	480	0.2	
C1	Ni – 40 wt% Cu	Homogenized	100	75	133	5.3	7.42
C2	Ni – 40 wt% Cu	Hot Isostatic Pressed	120	87	158	11	7.68

Table 3.1: Tensile test results and density measurements.

Tensile bars were machined to the specifications[28] of ASTM 12.7 mm wide sheet specimens and varied in thickness from 2.5 mm to 4 mm. Sample gauge length was 50.8 mm and an extensometer with 12.7 mm gauge length was mounted on the sample for more accurate measurement of strain and therefore modulus. The elastic behavior of all the specimens was very similar, with no marked difference in the elastic modulus, even for the samples tested prior to homogenization. The yield stress was also within a reasonable range such that no clear distinction can be made between the various conditions. The samples tested prior to homogenization actually showed the highest yield strengths. Sample E is marked with an * to denote that slipping occurred at the grips and the specimen was unloaded for repositioning, then reloaded prior to yield and the posted result is therefore somewhat questionable.

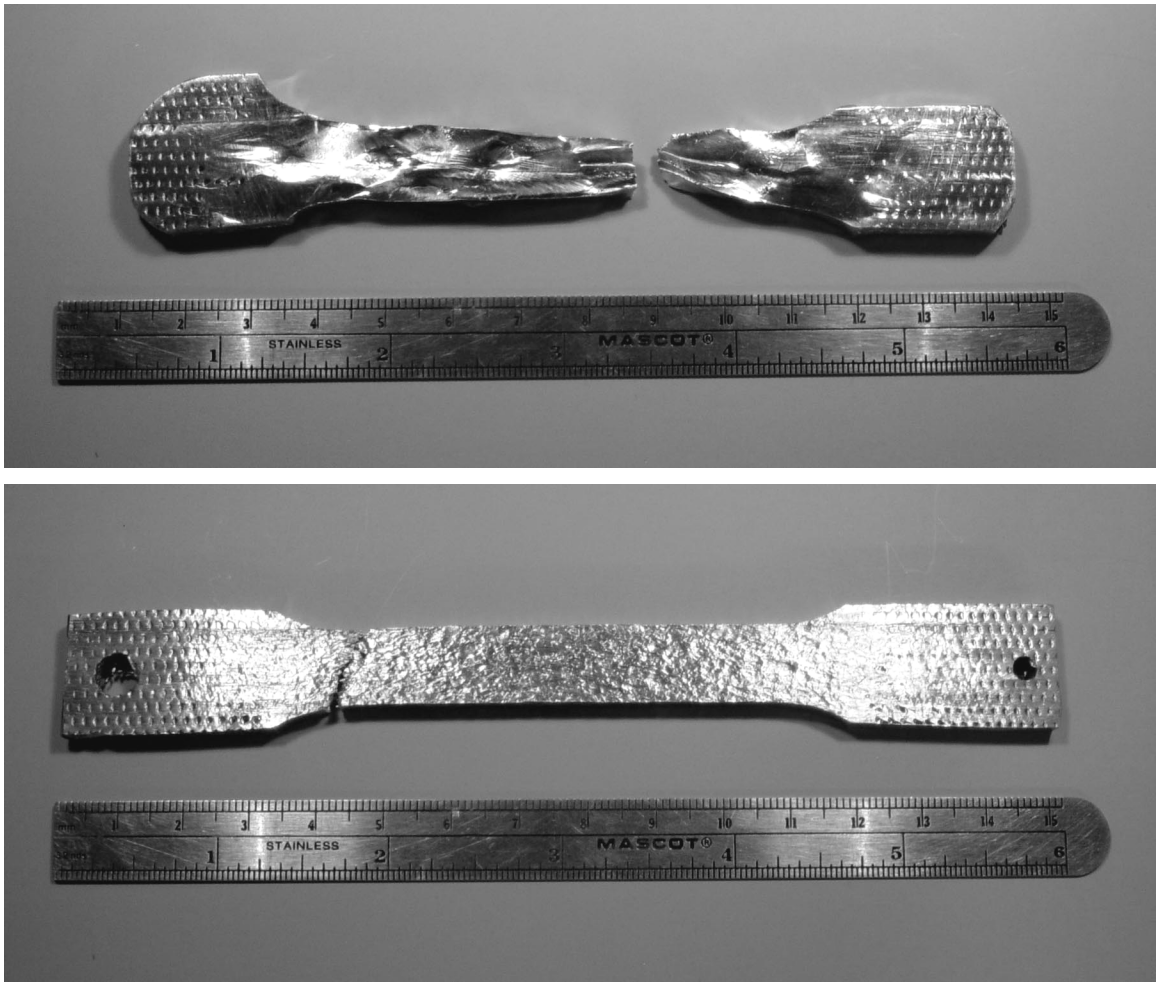

Figure 3.17: Tensile bars of homogenized Ni – 4 wt% Si after elongation and failure. Grain size in cast sample (top, H) is visibly ~1 cm, while infiltrated bar (bottom, F) has much finer grains, but exhibits similar tensile behavior.

The most significant observation of the tensile tests is the premature failure of the infiltrated samples when compared to the cast samples, which underwent 30–60% elongation before failure. The 4–6% elongation of the infiltrated and homogenized sample may not be considered brittle, but they failed prior to the substantial strain hardening that was observed in the cast sample. The HIP treatment appears to have succeeded in removing residual porosity from the homogenized samples, which would correspond to ~5% in the samples prior to HIP treatment if the cast sample is considered fully dense (the theoretical density of Ni – 4 wt% Si is not published). Figure 3.17 contrasts the grain size observed between the cast sample and the infiltrated sample after HIP treatment. The tensile behavior of both samples was similar, but the smaller grain size of the sample made by infiltration actually provides the advantage that the deformation is more likely to be distributed evenly throughout the part.

Chapter 4: Infiltration of Liquid into Porous Media

4.1 Surface tension and capillarity

Surface tension provides the driving force for capillary infiltration of liquids into porous media. Significant capillary pressure develops under proper wetting conditions because of the small length scales involved and the subsequently high curvature at the liquid interface. The magnitude of the capillary pressure can be determined by balancing the work exerted by the fluid over a given volume with the change in surface energy associated with the change in interfacial area, $\Delta P \cdot dv = \gamma \cdot dA$. For the simplest case of a spherical interface, the capillary pressure inside a sphere of radius r is equal to $2\gamma_{LV}/r$ where γ_{LV} is the liquid/vapor interfacial surface energy.[29] In porous media, the capillary pressure can similarly be calculated based on the surface area to volume ratio of the pore space.[30]

$$P_c = \left(\gamma_{SV} - \gamma_{SL}\right) \cdot \frac{dA}{dv} \tag{4.1}$$

The term in parenthesis represents the change in surface energy associated with the solid surface previously exposed to vapor that is now covered by liquid. This term can also be represented by an equilibrium wetting angle and the liquid/vapor surface tension. The wetting angle is defined by the magnitude of the interfacial surface tensions by $\cos(\theta) = \left(\gamma_{SV} - \gamma_{SL}\right)/\gamma_{LV}$.

For a sintered skeleton composed of powder with a reasonably narrow size distribution, the geometry can be approximated as a bed of spheres with uniform diameter D. This allows straightforward calculation of the surface area to volume ratio of the pore space. The specific surface S of the skeleton is the surface area per unit volume of solid, which is then related to the volume of pore space through the skeleton void fraction ε:

$$S = \frac{4\pi\left(\frac{D}{2}\right)^2}{\frac{4}{3}\pi\left(\frac{D}{2}\right)^3} = \frac{6}{D} \qquad \text{and} \qquad \frac{V_{solid}}{V_{pore}} = \frac{1-\varepsilon}{\varepsilon} \tag{4.2}$$

Since the capillary pressure is dependent upon the surface area to volume of the pore space, not the volume of the solid, it is defined as:

$$P_c = \gamma_{LV} \cos(\theta) \cdot \frac{6(1-\varepsilon)}{D\varepsilon} \tag{4.3}$$

This can be used to determine the maximum height a liquid will rise within a skeleton by setting the capillary pressure equal to the gravitational head of the liquid column, $\rho g h$.

4.2 Viscous flow and permeability

4.2.1 General theory of flow in porous media

The flow of liquid through porous media is restricted by viscous drag due to the no-slip boundary condition and the high specific surface area of powder. The geometry of a specific porous medium is represented by a permeability K that is the proportionality constant between the pressure gradient and the volume-averaged velocity of the fluid in the viscous dominated flow regime:

$$-\nabla P = \frac{\mu}{K} V \tag{4.4}$$

where P is fluid pressure, μ is the fluid viscosity, and V is equal to the flow rate divided by the total cross-sectional area. The permeability K will be discussed in greater detail in section 4.2.3. V is often referred to in literature as seepage velocity and is also equal to the velocity of the infiltration front times the void fraction. As an example, a flow rate of 1 cc/sec through a skeleton with 1 cm^2 cross-sectional area and ε=0.4 would correspond to V equal to 1 cm/s, but the velocity of the infiltration front would equal 2.5 cm/s. This equation, known as Darcy's Law, is a simplification of the general momentum equation for cases when the two given terms dominate over any inertial terms. For example, the contribution of fluid acceleration to the momentum equation would be of the order $\rho V/t_o$, where ρ is the fluid density and t_o is a characteristic time for the process. Comparing this term to the right-hand term of equation 4.4, the acceleration term will only be significant for $t_o < K\rho/\mu$. Because the permeability of even very coarse powder (300 μm) is less than 10^{-10} m^2 and the ratio ρ/μ for liquid metals is less than 10^7 s/m^2, the acceleration term becomes insignificant after 1 ms.[31]

As fluid flow velocity increases, the form drag can begin to impact the flow characteristics. This is represented by the Forchheimer equation, an extension of Darcy's Law:

$$\nabla P = -\frac{\mu}{K} V - \frac{c_F}{\sqrt{K}} \rho V^2 \tag{4.5}$$

where c_F is a dimensionless form-drag constant dependent on geometry and equal to 0.55 for spherical particles.[31] More detailed analysis suggests an increase of c_F with greater surface roughness and packing fraction.[32] The comparison of the two right-hand terms can be used to determine a critical velocity in terms of a Reynolds number with length scale $\sqrt{K}$, below which the Forchheimer term becomes important.

$$\frac{\frac{c_F}{\sqrt{K}}\rho V^2}{\frac{\mu}{K}V} = c_F \frac{\rho V\sqrt{K}}{\mu} = c_F \cdot Re_K \tag{4.6}$$

The influence of the Forchheimer term can be more easily explained by reference to Figure 4.1, which plots the Forchheimer equation divided through by $\rho V^2/K^{½}$ and represented as a friction factor f_K, taken from Nield and Bejan.[31] For Reynolds numbers above unity, the friction factor begins to levels off at c_F, rather than continuing to follow the extrapolation of $1/Re_K$ predicted by Darcy's Law. Since the velocity (shown as v in the figure, but this is the same as V) is inversely proportional to the friction factor, the Forchheimer equation would predict a slower velocity than Darcy's Law for the same conditions.

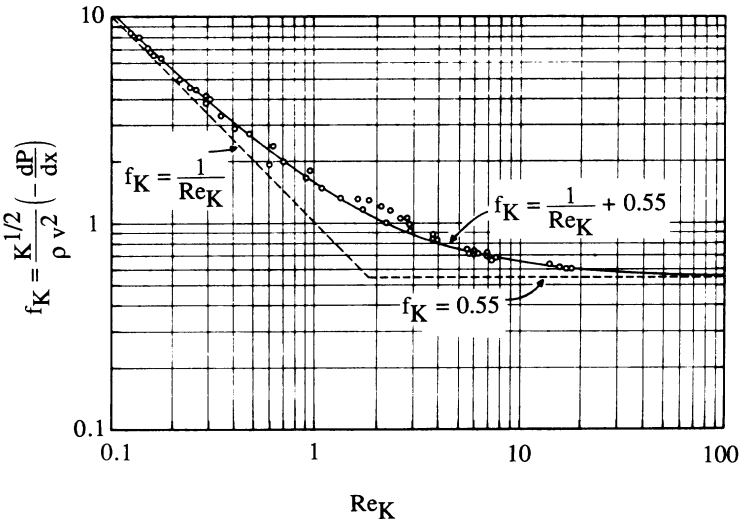

Figure 4.1: Influence of inertial body forces on flow through porous media given by the Forchheimer extension of Darcy's Law.[31]

It should be noted that this transition defined by Forchheimer equation does not correspond to the traditional distinction between laminar and turbulent flow. For $Re_K > 0.1$, the form drag becomes significant even though the flow remains laminar. Truly turbulent flow has been found not to occur until $Re_K \sim 100$ and this is rarely encountered in flow of incompressible fluid through porous media.[33] Maximum fluid velocities occur at the beginning of an infiltration and the corresponding Re_K is typically well below 0.1 for oil infiltrations. For liquid metal infiltrations into large powder, the Re_K can approach or exceed unity briefly at the start of infiltration, but usually falls to below 0.1 before the height reaches 1 cm.

4.2.2 Liquid flow model

Based on the typical conditions for capillary driven flow of oil or liquid metal into powder with diameter less than ~500 microns, characterization by Darcy's Law is sufficient. For the case of liquid flowing vertically into a sintered skeleton of porous media, it can be rewritten as a differential equation.

$$\frac{\Delta P}{h} = \frac{\mu}{K}\left(\varepsilon \frac{dh}{dt}\right) \tag{4.7}$$

Substitution of the capillary pressure and gravitational head loss yields:

$$\frac{dh}{dt} = \frac{K}{\varepsilon\mu h}\left(\frac{6\gamma'(1-\varepsilon)}{D\varepsilon} - \rho g h\right) \tag{4.8}$$

where $\gamma' = \gamma_{LV}\cos(\theta)$. This differential equation can serve as a model to predict the flow rate of liquid into various geometry skeletons.[34] By substituting $A \equiv \frac{6\gamma'(1-\varepsilon)K}{D\varepsilon^2\mu}$ and $B \equiv -\frac{K\rho g}{\varepsilon\mu}$, the above equation can be simplified for integration in the following form:

$$\int_0^h \frac{h}{A+Bh}dh = \int_0^t dt \tag{4.9}$$

After integration, the time must be determined as a function of infiltration height due to the implicit nature of the equation.

$$\frac{h}{B} - \frac{A}{B^2}\ln\left(\frac{A+Bh}{A}\right) = t \tag{4.10}$$

Although making time a dependent variable may seem a bit counterintuitive, the flow model can now easily be compared with subsequent experimental results.

4.2.3 Permeability prediction based on pore geometry

It is very useful to be able to predict the permeability of porous media based on known geometric properties. One method for doing this is the model developed by Kozeny based on solution of the Navier–Stokes equation for known porous media geometry, a bed of uniform diameter spheres. The original model was further modified by Carman after comparison with experimental work. For a skeleton with void fraction ε and specific surface area per unit volume of solid *S*, the permeability *K* can be predicted by the Kozeny–Carman equation.[35]

$$K_{K-C} = \frac{\varepsilon^3}{5S^2T(1-\varepsilon)^2} = \frac{D^2\varepsilon^3}{180T(1-\varepsilon)^2} \tag{4.11}$$

As discussed earlier in the section on capillary pressure, the specific surface area S is equal to $6/D$ for the case of uniform diameter spheres. The Kozeny–Carman equation has been exposed to some criticism due to variability under different experimental conditions, but remains the most widely recognized and useful means of predicting permeability for porous media. Prior researchers have included a 'tortuosity' factor T in the denominator to correct for differences between predicted permeability and that measured experimentally. This is typically justified by suggesting the actual path flow path is T times longer than the 'apparent' straight path.[35]

4.3 Infiltration model incorporating freezing

As mentioned previously, solidification of the infiltrant while it is still flowing into the skeleton results in a choking effect on the flow. Each powder particle essentially grows radially at the solidification rate determined by diffusion. As the powder particles impinge and the volume fraction of solid increases, the permeability of the skeleton decreases, provides greater restriction to flow, and will eventually cuts off the flow completely. This occurs first in at the entry point of the liquid, where the liquid and solid have been in contact with each other the longest, subsequently preventing liquid from flowing in all downstream sections. The maximum distance the liquid can travel due to this freezing is referred to as the infiltration or penetration distance limit. Note that it is a maximum distance from the entry point of the liquid, and not a direct height limit as with capillarity.

4.3.1 Growth of a sphere within a unit cell

With the goal of estimating the permeability of a skeleton as a function of its degree of solidification, the volume fraction and surface area to volume ratio were calculated for a powder bed with a simple cubic lattice structure. The unit cell of this geometry can be modeled as a sphere sitting inside a cube with side length equal to the sphere diameter. The solidification of the skeleton corresponds to growth of the sphere, with the lattice constant, represented by the cube side length, remaining constant. As the sphere grows, it takes up a larger fraction of the cubes interior volume as illustrated in Figure 4.2.

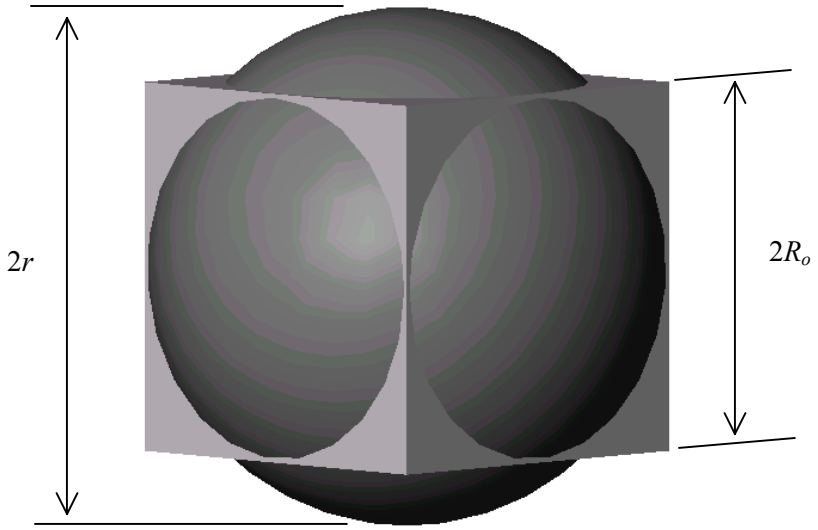

Figure 4.2: Growth of sphere of radius *r* within cubic unit cell with side length equal to the initial sphere diameter, $2R_o$.

The initial volume fraction of this unit cell is $\frac{4}{3}\pi R_o^3/(2R_o)^3$ or 52.4%, where R_o is the initial sphere radius and $2R_o$ is the cube side length. Once the radius of the sphere reaches $\sqrt{3}R_o$, the sphere will completely enclose the initial cube, corresponding to unity volume fraction and zero surface area (and adjacent spheres would be overlapping). For the range $R_o \le r \le \sqrt{2}R_o$ where r is the growing sphere radius, the volume fraction and surface area can be calculated simply by subtracting the elements of the spherical caps that would extend outside the cube. The volume of each cap corresponds to where particles would impinge upon each other in the cubic-latticed skeleton. The volume of each cap can be found by integrating the solid of revolution[36]:

$$V_{cap} = \int_{R_o}^{r} \pi \cdot (r^2 - x^2)dx = \pi r^2 (r - R_o) - \frac{\pi}{3}(r^3 - R_o^3) \tag{4.12}$$

The volume fraction can then be calculated as:

$$v_f = \left(\frac{4}{3}\pi r^3 - 6\pi r^2 (r - R_o) + 2\pi (r^3 - R_o^3)\right) \Big/ (2R_o)^3 \tag{4.13}$$

Similarly, the surface area of each cap can be found by integrating the area of the surface of revolution:

$$S_{cap} = \int_{R_o}^{r} 2\pi \cdot \sqrt{r^2 - x^2} \cdot \sqrt{1 + \left(\frac{x^2}{r^2 - x^2}\right)}dx = 2\pi r \cdot (r - R_o) \tag{4.14}$$

leading to a specific surface area of S, which is the ratio of surface area to solid volume:

$$S = \frac{4\pi r^2 - 12\pi r \cdot (r - R_o)}{v_f \cdot (2R_o)^3} \tag{4.15}$$

4.3.2 Change in permeability

The results of equation 4.13 and 4.15 can be inserted into equation 4.11 to predict the change in permeability with growing sphere radius:

$$K(r) = \frac{\left(1 - \left(\frac{4}{3}\pi r^3 - 6\pi r^2 (r - R_o) + 2\pi \left(r^3 - R_o{}^3\right)\right)\right)^3}{5\left(4\pi r^2 - 12\pi r \cdot (r - R_o)\right)^2 (2R_o)^3} \tag{4.16}$$

As shown in Figure 4.3, the permeability decreases sharply with radius so the limited model range of $r < 1.4R_o$ is sufficient. It should be noted that application of the Kozeny–Carman model in this context is only valid when the geometry still resembles packed spheres. This geometry exists for the initial packing of the spheres, $K(R_o)$, and prediction of the initial slope when $r \approx R_o$, but the model validity becomes questionable as solidification progresses. Nonetheless, it provides a reasonable estimate of how the permeability will vary during solidification.

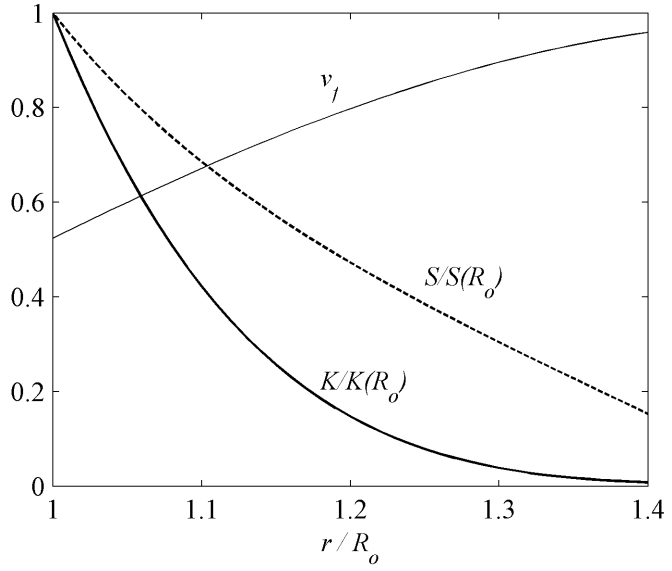

Figure 4.3: Volume fraction v_f, normalized surface area to volume ratio S, and normalized permeability K as a function of sphere growth (solidification) in a simple cubic unit cell.

The geometry of a randomly packed powder bed will differ from that of a simple cubic lattice and cause some deviation from the curves above. In particular, the void fraction ε will differ from

that of the initial unit cell, which is 47.6%. The void fraction (1-v_f) must be scaled appropriately by $\varepsilon/_{47.6\%}$ to achieve a better estimate of *K(r)* for a given powder skeleton. Finally, the permeability as a function of time is found based on the growth of the sphere radius $r(t) = R_o + X(t)$. As discussed in Chapters 2 and 3, the solidification rate is well represented by:

$$X(t) = \beta\sqrt{4\tilde{D}t} \tag{4.17}$$

where β is determined from the solidus and liquidus compositions or experiments, $\tilde{D}$ is the diffusivity of the melting point depressant in the solid and *t* is time.

The resulting permeability dependence on time is shown in Figure 4.4 for two skeletons with different void fractions, 100 μm diameter powder, and sample solidification parameters denoted in the caption. *K(t)* is the result of equation 4.16 with substitution of *r(t)* based on equation 4.17 and v_f modified based on ε as suggested above.

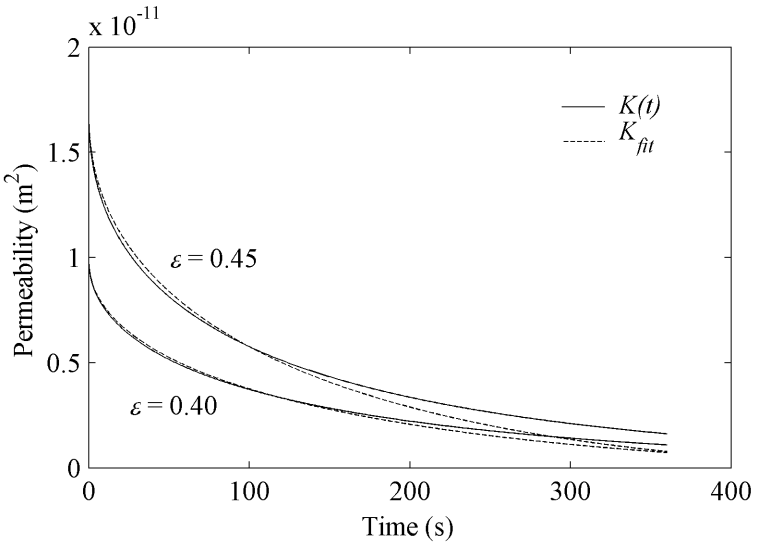

Figure 4.4: Predictions of *K(t)* during skeleton solidification (*D*=100 μm, β=1, $\tilde{D}$ =10^{-13} m^2/s) and curve fits of equation 4.18 estimating permeability change.

For reasons that will become more apparent during the data analysis presented in sections 5.6 and 5.7, it is useful to have a simpler equation relating the permeability and time as follows:

$$K_{fit} = K_{K-C}\left(1-(1+5\varepsilon)\frac{X(t)}{D/2}\right)^2 \tag{4.18}$$

This estimate matches the curve well until the permeability decays to below 20% of its initial value, at which point the corresponding flow rate is very small and the difference is tolerable. The general form of equation 4.18 was selected based on matching a quadratic curve to the permeability decay of Figure 4.3. The parameter (1+5ε) was determined using a least-squares fit weighted by the permeability to force a closer match when the permeability is greater and has more influence on liquid flow. The dependence on void fraction was found by matching the curve for various initial void fraction values, as shown in Figure 4.4. The permeability at t=0 is fixed at the permeability predicted by the Kozeny–Carman equation and would typically include a tortuosity factor determined from experiments, although for the data shown in Figure 4.4, T was set to unity.

4.3.3 Numerical simulation of infiltration rate with variable permeability

The infiltration rate into a powder skeleton during solidification can be predicted using the changing permeability in equations 4.16 or 4.18 in the flow model described in equation 4.8. A numerical simulation was written using MATLAB, with the code provided in Appendix B. A simple version initially assumes that permeability changes with time only, and is the same everywhere in the skeleton at a given moment. Then a modification is described which accounts for spatial differences in a skeleton's permeability due to variable contact time with the infiltrant.

Because the infiltration rate and the permeability change very quickly at the beginning of the simulation and then begin to level off, a variable time step was used. Small time steps are necessary for simulation accuracy, but lead to excessively long computing time when used for the entire simulation. The variable time steps provide greater simulation accuracy for a given number of computer iterations. Starting with an initial time step of Δt, each successive time step increased by Δt, such that the time vector consists of the following components, where n is the number of iterations in the finite-difference simulation:

$$t(1:n) = \begin{bmatrix} 0 \\ 0+\Delta t \\ 0+\Delta t+2\Delta t \\ \dots \\ 0+\Delta t+2\Delta t+3\Delta t+\dots+(n-1)\Delta t \end{bmatrix} = \begin{bmatrix} 0 \\ \Delta t \\ 3\Delta t \\ \dots \\ (n^2-n)\Delta t/2 \end{bmatrix} \tag{4.19}$$

Since the infiltrant flow stops when the skeleton permeability reaches zero, the solidification rate can be used to determine the necessary run length based on how quickly the permeability goes to

zero for the growing particle radius shown in Figure 4.3. The infiltration effectively comes to a halt when $r = 1.3R_o$ or $X(t) = 0.15D$. The necessary runtime $t(n)$ can be plugged into the solidification rate to find the time at which this occurs. The corresponding initial time step, Δt can be found from the bottom line of equation 4.19.

$$t(n) = \left(\frac{0.15D}{\beta}\right)^2 \Big/ 4\tilde{D} \qquad \text{and} \qquad \Delta t = \frac{2 \cdot t(n)}{\left(n^2 - n\right)} \tag{4.20}$$

At each time step i from 1:n, the height increase is calculated using the numerical difference form of equation 4.8:

$$h(i+1) = h(i) + i\Delta t \frac{\left(\frac{6\gamma'(1-\varepsilon)}{D\varepsilon} - \rho g \cdot h(i)\right)}{\varepsilon\mu \cdot R(i)} \tag{4.21}$$

where $R(i)$ is a resistance term equal to $h(i)/K(i)$ for the case when permeability varies with time only. For convenience, the time steps described in equation 4.19 are used to define $K(t)$ and for calculating $h(t)$, but they need not be the same.

To initiate the finite-difference simulation, it's necessary to estimate the first value for the height $h(2)$ in order to avoid dividing by $h(1) = 0$ during the first iteration through the simulation. To provide a reasonable estimate of the height after the first time step, this first value is selected such that $h(3)$ would equal twice $h(2)$. Using i=2 in the right-hand side of equation 4.21 and setting the left-hand side to equal 2 times $h(2)$ gives:

$$h(2) = \sqrt{\frac{2\Delta t \cdot K}{\varepsilon\mu}\left(\frac{6\gamma'(1-\varepsilon)}{D\varepsilon}\right)} \tag{4.22}$$

The numerical simulation can be checked against the analytical solution of equation 4.10 by setting $R(i) = h(i)/K(t=0)$. A small error develops at the beginning of the numerical simulation, but for n=500 and typical conditions, this error is less than 1 mm.

To account for spatial variations in permeability, the bulk resistance is the sum of the local resistance in each height segment. The skeleton permeability is known as a function of the elapsed time it has been in contact with the liquid infiltrant, so this time must be determined for each height segment to determine the localized permeability. In an example of an infiltration height vs. time curve, Figure 4.5 defines the time in contact with liquid for a given point as $t'(i,j)$

where *i* is the index for the current total infiltration time, and *j* is an index from 2:*i* for each of the previous time steps and the corresponding heights. This is a convenient method of breaking down the skeleton into height segments that have undergone variable degrees of solidification.

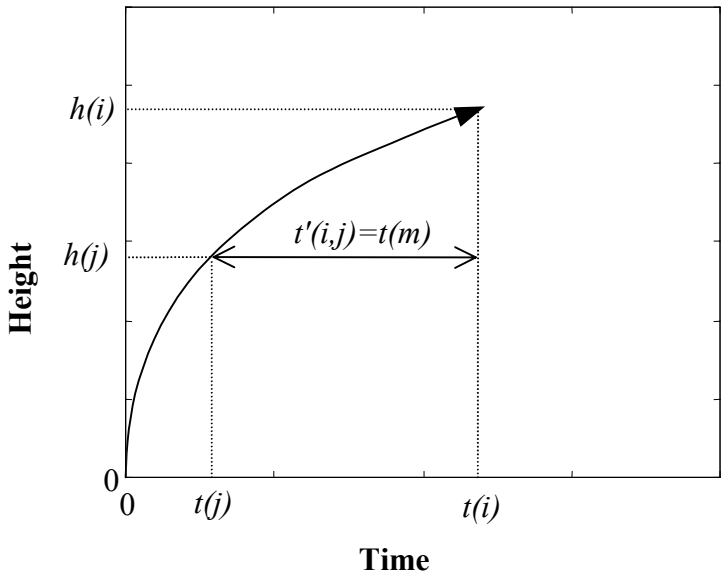

Figure 4.5: Definition of terms for variable permeability within a skeleton.

The actual time in contact with liquid, *t'*, is equal to *t(i) – t(j)* but due to the non-linearity between the indices and elapsed time, the new index *m* cannot be found simply by subtracting *i – j*. Such an index is convenient to reference the existing function of *K(t)* because K(t) has been defined by the same variable time steps of equation 4.19. The new index can be found based on the relation of time to the indices in equation 4.19.

$$t(m) = \left(m^2 - m\right)\frac{\Delta t}{2} = \left(i^2 - i\right)\frac{\Delta t}{2} - \left(j^2 - j\right)\frac{\Delta t}{2} \tag{4.23}$$

The quadratic relation can be solved directly for *m*, and then rounded to the nearest whole number for use as an index to define the localized permeability.

$$m(i,j) = \text{round}\left(\frac{1+\sqrt{1+4\cdot\left(i^2 - i - j^2 + j\right)}}{2}\right) \tag{4.24}$$

The resistance term in equation 4.21 accounts for the spatial as well as temporal change in permeability when defined as a sum of series resistances from each height segment:

$$R(i) = \sum_{j=2}^{i}\left(\frac{h(j) - h(j-1)}{K(m)}\right) \tag{4.25}$$

with *m* as a function of *j* from equation 4.24.

The actual difference in both height and effective permeability between the numerical simulations using *K(t)* and *K(h,t)* is fairly small. The *K(t)* simulation predicts a 'worst case' and a final infiltration height that is ~10% less than for *K(h,t)*. The results of the numerical simulation are shown in Figure 4.6 for transient liquid-phase infiltration of a 100 μm powder skeleton with ε=0.4, the same solidification parameters as in Figure 4.4, and infiltrant properties of ρ=7.2 g/cc, μ=10.5 mPa-s, and γ′=1.4 N/m.

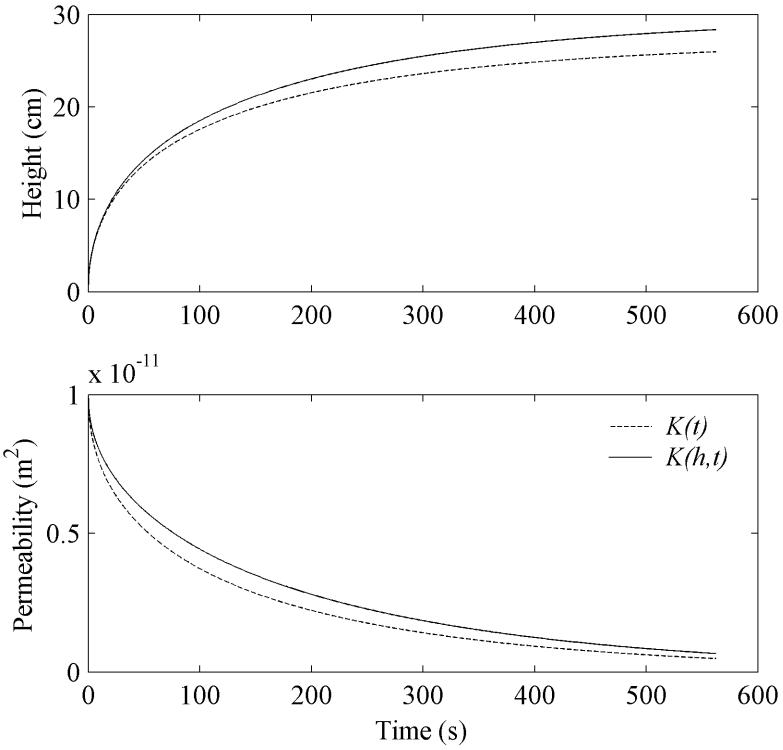

Figure 4.6: Sample results of TLI numerical simulation and effect of including spatial change in permeability.

Chapter 5: Infiltration Rate Results and Analysis

5.1 Oil permeametry

Direct measurement of permeability is relatively simple and can be done at room temperature with any fluid of known physical properties.[37] Permeametry experiments were conducted using Multitherm 503, a heat-transfer oil with the physical properties described in Appendix C. Figure 5.1 shows a schematic representation of the apparatus used for measuring permeability alongside a photograph of the experimental setup.

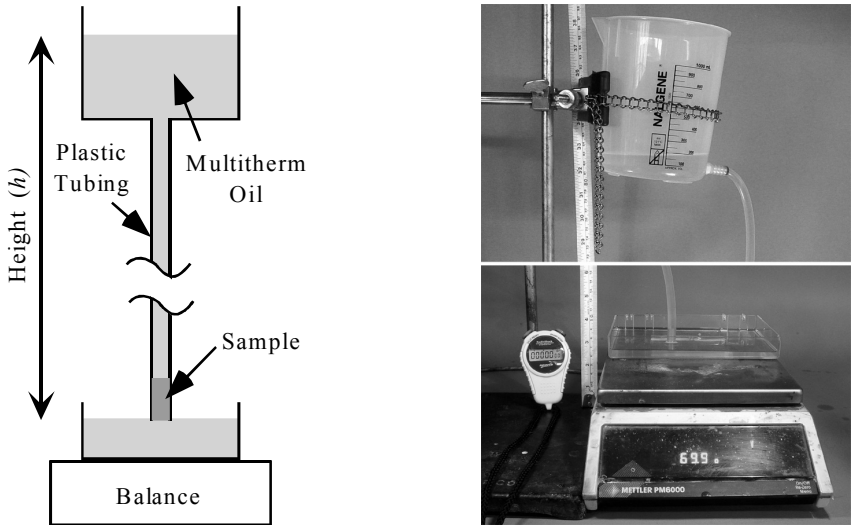

Figure 5.1: Permeametry using oil flow through cylindrical plug sample.

The plastic tubing used was ¼″ inner diameter and samples had a slightly larger diameter so the tubing stretched around it and ensured all the liquid flowed through the sample, not around it. The top and bottom liquid reservoirs had a large cross-sectional area of ~100 cm^2 to minimize the height change during an experiment. Samples were typically 15 – 20 mm in length and prepared as described below in Appendix D. The mass flow through the sample was determined via timed measurements of mass increase to the lower reservoir. The permeability is calculated directly from Darcy's Law:

$$K = \frac{\dot{m}}{\rho A} \Big/ \frac{\rho g h}{\mu L} \tag{5.1}$$

where ρ is the fluid density, g is gravity, h is the height difference of the reservoirs, μ is the fluid viscosity, L and A are the length and cross-sectional area of the sample, and $\dot{m}$ is the mass flow

rate of the liquid. For better measurement accuracy, several flow-rate measurements are taken at varying heights and the permeability is determined from the least squares fit to the corresponding plot slope. The tortuosity factor *T* for a given powder sample is then determined by solving for T in equation 4.11 using the average powder diameter and the measured permeability value.

D_{powder} (μm)	D_{sample} (mm)	L_{sample} (mm)	1−ε	$K_{measured}$ (m^2)	Tortuosity
63–74	9.48	19.35	59.0%	3.54E-12	1.45
90–104	9.42	16.56	59.6%	5.50E-12	1.76
125–150	6.29	14.90	58.0%	8.79E-12	2.64
212–250	6.34	19.20	56.4%	2.80E-11	2.76
250–300	7.05	18.93	54.2%	6.79E-11	2.02

Table 5.1: Permeametry using Multitherm 503 oil and skeletons of nickel powder.

The powder was sieved into narrow size distributions to match the assumption of uniform diameter spheres used in the Kozeny–Carman model. The distribution of powder size within the range is unknown for each powder sample, which would cause the weighted average diameter to differ from the midpoint of the sieve sizes. In addition, the surface texture of the hydrometallurgically processed nickel powder was cauliflower-like and the roughness will have an affect on the permeability. This combination of factors is taken into account with the tortuosity factor, which appears to have a correlation with powder size but there is no strong justification for this. The sample of largest powder was made by machining a sintered bar with square cross-section into a cylindrical plug. The corresponding rough surface introduced more uncertainty into the calculation of void fraction and could explain the deviation from the trend. All of the other cylindrical samples were sintered inside an alumina tube and had smoother exterior surfaces.

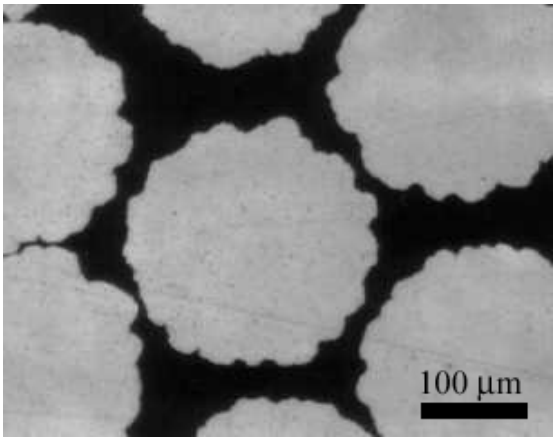

Figure 5.2: Ni powder made by the hydrometallurgical process. Polished cross-section of several powder particles embedded in epoxy highlights their surface roughness.

5.2 Oil infiltration and comparison with flow model

The infiltration rate of oil into various skeletons was measured and compared with the flow model developed based on Darcy's Law. For nickel powder, the infiltration front is easily distinguishable due to the darkening of the skeleton when filled with oil. A sintered skeleton was held vertically next to a ruler as shown in Figure 5.3, and infiltration height was measured as a function of time.

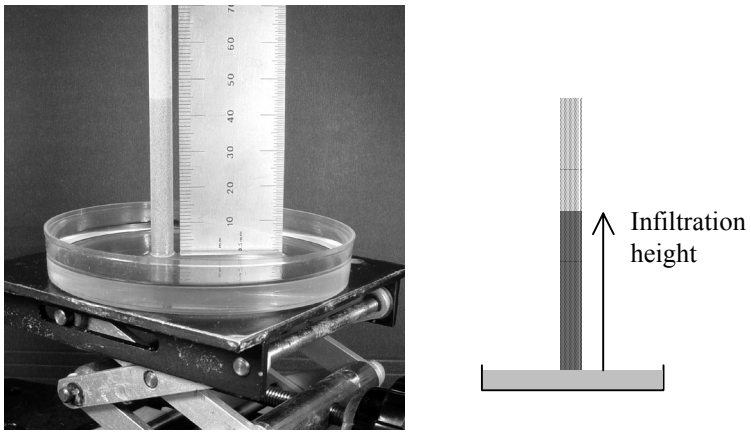

Figure 5.3: Photo and schematic of infiltration rate measurement of Multitherm oil into 125–150 µm nickel skeleton.

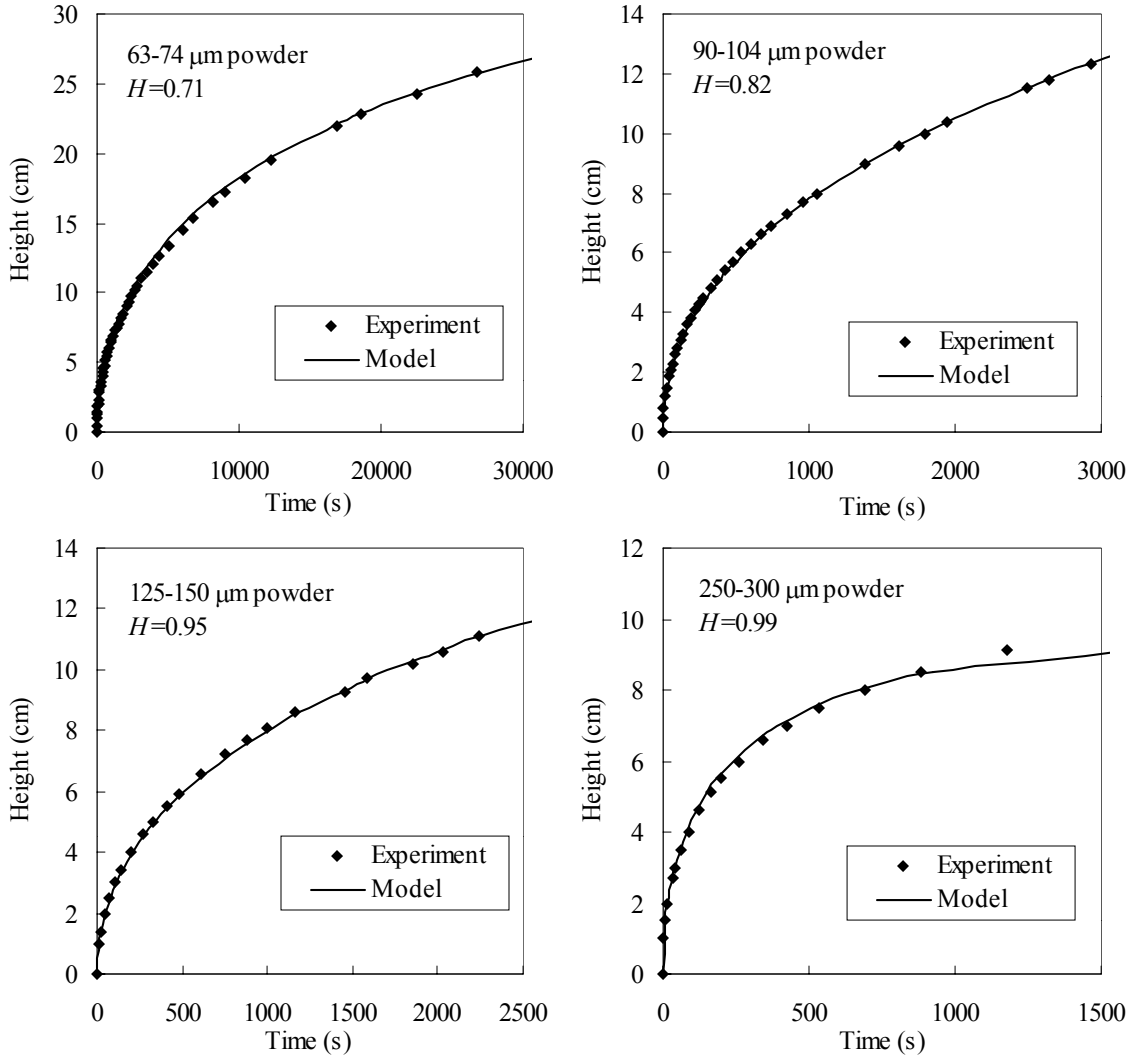

Figure 5.4: Infiltration rate of oil into nickel powder and corresponding rate model.

The experimental results shown in Figure 5.4 correspond to the solution to equation 4.8 with the addition of a parameter, *H*, that accounts for variation of the actual capillary pressure from that predicted by equation 4.3:

$$\frac{dh}{dt} = \frac{K}{\varepsilon\mu h}\left(H\frac{6\gamma'(1-\varepsilon)}{D\varepsilon} - \rho g h \right) \tag{5.2}$$

The values for permeability are calculated from equation 4.11 using the tortuosity factors determined from oil permeametry and listed in Table 5.1. The parameter *H* could ideally be extracted from the final capillary rise height, but a secondary flow regime is observed over longer time scales where incessant fingering of the liquid front prevents measurement of the equilibrium

rise height. Instead, the values for H are selected to match the experimental height measurements with minimum least-squares error. The values for H are shown on the plot corresponding to each powder size. For both H and T, the given values are considered representative of the given powder size range and used for future modeling results with liquid metal infiltrant.

5.3 Fluid properties of liquid metal

The fluid properties of density, surface tension, and viscosity must be determined in order to apply the liquid flow model to another infiltrant. For the case of liquid copper, these properties are fairly well defined, but the properties of the binary nickel–silicon alloy used as an infiltrant are not available in literature. The near-eutectic composition Ni–Si material is not commercially available, so it was mixed from high purity Ni chunks and Si chips, both obtained from Alfa Aesar (stock #'s 35482 and 38542), using an induction furnace in MIT's foundry under a blanketed Argon atmosphere. The methods used to determine each of the fluid properties for this material are given below.

5.3.1 Density

The density of the solid Ni – 10.2 wt% Si was measured using Archimedes principle with several different cast samples and found to be 8.08 g/cc. Cross-sections of the samples revealed no significant voids that would alter the density measurement. To estimate the density of the same material at its melting point, the ratio of liquid density to solid density at room temperature was compared for several different common metals as compiled in Appendix E. The ratio was fairly consistent for the common metals listed (excluding the semiconductor Si) and this ratio was applied to the Ni–Si alloy to get an estimated liquid density of 7.2 g/cc. Theoretical approximation of density for a binary liquid alloy is given by the weighted sum of their atomic volumes:

$$\rho_{alloy} = \left(x_1 M_1 + x_2 M_2\right) \Big/ \left(\frac{x_1 M_1}{\rho_1} + \frac{x_2 M_2}{\rho_2} \right) \tag{5.3}$$

where x_i, M_i, and ρ_i are the atomic fraction, molecular weight, and liquid density of the two mixture components, resulting in a density of 6.5 g/cc for the Ni–Si alloy.[39] However, significant negative excess volumes have been reported for compound-forming alloys that would result in underestimating the density by as much as 25%. Because of this uncertainty, the initially estimated value of 7.2 g/cc was used for subsequent calculations.

5.3.2 Surface tension

The surface tension of pure nickel at its melting temperature of 1454°C is listed in Appendix E as 1.778 N/m. The addition of alloying elements generally tends to reduce the surface tension of pure metals. To determine the surface tension of the Ni–Si infiltrant, a method based on the Wilhelmi plate principle[38] was developed for use with liquid metal inside the furnace. In this case, a 1mm thick, 5 cm wide sheet of pure nickel was dipped into a pool of liquid infiltrant. It was suspended from a wire that could be raised and lowered from outside the furnace while measuring the wire tension using a load cell. The setup was the same as that used for measuring the infiltration rate of liquid metal and is described in more detail in section 5.4. Figure 5.5 plots the surface tension force generated from four sequential measurements. For each measurement, the sheet was lowered until it touched the surface of the melt, then held for 5–10 seconds and removed. The average value was 1.4 N/m.

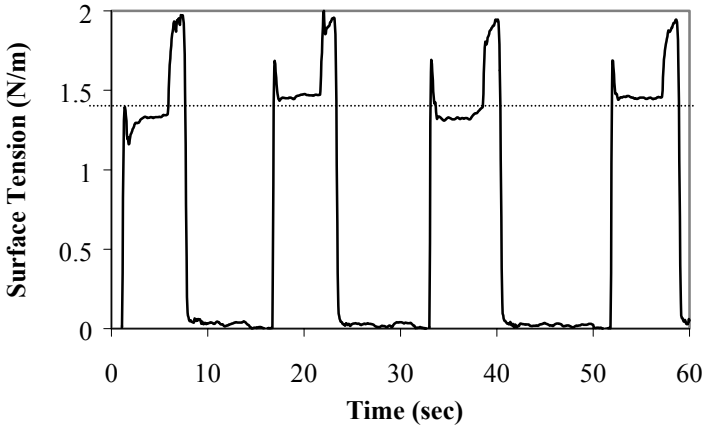

Figure 5.5: Surface tension measurements from dipping nickel plate into Ni – 10.2 wt% Si at 1200°C.

5.3.3 Viscosity

Measurements of the viscosity of pure nickel at its melting temperature are fairly consistent at ~5 mPa-s and the viscosity decreases by ~0.005 mPa-s/°C as temperature increases.[39] The effect of alloying elements on viscosity is somewhat unpredictable, so a relatively simple method for measuring the infiltrant viscosity was developed based on the capillary method. A known quantity of liquid metal is forced through a capillary tube by a known pressure differential using the apparatus described in Appendix F. The viscosity is determined by the flow rate through the 23 cm long alumina tube with 0.75 mm inner diameter. Because any solidification of the infiltrant would clog the capillary tube, the experiments were conducted using the eutectic

composition of Ni – 11.3 wt% Si at a temperature of 1200°C, significantly above the eutectic temperature of 1143°C. The viscosity was measured at 10.5 mPa-s, with an estimated accuracy of +/- 10%.

5.3.4 Summary

The liquid properties of various infiltrants are summarized in Table 5.2, along with the typical infiltration temperature. Any change in fluid properties between the measurement temperature and infiltration temperature is neglected. The maximum capillary height for a given powder skeleton is proportional to γ'/ρ, which is 4–5 times greater for liquid metal than for oil. Significantly below the capillary rise limit, the rate of infiltration is affected only by γ' and μ, therefore infiltration occurs significantly faster with liquid metal because the driving force of surface tension is ~50 times greater and there is very little difference in the viscous drag. The corresponding higher flow rates can cause the form drag term of equation 4.5 to potentially become significant. The critical Re_K of 0.1 corresponds to a maximum front velocity of 1.5 cm/s for Cu or 4.5 cm/s for Ni–Si in a skeleton of 250–300 μm powder. Infiltrant velocities sometimes exceed these values, particularly for copper, but only briefly at the beginning of an infiltration. Since the velocity and permeability drop off sharply with time during an infiltration, the overall contribution of the form drag term to predicting infiltration rate and penetration distance is considered insignificant.

Fluid	**Multitherm 503 Oil 20 °C**	**Ni – 10.2 wt% Si 1185 °C**	**Copper 1100 °C**
ρ [kg/m^3]	794	7200	8000
μ [mPa·s]	8.0	10.5	4.0
γ' [N/m]	0.029	1.4	1.2

Table 5.2: Fluid properties of oil and liquid metal infiltrants.

5.4 Experimental setup for measuring liquid metal infiltration rate

Measurement of the imbibition or infiltration rate of liquid metal into a powder skeleton is challenging because it cannot be easily observed optically. Furnace windows can be installed to provide limited views of the hot zone, but the walls of the infiltrant crucible would further obstruct the view. In addition, the contrast at the infiltration front may not be easy to distinguish, depending on the relative emissivities of the liquid and solid material. An alternative method was developed to measure the infiltration rate indirectly through the increase in the skeleton's mass as

it sucks up the liquid infiltrant. The skeleton is suspended from a wire passing through the roof of the furnace and the wire tension is measured using a load cell. The mass of the skeleton must be isolated from other forces acting on the skeleton and wire, specifically friction, surface tension, and buoyancy.

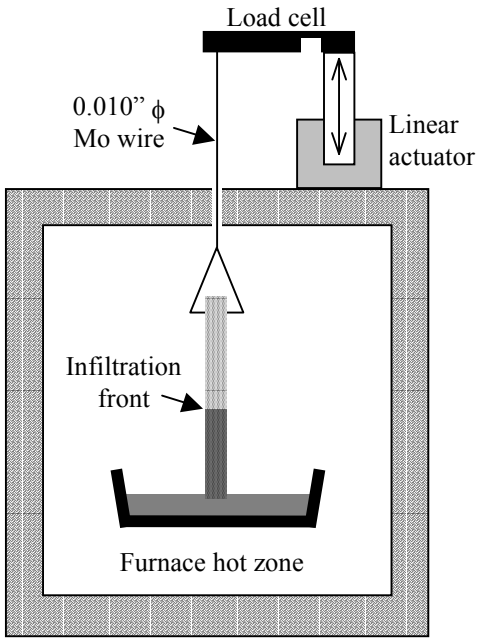

Figure 5.6: Setup used to measure infiltration rate inside furnace through mass increase.

The force measurement device (in this case a 1 N load cell from Strain Measurement Devices) must be kept outside the hot zone, therefore the supporting wire must pass through the gas-tight furnace shell with little or no friction. A short ~2 cm section of alumina thermocouple tube (⅛″ OD, double bores of 0.023″ ID) is mounted in a compression fitting using Teflon ferrules with the holes remaining open for the wires to pass through. The holes must be kept small and long enough to prevent contamination of the furnace atmosphere, which is kept at a slight positive pressure to prevent influx of air. Molybdenum wire, 0.010″ ϕ, was selected because it maintains strength at high temperatures and is reasonably ductile before firing. The wire is stretched prior to installation to straighten it and prevent it from rubbing against the ceramic tube. Hysteresis between raising and lowering a skeleton of fixed mass reveals the contribution of friction to the wire tension to be typically less than 0.5 grams.

The force acting on the skeleton due to surface tension can be estimated from the solid/liquid surface energy and the perimeter of the skeleton. The ratio of the skeleton perimeter to its cross-sectional area will determine the relative importance of the effect of surface tension. This ratio was kept small by using skeletons with cylindrical or square cross-sections and diameter or side lengths of ~1 cm. Typically the compensation for the effect of surface tension corresponds to 1–2 centimeters of infiltrant height rise.

The buoyancy force acting on the skeleton is equal to the volume of liquid displaced times the difference in density. Since the liquid displaced by solid has only a small density difference, the corresponding buoyancy force is negligible, but the force due to liquid displaced by void space in the skeleton can be significant. The overall effect of the buoyancy, when translated to an infiltration height, is roughly equal to the distance the skeleton is submerged below the surface of the melt. To keep the skeleton near the melt surface, it is slowly lowered from above the melt with a linear actuator while monitoring the wire tension. A noticeable step increase in wire tension (due to surface tension) occurs when the skeleton touches the surface of the melt, and the actuator is then stopped so the buoyancy effect is limited to a few millimeters.

Force disturbances can also occur if the skeleton touches any other solid objects. The melt pool must be kept deep enough to prevent the skeleton from accidentally touching the bottom of the crucible. In the case when the infiltrant is maintained at a semisolid state, even a sparse matrix of solid dendrites can support some of the skeleton's mass and disrupt the measurements. A stirring mechanism originally developed to ensure uniform composition in the melt also serves the purpose of breaking up any solid matrix that forms in the crucible. A ceramic rod with a rectangular block of bisque-fired alumina cemented on the end was used as a propeller to stir the melt at ~100 rpm while it was slowly cooled from a fully liquid state to the desired infiltration temperature. After the infiltration temperature is reached, the propeller is lifted so it only stirs in the top half of the melt, with the intention of the solid settling to the bottom. The propeller is stopped and removed prior to dipping the skeleton. After removal of the skeleton, dendrites can sometimes be found attached to the skeleton where it was dipped into the melt, visible in Figure 3.9. These likely are responsible for some of the disturbances in the infiltration rate data, but useful results were still attainable.

The infiltration height of the skeleton can then be found based on mass increase as the the liquid fills the skeleton:

$$h = \frac{m}{\rho_l \varepsilon A} = \frac{cV - \gamma' L / g}{\rho_l \varepsilon A} \tag{5.4}$$

where m is the mass, ρ_l is the liquid density, ε is the void fraction and A is the cross-sectional area of the skeleton. The mass is determined from the load cell voltage V based on the load cell constant c (g/V) and the surface tension effects as discussed above where L is the perimeter of the skeleton. In most cases there was no buoyancy effect, but because it is proportional to height it can be compensated for after the conversion from mass to distance. A data-logging multimeter was used to record measurements from the load cell through a 1000x DC amplifier at time intervals of 0.05 seconds. The load cell was first calibrated at room temperature with several different masses and c was found to equal 11.2 g/V. Because the load cell is close to the furnace roof and is near 100°C during infiltration measurements, the difference between the skeleton's mass and the infiltrated part's mass was used to calibrate the load cell for each run at the elevated temperature. The mass change was divided by the difference between initial and final voltage measured from the load cell during each experiment, resulting in values of $c = 11.3 \pm 0.4$ g/V.

5.5 Dipping experiments to measure local permeability change

As discussed in section 4.3, the permeability of the skeleton begins to change as soon as it comes into contact with molten infiltrant and will therefore vary spatially within the skeleton during an infiltration. To experimentally isolate the local change in permeability, the skeleton was dipped in infiltrant for only a few seconds to fill the bottom few centimeters with infiltrant. The skeleton was then removed and held at temperature for a given time period as diffusional solidification occurs and the permeability decreases. The skeleton was then re-introduced to infiltrant to measure the corresponding change in permeability. As long as the initial dipping time is short, the skeleton can be assumed to be uniform, and the spatial variation in permeability can be ignored. The experiment is summarized in Figure 5.7 showing the sequence of actions in conjunction with the recorded data.

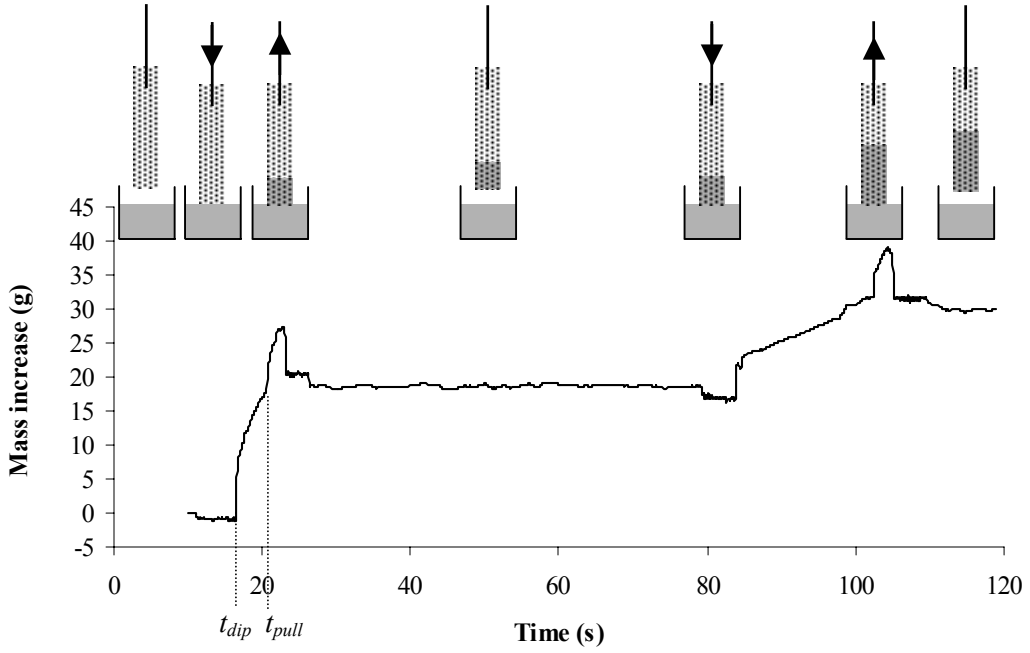

Figure 5.7: Raw data from dipping experiment to measure local permeability change. Increase in mass can be correlated to infiltration height. Raw data shown does not account for surface tension offset, which is only applied when the part is touching the melt.

The velocity of the infiltration front can be found by taking the derivative of the measured height vs. time. The experimental data is recorded 20 times per second, and allows a reasonable calculation of the slope for the short time periods over which the part is dipped. The permeability can be estimated from the front velocity and compared to the model shown in Figure 4.6. The permeability is calculated directly by rearrangement of equation 5.2:

$$K_{data} = \left(\frac{\varepsilon \mu h}{H \dfrac{6\gamma'(1-\varepsilon)}{D\varepsilon} - \rho g h} \right) \frac{dh}{dt} \tag{5.5}$$

where the slope dh/dt is calculated from a least squares fit to +/- N sequential data points over which the derivative is taken. Any irregularities in the height measurement become magnified in the calculation of permeability, so larger values for N help to smooth out the data. However, if the sample was dipped into the melt at t_{dip} and pulled from the melt at t_{pull}, then the slope calculations are only valid for $(t_{dip} - N/20) < t < (t_{pull} - N/20)$. Since the initial dip typically lasted for 3–4 seconds, N must be small to still extract permeability values for more than one second. Values of N ranged from 10–15 during initial dipping and from 50–80 after the hold. Figure 5.8 below shows the results of three dipping experiments with 250–300 μm powder and two experiments with 125–150 μm powder. The initial void fraction of each skeleton was slightly

different, which would result in a Kozeny–Carman permeability (including the appropriate tortuosity T for the powder size) unique to each skeleton. To allow a comparison of the skeletons, the plot shows a normalized permeability, which has been divided by $K_{K\text{-}C}$ for the given skeleton to compensate for differences in void fraction.

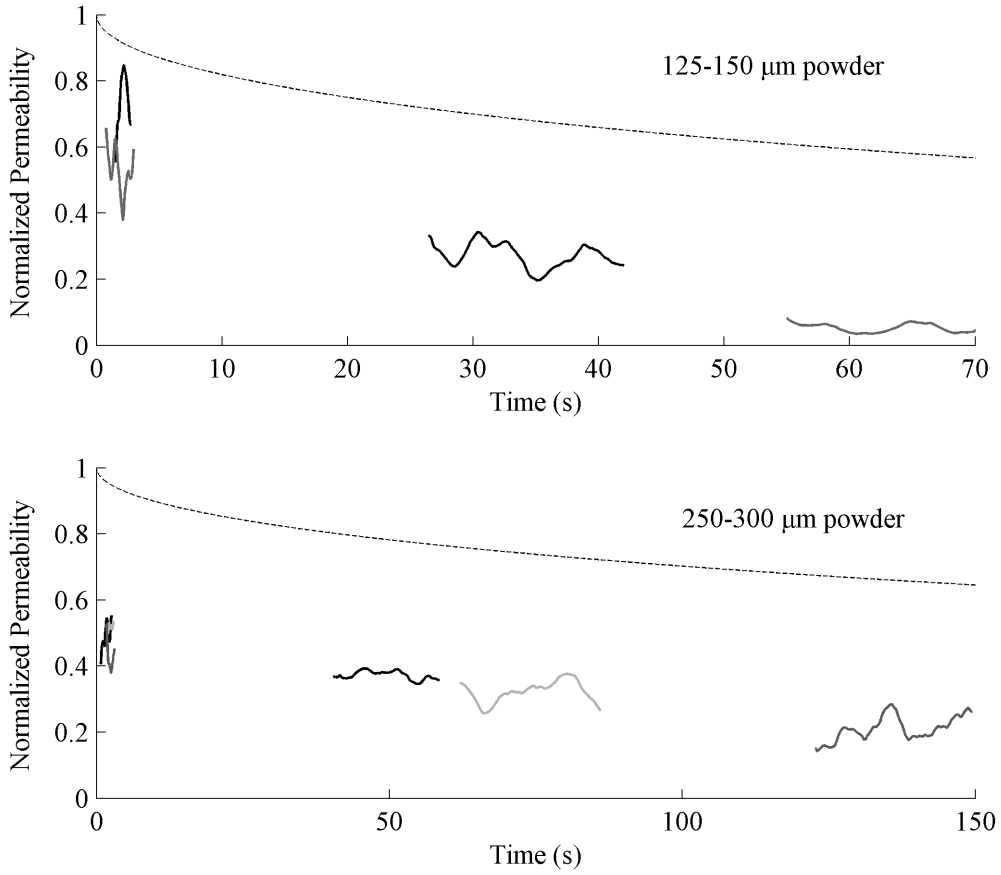

Figure 5.8: Local permeability change from dipping experiments for skeletons of two different powder size. The dashed line represents the *K(t)* model with β = 1.3 and $\widetilde{D}$ = 8.35 x 10^{-14} m^2/s. Solid black and gray lines are calculated using equation 5.5 and heights from dipping experiments.

The experimental results exhibited the expected decrease in permeability with time, and further show the rate of decay increases as the powder size decreases. However, when compared to the model of *K(t)* developed in section 4.3.2, the calculated permeability values are significantly lower than predicted (dashed line). The infiltration temperature was 1185°C, corresponding to the diffusivity given in the caption and the value for β was chosen based on the quenching experiments of section 3.2.2. The fluid properties used in the model are those listed in Table 5.2. The initial value of Re_K for the larger powder is 0.2 and it decreases rapidly, signifying that the

flow is indeed viscous dominated. The variables T and H used to fit the oil permeametry and infiltration rate experiments are intended to be representative of each skeleton's powder size range. Representing the permeability and capillary pressure variation from the given models for uniform diameter spheres, they can be considered skeleton parameters to be carried over for modeling with another fluid. Since T and H affect the fluid flow in the same manner as the fluid viscosity and the surface tension respectively, determination of these parameters is dependent upon the properties of the calibrating fluid. Similarly, the fluid properties of the Ni–Si infiltrant play a significant role in the calculation of permeability as shown in equation 5.5.

The lower than expected permeability value could be attributed either to an actual fluid viscosity greater than μ or an effective surface tension less than γ'. As discussed in section 5.3, the method used to determine viscosity necessitated measurement at a slightly higher temperature and silicon composition to prevent solid particles from clogging the capillary. The infiltrations of Figure 5.8 were done at 1185 °C with the bulk infiltrant composition in the two-phase field so that the extracted liquid was at its liquidus composition. The corresponding viscosity would be expected to be slightly higher than the estimated value of μ, although the specific relationship is unknown. An argument could also be made for an effective surface tension value less than γ', a static calculation from contact with a flat plate. The advancing contact angle is likely to be higher (resulting in lower γ') and could also be dependent upon the infiltration front velocity.

The dipping experiments were specifically designed to isolate the local permeability change in the skeleton for comparison with the model for $K(t)$. The differences between the two models for $K(t)$ and $K(h,t)$ shown in Figure 4.6 are quite small compared to the differences between experiment and model shown in Figure 5.8. A permeability calculation can be extracted from a simpler continuous infiltration experiment by neglecting the spatial differences in permeability.

5.6 Infiltration rate curves and analysis

Continuous infiltration rate experiments into nickel powder were conducted for four different size ranges with the Ni–Si infiltrant and three powder size ranges using pure copper as an infiltrant. For each experiment, the effective bulk permeability (ignoring spatial variation) was calculated using equation 5.5. For the infiltrations with Ni–Si at its liquidus composition, solidification in the melt pool is the likely cause of noise in the data. The slope dh/dt was averaged over a larger number of data points, N=200, to smooth out the measurements of permeability. The copper melt

pool at 1100°C did not cause as much disturbance in the height measurements so a smaller value of N=60 was used.

In order to extract physically meaningful information from the permeability data, the results of each experiment were fit to the form of equation 4.18 with the solidification rate substituted for $X(t)$ using the relation from equation 2.6:

$$K_{fit} = \frac{K_{K-C}}{\tau} \cdot \left(1 - \alpha(1+5\varepsilon)\frac{\beta\sqrt{4\tilde{D}t}}{D/2} \right)^2 \tag{5.6}$$

where the two parameters τ and α are fitted to the calculated permeability based on least squares. These parameters characterize the variation of the permeability curve from expectation in terms of a direct scaling factor accounting for initial variation, τ, and a coefficient influencing the rate of decay, α. Determination of τ and α cannot be done simultaneously because they appear in equation 5.6 in a non-linear manner. First, a free fit to a second-order polynomial fit is used to achieve a very good match to the curve and find the appropriate initial permeability at X=0. This involves solving for the independent parameters p_1, p_2, and p_3:

$$K_{K-C} \cdot \left(p_1 + p_2 \cdot (1+5\varepsilon)\frac{2X(t)}{D} + p_3 \cdot \left((1+5\varepsilon)\frac{2X(t)}{D} \right)^2 \right) = K_{data} \tag{5.7}$$

using linear regression to fit a curve to the calculations of equation 5.5 that extract permeability from experiments. The polynomial coefficients would be interdependent if this polynomial fit were forced to match equation 5.6, where the interdependence would relate to τ and α as follows:

$$p_1 = \frac{1}{\tau} \qquad p_2 = \frac{-2\alpha}{\tau} \qquad p_3 = \frac{\alpha^2}{\tau} \tag{5.8}$$

However, since p_2 and p_3 are determined independently, they rarely exhibit this interdependence and only the first parameter can be determined from the polynomial fit. The value for τ determined by the first fit can now be used to find the appropriate value for α by rearrangement of equation 5.6:

$$\alpha \cdot \left((1+5\varepsilon)\frac{2\beta\sqrt{4\tilde{D}t}}{D} \right) = \sqrt{1 - \tau\frac{K_{data}}{K_{K-C}}} \tag{5.9}$$

and finding the corresponding least square fit for α.

Figure 5.9 shows how the two equations fit the calculated permeability value using equation 5.6 with τ and α chosen from 5.7 – 5.9. The unadjusted model for the given skeleton, 125–150 μm

powder with 40.9% void fraction, uses the values for H=0.95 and T=2.64 determined with oil and solidification parameters β=1.3 and $\widetilde{D}$=8.35 x 10^{-14} m^2/s from the wire bundle experiments in Chapter 3. It significantly overestimates the permeability and therefore the corresponding height rise of the infiltrant. Both the original polynomial fit of equation 5.7 and the second curve fit to equation 5.6 match the measured permeability closely and therefore accurately predict the infiltration height for the given skeleton. The parameters τ and α can be used to characterize the observed behavior. Since α and β are both directly proportional to the solidification rate, the fitted value for α will depend on β. In order to facilitate application of the model to different material systems without the need for experimentally determining the solidification parameters, the theoretical value for β is calculated from the solidus and liquidus concentrations on the phase diagram.

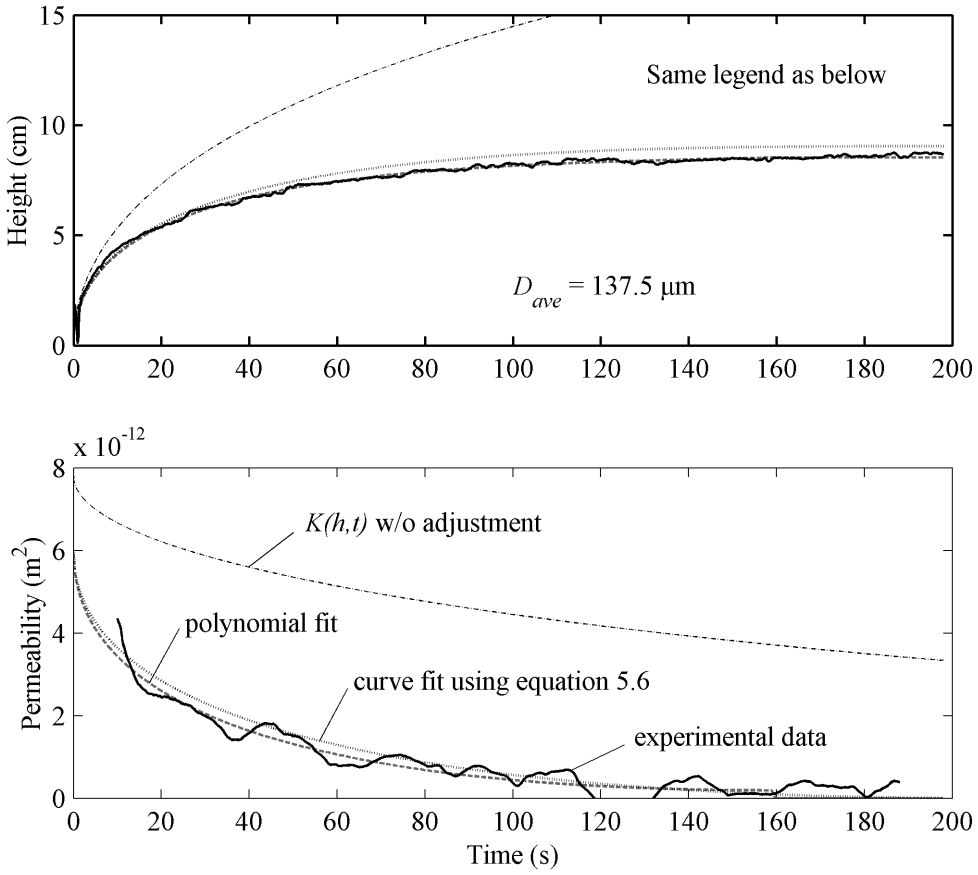

Figure 5.9: Continuous infiltration rate experiments, comparison with model and permeability curve fits (p_1 = 0.76, p_2 = –8.2, and p_3 = 22.5 for the polynomial fit; τ = 1.3 and α = 2.1 for the fit to equation 5.6).

The results of eight different experimental measurements of infiltration rate are summarized in Tables 5.3 and 5.4, where the variation from the model is captured in the curve-fitted parameters τ and α.

D_{powder} (μm)	ε	T	H	τ	α	$T \cdot \tau$	α (τ = 3.6/T)
63–74	40.3%	1.45	0.71	2.86	1.03	4.15	1.10
90–104	40.7%	1.76	0.82	1.83	1.65	3.22	1.61
125–150	40.9%	2.64	0.95	1.31	2.08	3.46	2.06
250–300	45.3%	2.02	0.99	1.62	1.53	3.27	1.18
250–300	45.4%	2.02	0.99	1.97	2.90	3.98	3.20

Table 5.3: Fitted parameters for Ni–Si infiltrations using β = 1.3 and $\widetilde{D}$ = 8.35 x 10^{-14} m^2/s.

D_{powder} (μm)	ε	T	H	τ	α	$T \cdot \tau$	α (τ = 3.6/T)
63–74	40.1%	1.45	0.71	2.74	0.92	3.97	0.94
90–104	41.8%	1.76	0.82	2.41	1.09	4.24	1.12
250–300	46.6%	2.02	0.99	1.42	1.89	2.87	1.54

Table 5.4: Fitted parameters for copper infiltrations using β = 1.65 and $\widetilde{D}$ = 2.2 x 10^{-13} m^2/s.

There appears to be significant variation in both τ and α from one experiment to another, with no clear reason. Some of this variation is attributable to experimental uncertainty, since the two 250–300 micron powder skeletons infiltrated with Ni–Si produced different results. The second of those two skeletons was only 8 cm tall and filled in only 20 seconds, well before freeze-off occurred. Since data was only available over a short time period, the corresponding curve fit is less reliable and these values were not used in any averaging. Using the remaining seven experiments, the mean and standard deviation are $\tau = 2.0 \pm 31\%$ and $\alpha = 1.46 \pm 31\%$.

To make the model useful as a predictor of infiltration distance, it is necessary to identify the parameters τ and α in some universal way. The data suggests a possible inverse relationship between the tortuosity factor T and the curve fit parameter τ. Their product is included in the table and indeed the variance is significantly reduced, $T\tau = 3.6 \pm 15\%$. The final column shows the corresponding parameter α found from equation 5.9 using the suggested dependence of τ. The resulting deviation in the second parameter is reduced as well, $\alpha = 1.36 \pm 29\%$, although only slightly. No doubt there are many different physical phenomena responsible for defining these parameters, but the limited data set with some intrinsic variability prevents a definitive explanation. Use of a dynamic wetting angle would cause a dependence of the capillary pressure on the infiltration rate. Deviation from the Kozeny–Carman model is likely as the solidifying geometry no longer resembles packed spheres. This could be represented by a tortuosity factor

that changes with volume fraction. The rate of solidification is directly proportional to α, and since a value of 1 would correspond to a match between the permeability decay and the prediction based on the sphere growth solidification model, the observed fits for α correspond roughly to a 50% higher solidification rate. Experimental results with 50 μm diameter wire in Chapter 3 already exhibited a factor of two higher solidification rate than expected by theory using the literature value for diffusivity. This rate might be further increased in the powder if it has a finer grain size. Nonetheless, the model captures the general behavior of infiltration into a skeleton during diffusional solidification and makes a reasonable prediction of limitations to the infiltration height due to freeze-off. The following plots show how the universal model would have faired in predicting the behavior for each of the experiments.

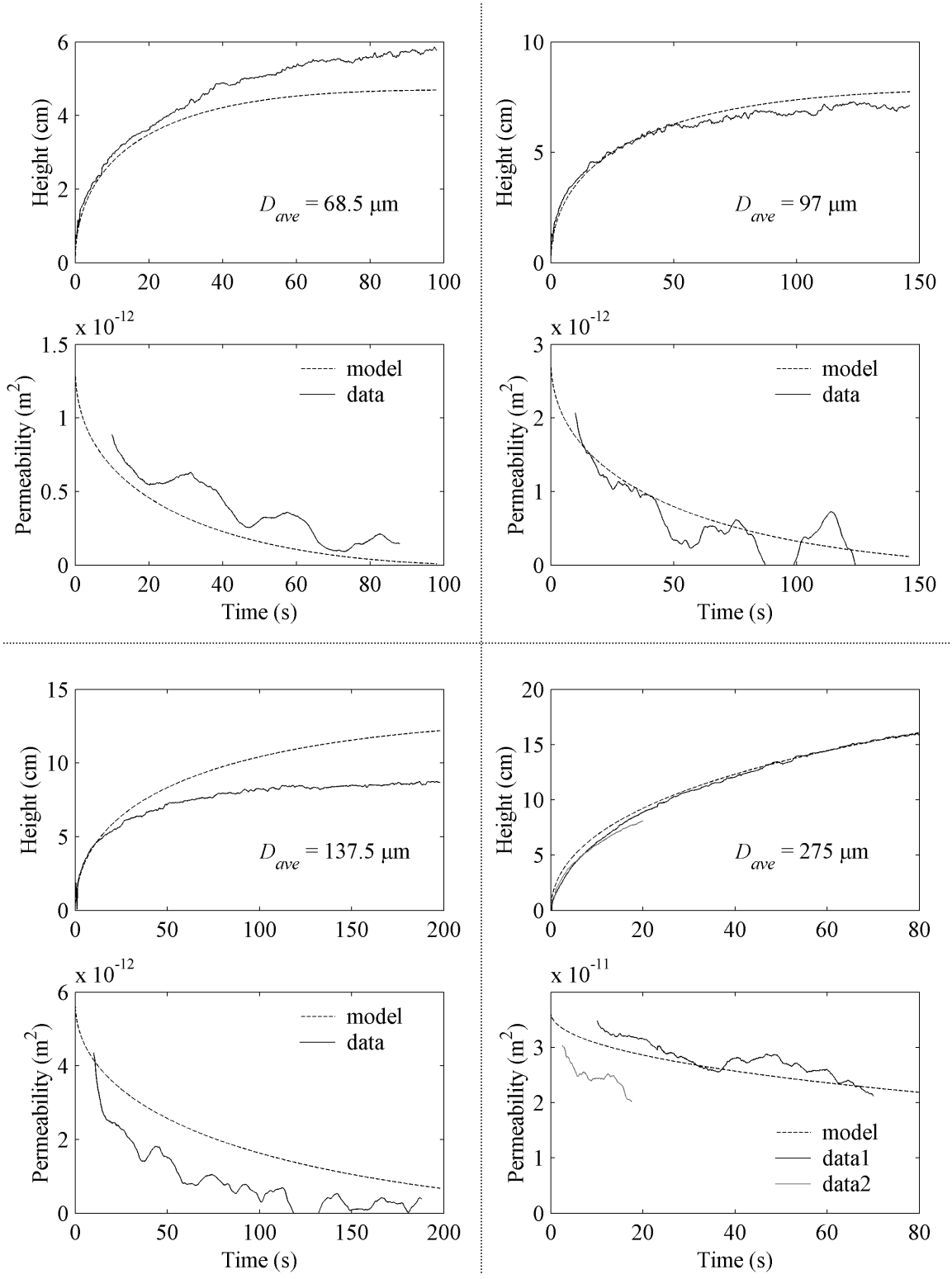

Figure 5.10: Infiltration rate experiments with Ni–Si and model ($\tau = 3.6/T$, $\alpha = 1.4$).

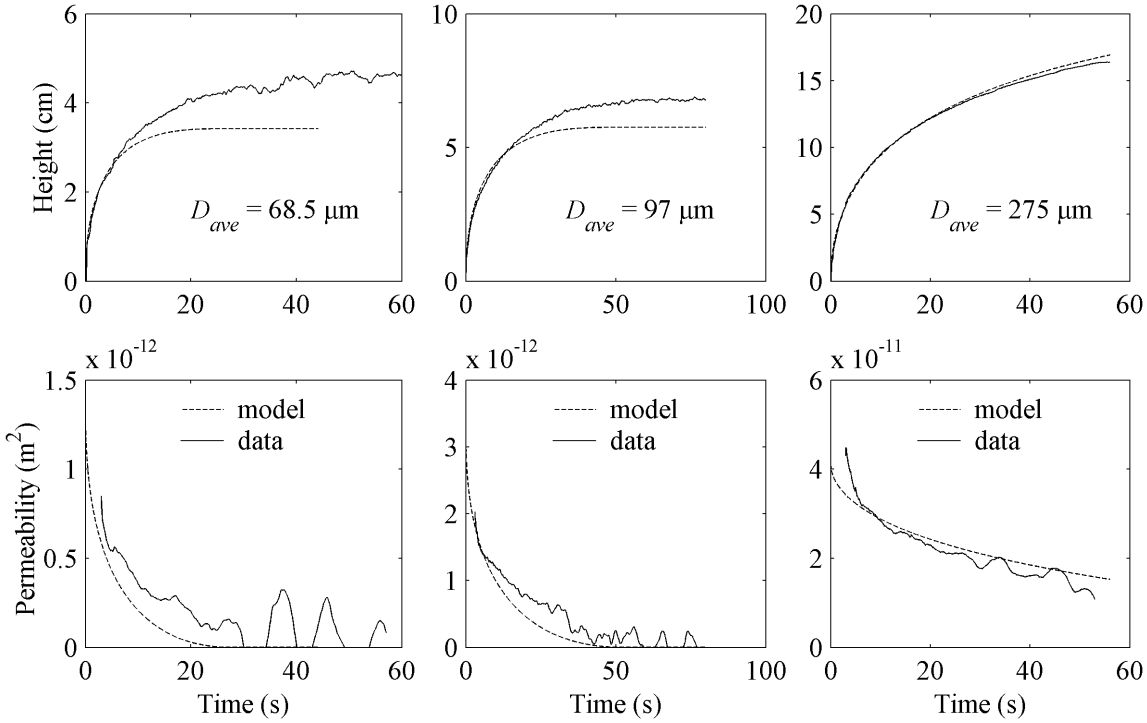

Figure 5.11: Infiltration rate experiments with copper and model ($\tau = 3.6/T$, $\alpha = 1.4$).

The final infiltration height predicted by the model is generally within about 20% of the measured value for both material systems. The solidification parameters β and $\widetilde{D}$ are the only difference in the model for infiltration with Ni–Si and infiltration with copper. Furthermore, because the model fit to the observed data suggests the product (τT) to be constant, the tortuosity factor, T does not play a significant role in the model for the given conditions. The only experimentally determined parameter to play a role is H, which could be neglected when using the model for first order approximations.

5.7 Implications of the TLI rate model

Using this relatively universal permeability model, we can determine the dependence of the infiltration height limit on powder size. For infiltration heights less than 10–20 cm, the loss of fluid driving pressure to gravitational head is quite small, and the limitations to vertical and horizontal infiltrations are identical. This can be seen clearly in Figure 5.12, showing how the model predicts dependency on powder size for the two infiltrants.

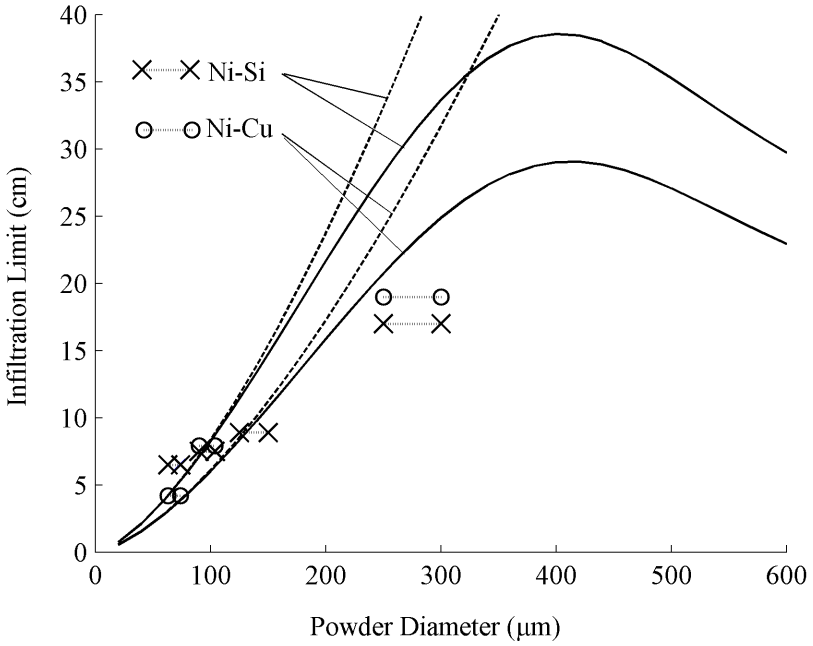

Figure 5.12: Dependence of infiltration limits on powder size based on TLI model. Dashed lines are for horizontal infiltration ignoring the effect of gravity. Experimental results from section 5.6 are superimposed to show the height achieved with skeletons of the given size range, X for Ni–Si and O for Ni–Cu. Both skeletons of 250–300 μm powder filled to the top of the skeleton and therefore represent minimum values.

The maximum value for vertical infiltration limit occurs for both materials in the range of 300–400 μm powder, signifying a transition from the freezing limit to the capillary rise limit. For powder sizes larger than 500 mm, the inertial body forces become more significant and the fluid flow will begin to deviate from the Darcy's Law. Below the capillary limit, the curve indicates that a doubling of powder size would result in slightly more than doubling of the infiltration limit. For infiltrant with a slower diffusing melting point depressant, the slope would be steeper, the peak infiltration limit would be higher, and the transition to limitation by capillary rise would occur at a smaller powder size. This would be the case for copper as compared to Ni–Si, except that the lower surface tension causes the peak to be lower as well. An infiltrant with a very fast melting point depressant would conversely have a more gradual slope, a lower peak infiltration limit, and would not transition to a capillary rise limit until a larger powder size. For such a case, it is reasonable to neglect the gravitational head loss in the model, and equation 5.2 can be integrated directly with the model of equation 5.6 substituted for *K(t)*:

$$\int_0^{h_{limit}} h \cdot dh = \frac{HD\varepsilon\gamma'}{30\tau T\mu(1-\varepsilon)} \int_0^{1/Z^2} \left(1 - 2Z\sqrt{t} + Z^2 t\right) \cdot dt \quad \text{where} \quad Z = \alpha(1+5\varepsilon)\frac{2\beta\sqrt{4\widetilde{D}}}{D} \qquad (5.10)$$

The curve fit for *K(t)* is valid until the permeability reaches zero at $t_{final} = 1/Z^2$, at which point the height is equal to the horizontal infiltration limit.

$$h_{limit} = \sqrt{\frac{HD\varepsilon\gamma'}{15\tau T\mu(1-\varepsilon)} \cdot \frac{1}{6Z^2}} = \sqrt{\frac{H}{1440\tau T\alpha^2} \cdot \frac{\varepsilon}{(1-\varepsilon)(1+5\varepsilon)^2} \cdot \frac{D^3\gamma'}{\mu\beta^2\widetilde{D}}} \tag{5.11}$$

The effect of the void fraction on the infiltration is actually quite small due to several offsetting influences. For constant permeability, a smaller void fraction creates greater capillary pressure, but is more than offset by the smaller permeability. The net effect on infiltration distance without freezing follows ε/(1- ε) and can result in 20% greater distance by increasing from 0.4 to 0.5. In the case of freezing as in TLI, the term (1+5ε) is derived in section 4.3.2 and represents how the permeability change is faster in a skeleton of higher initial void fraction. The effects offset each other and the combination of all the terms in equation 5.11 that include void fraction results in less than a 5% difference in height limit over a wide range of $0.35 < \varepsilon < 0.5$. Substitution of H=1, $T\tau$=3.6, α=1.4 and ε=0.4 reduces equation 5.11 to the following:

$$h_{limit} = 2.8 \times 10^{-3} \sqrt{\frac{D^3\gamma'}{\mu\beta^2\widetilde{D}}} \tag{5.12}$$

The preceding equations neglect the effect of gravity, which can begin to play a significant role for large parts and large powder sizes. For vertical infiltration as shown in Figure 5.13, the effect of void fraction for small powder once again is very small, but for large powder the effect can be greater due to the influence of void fraction on the capillary limit.

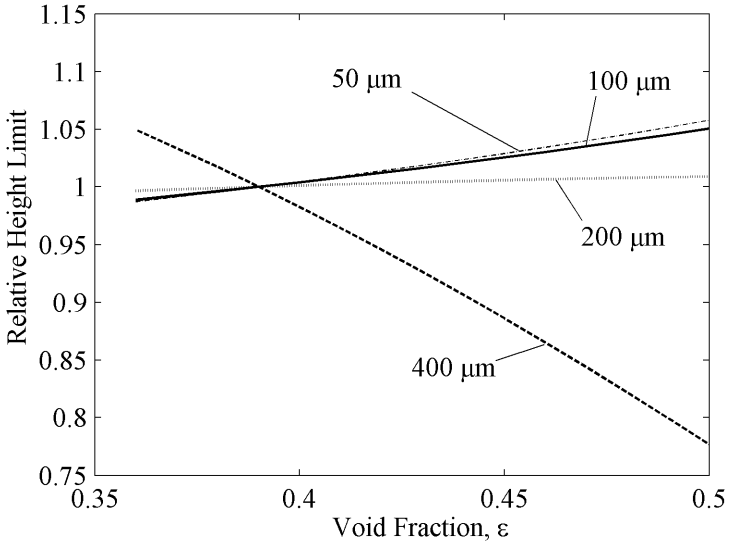

Figure 5.13: Influence of void fraction on vertical infiltration limits generated from model to include the effect of gravity.

Chapter 6: Conclusions

6.1 Overview

The impact Transient Liquid-Phase Infiltration has on the PM and SFF industries will be determined by the usefulness of parts that can be made using this new method of densification. Specifically, this 'usefulness' can be defined in terms of the achievable material properties and part geometries. To address these aspects of TLI, Chapters 2 and 3 presented the important materials issues and Chapters 4 and 5 delved deeper into the limitation that freeze-off can impose on part geometry. Each of the major issues introduced in section 1.3 has been presented in general terms so as to apply to a variety of material systems. The two material systems developed experimentally in this work, Ni–Si and Ni–Cu, were successfully used to test the understanding of the physical mechanisms playing a role in TLI.

6.2 Materials conclusions

The solidification rate is determined primarily by diffusion of the MPD into the solid skeleton. The motion of the solid liquid interface can be described by

$$X(t) = \beta\sqrt{4\tilde{D}t} \tag{6.1}$$

for semi-infinite, one-dimensional geometry and constant diffusivity. β is determined from the MPD solubility and the width of the solid/liquid two-phase field. This relationship is described in equation 2.9 and plotted in Figure 2.2. The diffusivity can be found in literature.

Numerical simulations were used to show the effect of finite boundary conditions and curved geometry on the solidification rate. Described in section 2.2.1, finite boundary conditions were shown not to affect the interface motion until the solid became nearly saturated with MPD. For a skeleton containing no MPD, the effect on solidification rate is negligible for cases when the partition coefficient, C_s/C_l, is greater than the initial volume fraction of the skeleton. In section 2.2.3, cylindrical and spherical geometry was shown to decrease the motion of the interface relative to the planar case. The decrease is proportional to both curvature and elapsed time, and the effect is fairly small for the large powders and short times of interest in TLI.

For cases of concentration-dependent diffusivity, interface motion is determined by mass flux using the local diffusivity and concentration gradient at the interface. The diffusivity at the

interface is based on the solidus concentration, but the concentration gradient is affected by the diffusivity elsewhere. The numerical simulations in section 2.2.2 showed that the interface motion was once again proportional to the square root of time as in equation 6.1, despite significant variation in diffusivity with the Ni–Cu system. The motion can therefore be represented by an effective diffusivity that lies somewhere between the diffusivity in the pure skeleton material and the diffusivity at the interface. This effective diffusivity followed more closely to that of the solidus concentration for the Ni–Cu system as shown in Figure 2.8, but generalization is not recommended since the effective diffusivity will depend on the specific concentration dependence of diffusivity for a given materials system.

The quenching experiments described in section 3.2 provided a simple and accurate method for measurement of the solidification rate. The observed solidification rate in the Ni–Si materials system was approximately twice as fast as predicted by theory. This difference is likely due to penetration of liquid and subsequent higher rates of diffusion along grain boundaries, which has been observed by prior researchers in other materials systems.

Significant dissolution of a skeleton occurs when it is dipped into an infiltrant pool that can absorb the skeleton material. Presaturating the infiltrant can prevent this gross part erosion because the liquid is already at thermodynamic equilibrium. However, further erosion can result if the latent heat released during solidification increases part temperature and allows more dissolution. The temperature rise depends on the solidification time, which is a strong function of powder size, and the external part geometry, which limits the dissipation of heat, as given by equation 2.20. Experimental observations show the erosion to be in general less severe than predicted by equation 2.22, but support the prediction that this type of erosion is more severe for skeletons of smaller powder.

The bulk composition of a part made by TLI remains uniform along with path of infiltration for a binary system with presaturated infiltrant. This is ensured because the liquid composition does not change as it flows into the part. Compositional analysis of an infiltrated Ni–Si part supported this prediction. Uniform composition cannot be guaranteed for ternary and higher systems because solidification can result in a change of composition in the remaining liquid even if the infiltrant begins at a liquidus composition.

After infiltration and heat treatment sufficient for homogenization of MPD concentration, Ni–Si parts made by TLI were compared to cast material of the same composition. The density of the infiltrated and homogenized parts was lower than the cast parts, suggesting the presence of some residual porosity. Tensile tests showed similar elastic behavior for the parts made by TLI and casting. Above the yield strength, the TLI parts failed after only 3–5% elongation and at a lower UTS, most likely as a result of the porosity. After HIP treatment of the TLI parts, the density increased to match that of the cast samples as did the ductility and UTS. The TLI parts after HIP treatment maintained a finer grain size than the castings, resulting in more isotropic deformation throughout the tensile bar.

6.3 Infiltration limits from freeze-off

Fluid flow during capillary infiltration of a powder skeleton can be adequately described by the differential equation:

$$\frac{dh}{dt} = \frac{K}{\varepsilon\mu h}\left(H\frac{6\gamma'(1-\varepsilon)}{D\varepsilon} - \rho g h \right) \tag{6.2}$$

for viscous-dominated flow with the variables as defined in sections 4.1 and 4.2. Skeleton permeability K was measured directly via permeametry as described in section 5.1. The parameter H was used introduced to account for differences between the actual capillary pressure of the skeleton and that predicted by a uniform diameter sphere model. Figure 5.4 shows very close agreement of the solution to equation 6.2 with measurements of infiltration rates using oil of known fluid properties.

The measured permeability for different skeletons was compared with the Kozeny–Carman model of equation 4.11 to determine a tortuosity factor T characteristic of each powder size range. Neglecting the gravitational term of equation 6.2 and substitution of the Kozeny–Carman model for permeability allows a simple solution for infiltration height (or distance, since gravity is neglected).

$$h(t) = \sqrt{\frac{H}{T}\cdot\frac{D\varepsilon\gamma' t}{15\mu(1-\varepsilon)}} \tag{6.3}$$

This relation is useful for determining the influence of each parameter on the infiltration distance for a skeleton of constant permeability.

Measurement of infiltration rate with liquid metal was done through mass increase as described in section 5.4. The changing permeability of the freezing skeleton was determined by solving equation 6.2 for K with the measured infiltration rate. A model for the permeability change was developed based on a simple cubic lattice structure, a growth rate for each powder radius according to equation 6.1, and the Kozeny–Carman model prediction of permeability using the volume fraction and surface area of the unit cell. The permeability calculated from the measured infiltration height typically was smaller and decreased faster than the model prediction. A reasonable curve fit to the measured permeability change was found using the following expression for permeability:

$$K_{fit} = \frac{K_{K-C}}{\tau} \cdot \left(1 - \alpha\left(1 + 5\varepsilon\right) \frac{\beta\sqrt{4\tilde{D}t}}{D/2} \right)^2 \tag{6.4}$$

where τ and α were introduced to adjust the initial permeability value and the rate of decay respectively to match experimental observations, discussed in more detail in sections 4.3.2 and 5.6. In the case of a perfect match between experiments and the prediction of permeability change by the unit sphere growth model, both parameters would equal one. Some possible explanations for the faster freeze-off were discussed in section 5.6, along with the characterization for the Ni–Si and Ni–Cu systems. Suggested values for τ and α were chosen based on the experimental data in these two material systems, but understanding of the physical phenomena that determine these values is still somewhat lacking.

This expression for variable permeability given by equation 6.4 was used in the fluid flow model of equation 6.2 and solved to find the following general expression for the infiltration distance limit (neglecting gravity) due to freeze-off in transient liquid-phase infiltration with the parameters described below.

$$h_{limit} = \sqrt{\frac{H}{1440\alpha^2 T\tau} \cdot \frac{\varepsilon}{\left(1-\varepsilon\right)\left(1+5\varepsilon\right)^2} \cdot \frac{D^3\gamma'}{\mu\beta^2\tilde{D}}} \tag{6.5}$$

T – tortuosity factor determined by oil permeametry and comparison to Kozeny–Carman prediction of permeability as described in section 5.1.

H – height factor introduced to match actual capillary pressure of the skeleton to that predicted by the uniform diameter sphere model, determined from measurement of infiltration rate with oil in section 5.2.

τ and α – determined by curve fit to experimental measurements of infiltration rate for Ni–Si and Ni–Cu as described in section 5.6.

ε – initial void fraction of the powder skeleton determined by comparing skeleton density to theoretical density of solid skeleton material.

D – representative powder diameter. For powder sieved between two mesh sizes, D is typically chosen as the median value. If powder size distribution is known, D could be chosen as the weighted average.

γ' – surface tension force acting on the skeleton, inclusive of wetting angle effects. This was measured directly for Ni–Si as described in section 5.3.2.

μ – viscosity of the liquid infiltrant. This was measured directly for Ni–Si as described in section 5.3.3.

β – solidification rate coefficient determined from solidus and liquidus concentrations and Figure 2.2 or alternatively through direct measurement of solidification rate via quenching experiments as described in section 3.2.2.

$\widetilde{D}$ – chemical diffusion coefficient of the MPD in the solid skeleton found in literature and generally reported as an Arrhenius function of temperature. For diffusivity that is a strong function of concentration, an effective diffusivity representative of the interface motion can be determined as described in section 2.2.2.

Based on the experimental measurements of permeability with Ni–Si and Ni–Cu, the following substitutions can be made: $T\tau$=3.6, and α=1.4 as discussed in section 5.6. Further, for most skeletons the height factor is close to one, so a good approximation can be made by substituting H=1. The terms including the skeleton void fraction are fairly insensitive to variation in ε in the range from 0.35 to 0.55. Using a typical value of ε=0.4, equation 6.4 can be simplified to:

$$h_{limit} = 2.8 \times 10^{-3} \sqrt{\frac{D^3 \gamma'}{\mu \beta^2 \widetilde{D}}} \tag{6.5}$$

providing a very simple estimate for the freeze-off limit that is useful for selection of processing parameters and evaluation of potential new material systems.

The numerical simulation described in section 5.6 further includes the effect the gravitational head can have on the capillary driving pressure, which becomes significant for conditions when the freeze-off limit approaches the capillary rise height limit. When the freeze-off limit is

significantly greater than the capillary rise limit, it no longer plays a role and the behavior is similar to a traditional infiltration.

6.4 Recommendations for future work

The Ni–Si material system was selected for experimental work because of the common use of similar alloys as brazing material, the simplicity of analysis for a binary system and its well-known equilibrium thermodynamic properties. Because the silicon content in most nickel superalloys is typical very small, it may not be possible to match the composition of commercially significant alloys such as Inconel 718 using TLI. However, the addition of other alloying elements to the binary system will help achieve more desirable final material properties. Infiltration at higher temperatures could also further decrease the silicon content in the final part. Work with ternary systems such as Ni–Cr–Si would also provide an opportunity to test the uniformity of composition along the infiltration path as discussed in section 2.4.

The Ni–Cu system is more likely to allow TLI fabrication of final parts equivalent to existing commercial alloys, namely Monel 400 and K–500 which consist primarily of 30 wt% copper in nickel. Further work with this materials system should include more extensive analysis of the microstructure after infiltration and during homogenization. Because this TLI system involves significantly greater mass transport, there is increased likelihood of Kirkendall porosity. The rate of solidification for Ni–Cu in this work was predicted using the solidus and liquidus concentrations to find β and the values of diffusivity from literature (including the variation with composition). Quenching experiments as in section 3.2.1 would provide verification of the solidification rate in this system and test the predictions of an effective diffusivity from the simulations of variable diffusivity in section 2.2.2. For the Ni–Cu system, both the quenching experiments and the infiltration rate experiments could be conducted at higher temperatures to test the prediction of solidification rate temperature dependence given in section 2.1.3.

The amount of erosion resulting from latent heat release during solidification as described in sections 2.3 and 3.4 will depend on the characteristic enthalpy change of a given materials system, with some systems being more prone to erosion than others. The temperature increase in a part during TLI could be measured to learn more about this mechanism. Conducting experiments with different part geometry could test how heat dissipation might control erosion, with thicker parts expecting to rise more in temperature.

Development of TLI to fabricate steel parts could be achieved using either silicon or carbon as primary melting point depressants. The equilibrium phase diagrams for the two binary systems are shown in Figure 6.1 to aid in the selection of infiltrant composition and infiltration temperature and corresponding parameters to estimate the TLI freeze-off limits.

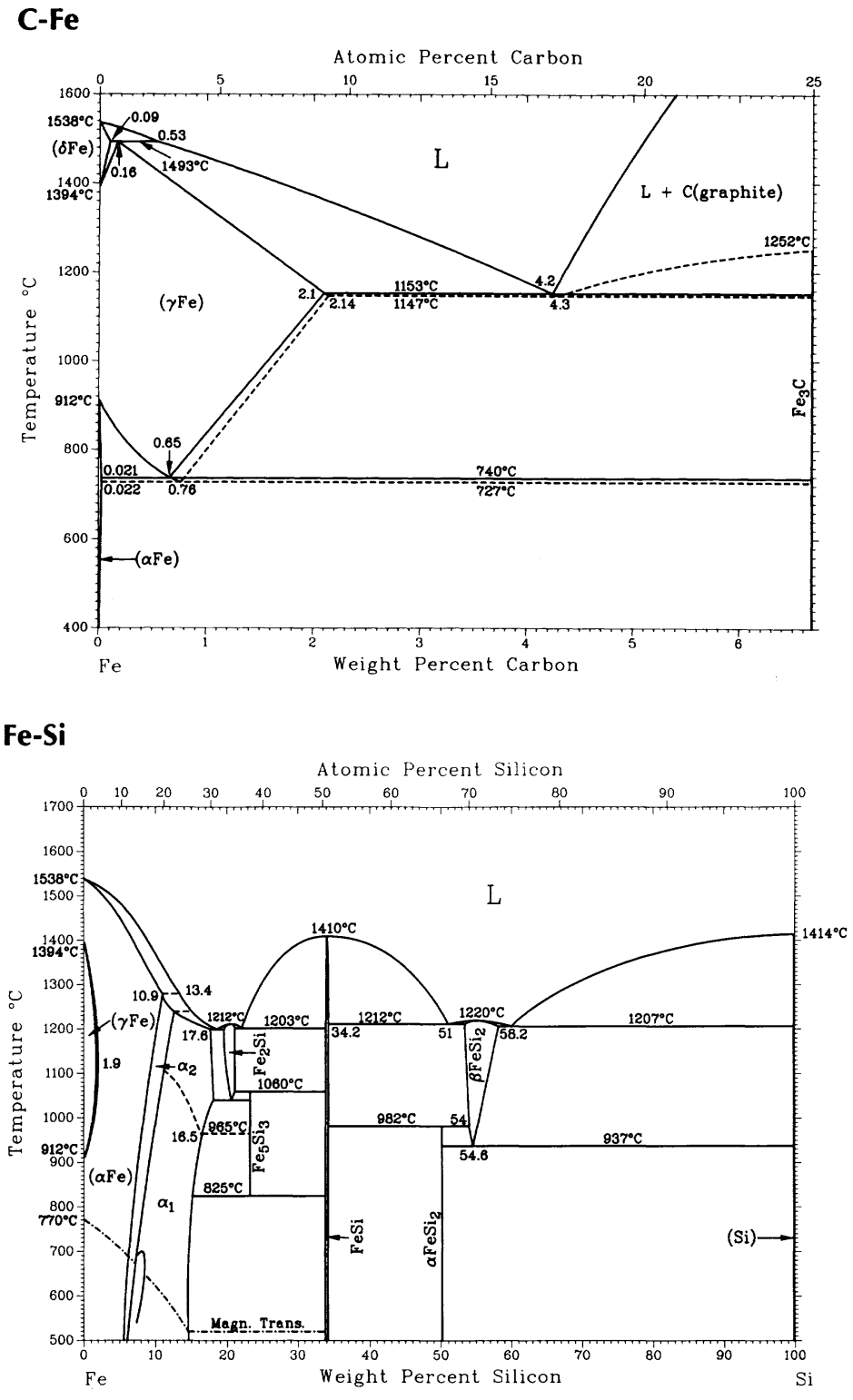

Figure 6.1: Equilibrium phase diagrams for Fe–C and Fe–Si.[17]

The use of carbon offers significantly greater potential to match existing commercial alloys, which often contain over 1 wt% C. Infiltration at 1300°C would correspond to an infiltrant

composition of 2.7 wt% C from the liquidus curve of the phase diagram and result in a final composition near 1 wt% C. At this temperature, the solidification rate would be given by $\widetilde{D} = 8.7 \times 10^{-10}$ m^2/s[13] and $\beta = 0.36$. The fluid properties of pure iron at its melting point provide reasonable estimates for the surface tension, viscosity and density: $\gamma = 1.8$ N/m, $\mu = 5.5$ mPa-s, $\rho = 7$ g/cc. The majority of commercial steel alloys contain less than 1 wt% Si, but some have up to 3–4 wt% Si. An infiltration temperature of 1400°C using Fe–Si would use an infiltrant composition of 9 wt% Si, the corresponding solidification rate would be given by $\widetilde{D} = 2.8 \times 10^{-11}$ m^2/s[13] and $\beta = 0.71$, and once again the fluid properties could be approximated by those of pure iron. The freeze-off limit for a horizontal infiltration can be determined using these values in equation 6.5 and the numerical simulation in section 5.6 provides the limits for a vertical infiltration including the effects of gravitational head loss.

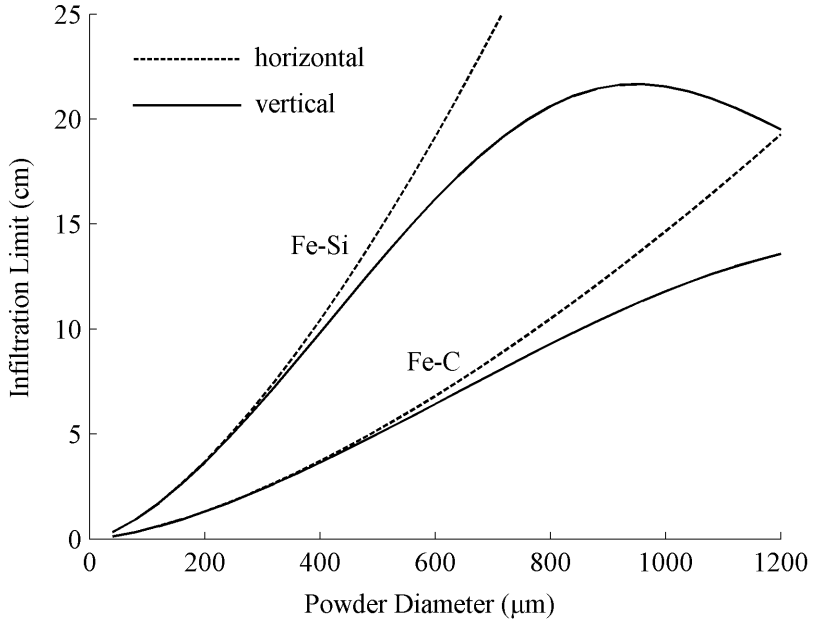

Figure 6.2: Prediction of size limitations due to freeze-off in TLI for steel parts.

This provides an example of how the understanding of TLI developed in this thesis can be used in the selection of new materials systems. Several rough approximations are implicit in these predictions, but they still provide a useful basis for decision making. The predictions of Figure 6.2 are based on the observations in the nickel systems and the corresponding values of τ and α used in equation 6.4. Further measurements of infiltration rate in other material systems could help provide insight into what factors influence these parameters.

The diffusivity can change dramatically with crystal lattice structure, which could play a significant role in the Fe–Si system that changes from fcc to bcc with increased silicon content. The diffusivity value presented in the previous paragraph is based on the bcc lattice at 4 at% Si and changes by only a factor of two within the alpha-phase. The diffusivity in the gamma-phase is ~50 times slower, and could cause significant retardation of the solidification rate. This situation is somewhat similar to the variable diffusivity of Ni–Cu presented in 2.2.2, but involves a step change in diffusivity and an additional interface between the two solid phases. Quenching experiments in conjunction with a modified numerical diffusion model could provide better understanding of how the solidification rate is effected. Addition of other elements to stabilize the gamma phase might allow significantly greater infiltration distances.

Appendices

Appendix A: Matlab M-file simulation of diffusional solidification

```
% Diffusional solidification simulation based on Tanzilli and Heckel's model
% as described in Transactions of the Metallurgical Society of AIME
% Volume 242, Nov 1968, pages 2313-2321.
% Written for Matlab by Adam Lorenz - November 2001

% Sample values based on Ni–Si at 1185°C
Da=8.35e-14;            %Diffusivity in the Beta phase (m^2/s)
Db=8.35e-14;            %Diffusivity in the Alpha phase (m^2/s)
Cb=0.138;               %Equilibrium concentration in Beta (solidus comp)
Ca=0.196;               %Equilibrium concentration in Alpha (liquidus comp)

width_b=2.5e-5;         %initial width of Beta phase, left side (meters)
width_a=2.5e-5;         %initial width of Alpha phase, right side (meters)
r=40;                   %Number of nodes in Beta portion (also node of interface position)

i=width_b;              %set interface position i
L=width_b+width_a;      %calculate total width L
N=round(r+(L-i)/i*(r-2));  %calculate total number of nodes

%set initial concentration profile
C=zeros(N+1,1);
C(r:N+1)=Ca;            %set right half at liquidus composition

%initialize variables
j=1;dt=0;int_vel=0;x=0;mass=0;
elapsed_time=0;
runtime=1000;           %time for simulation to run (seconds)
while elapsed_time<=runtime
  dxb=i(j)/(r-2);                       %mesh size in Beta phase
  dxa=(L-i(j))/(N-r);                   %mesh size in Alpha phase
  dt(j)=min([ 0.2*dxb^2/Db 0.2*dxa^2/Da]);%time step must be less than 0.25*dx^2/D for stability
  elapsed_time(j+1)=elapsed_time(j)+dt(j);

  %Calculate interface motion based on mass flux balance
  int_vel(j)=1/(Cb-Ca)*[Da*(-C(r+2,j)+4*C(r+1,j)-3*Ca)/(2*dxa) ...
              - Db*(C(r-2,j)-4*C(r-1,j)+3*Cb)/(2*dxb)];
  i(j+1)=i(j) + int_vel(j)*dt(j);

  %Apply Fick's law to Alpha phase (right side)
  C(r,j)=Ca;
  for   n=r+1:N
    C(n,j+1)=C(n,j) + dt(j)*[(N-n)/(L-i(j))*(C(n+1,j)-C(n-1,j))/2*int_vel(j) ...
              + Da*(C(n-1,j)-2*C(n,j)+C(n+1,j))/dxa^2];
  end;

  %Apply Fick's law to Beta phase (left side)
  C(r,j)=Cb;
  for n=2:r-1
```

```
    C(n,j+1)=C(n,j) + dt(j)*[(n-2)/i(j)*(C(n+1,j)-C(n-1,j))/2*int_vel(j) ...
        + Db*(C(n-1,j)-2*C(n,j)+C(n+1,j))/dxb^2];
  end;

  %reset boundary conditions for zero mass flux boundaries
  C(1,j+1)=C(3,j+1);
  C(N+1,j+1)=C(N-1,j+1);

  %Extra calculations for use while plotting
  x(j,1:N-1)=[([2:r]-2)*dxb,(r-2)*dxb+[1:N-r]*dxa];

end;
plot(1e6*x(j,:),100*C(2:N,j));
```

Appendix B: Matlab M-file of liquid flow model using variable permeability

```
% Transient Liquid-Phase Infiltration Model
% Written by Adam Lorenz – March 2002

% Predicts the rise height of liquid metal into a porous skeleton
% based on the following model:
% dh/dt = (K/(e*mu*h))*((6*gamma*(1-e))/(De)-rho*g*h)

%Sample properties based on Ni–Si at 1185°C
%Fluid properties
rho=7200;               % density [kg/m^3]
mu=0.0105;              % viscosity [Pa-s]
gamma=1.4;              % surface tension [N/m]
g=9.81;                 % acceleration due to gravity [m/s^2]
%Solidification properties
Diff=8.35e-14;          % Diffusivity of MPD in Skeleton [m^2/s]
M=1.3;                  % value for beta based on growth of interface in wire experiments

%Skeleton properties
D=68.5e-6;              % average powder diameter [meters]
e=0.403;                % void fraction
T=1.45;                 % Tortuosity factor based on oil permeametry expmts
H=0.71;                 % Height factor based on oil infiltration rate expmts
t_end=98;               % Time when sample was removed from melt [sec]
N=200;                  % Number of points to average dh/dt over



%%%%%%%%%%%%%%%%%%%%%%%%%%%%%%%%%%%%%%%%%%%%%%%%%%%%%%%%%%%%%%%%%%%%%%%%%%%%%%%
% Calculation of permeability change with time based on growth of a sphere in a unit cell
%%%%%%%%%%%%%%%%%%%%%%%%%%%%%%%%%%%%%%%%%%%%%%%%%%%%%%%%%%%%%%%%%%%%%%%%%%%%%%%

%Resolution of time steps set by n, where the total time is the sum of
% 0+dt+2dt+3dt+...+ndt and dt=2*tfinal/(n^2-n),  t(1)=0, t(n)=tfinal.
n=500;
tfinal=(0.15*D/M)^2/(4*Diff);  % time til porosity closed off, X=0.15*D [seconds]
if tfinal >t_end   tfinal=t_end; end; %when comparing to experiments, only need to calculat
t=((1:n).^2-(1:n))/(n^2-n)*tfinal;
% Solidification distance given by X = M*sqrt(4*Diff*t)
r=D/2+M*sqrt(4*Diff*t);                 % Radius of growing sphere

% Volume fraction solid as a function of growing radius
cap=pi.*(r.^2.*(r-D/2)-(r.^3-(D/2)^3)/3);
sphere=4/3*pi.*r.^3;
volumefrac=(sphere-6*cap)/D^3;
% Surface/volume ratio as a function of growing radius
caps=2*pi.*r.*(r-D/2);
spheres=4*pi.*r.^2;
surface=(spheres-6*caps)./(volumefrac*D^3);
%Offset for actual initial packing density (unit cell is 52.4% dense)
volumefrac=1-(1-volumefrac)*e/(1-volumefrac(1));
% Permeability based on Kozeny-Carman model including tortuosity factor
K=(1-volumefrac).^3./(5.*surface.^2.*volumefrac.^2)/T;
```

```
%%%%%%%%%%%%%%%%%%%%%%%%%%%%%%%%%%%%%%%%%%%%%%%%%%%%%%%%%%%%%%%%%%%%%%%%%%%%
% Numerical simulation for infiltration rate with permeability changing in space and time
%%%%%%%%%%%%%%%%%%%%%%%%%%%%%%%%%%%%%%%%%%%%%%%%%%%%%%%%%%%%%%%%%%%%%%%%%%%%

h=0;                    %initialize height array [meters]
%select appropriate value for initial height based on time step
h(2)=sqrt((4*tfinal/(n^2-n))*K(1)/(e*mu)*(6*gamma*(1-e)/(D*e)));
R=h(2)/K(1); %initialize R
for         i=2:n-1
  % define indices m such that t(m) corresponds the time the
  % liquid has been in contact with the skeleton at a given height
  m=round((1+sqrt(1+4*(i^2-(2:i).^2-i+(2:i))))/2);
  % R(i) accounts for the spatial variation in permeability K as the sum of resistors in series, where
  % each height segment contributes dh/K
  R(i)=sum(diff(h)./K(m));
  h(i+1)=h(i)+i*2*tfinal/(n^2-n)/(R(i)*e*mu)*(6*gamma*(1-e)/(D*e)-rho*g*h(i));
end;
R(n)=R(n-1);



%%%%%%%%%%%%%%%%%%%%%%%%%%%%%%%%%%%%%%%%%%%%%%%%%%%%%%%%%%%%%%%%%%%%%%%%%%%%
% Extract permeability from experimental measurements of height (array NiSi_68 for sample skeleton)
%%%%%%%%%%%%%%%%%%%%%%%%%%%%%%%%%%%%%%%%%%%%%%%%%%%%%%%%%%%%%%%%%%%%%%%%%%%%

hdata=NiSi_68(1:20*t_end);
tsegment=[ [-N+1:N]'/20 ones(2*N,1)];  % matrix used for linear regression
V=0;
for i=N:length(hdata)-N
   linefit=(tsegment\(hdata(i-N+1:i+N)));
   % finds the least squares fit to the data over +/- N points
   V(i)=linefit(1)/100;     % determines front velocity, dh/dt [m/s]
end;
Kdata=V'*e*mu*0.01.*hdata(1:length(hdata)-N)...
   ./ (6*gamma*(1-e)/(D*e) - rho*g*0.01*hdata(1:length(hdata)-N));



%%%%%%%%%%%%%%%%%%%%%%%%%%%%%%%%%%%%%%%%%%%%%%%%%%%%%%%%%%%%%%%%%%%%%%%%%%%%
% Determine parameters alpha (B2) and tau (T2) for curve fit to measured permeability
%%%%%%%%%%%%%%%%%%%%%%%%%%%%%%%%%%%%%%%%%%%%%%%%%%%%%%%%%%%%%%%%%%%%%%%%%%%%

% Permeability based on Kozeny-Carman model including tortuosity factor
Ko=e^3./(5*(6/D)^2*(1-e)^2)/T;
B=1+5*e;
tfit=[N/20:0.05:t_end-N/20]';
X=M*sqrt(4*Diff*tfit);
F=(Ko*[ones(size(X)) 2*B*X/D (2*B*X/D).^2])\(Kdata(N:20*t_end-N));
T2=1/F(1);% or 3.6/T for universal fit
B2=real((2*B*X/D)\(1-sqrt(Kdata(N:20*t_end-N)*T2/Ko)));% or B2=1.4 for universal fit
```

```
%%%%%%%%%%%%%%%%%%%%%%%%%%%%%%%%%%%%%%%%%%%%%%%%%
% Define permeability based on curve fit
%%%%%%%%%%%%%%%%%%%%%%%%%%%%%%%%%%%%%%%%%%%%%%%%%%

%Resolution of time steps set by n, where the total time is the sum of
% 0+dt+2dt+3dt+...+ndt and dt=2*tfinal/(n^2-n),  t(1)=0, t(n)=tfinal.
n=500;
tfinal=(0.15*D/M)^2/(4*Diff);  % time til porosity closed off, X=0.1*D [seconds]
if tfinal > 1*t_end   tfinal=1*t_end; end;
t=((1:n).^2-(1:n))/(n^2-n)*tfinal;
X=M*sqrt(4*Diff*t)';
K=Ko*(1-B2*B*2*X/D).^2/T2;
if interp1(diff(K),1:n-1,0)<n                          % if curve fit reaches out of valid range
   K(round(interp1(diff(K),1:n-1,0)):n)=Ko/1e5;        % set permeability to really small number
end;



%%%%%%%%%%%%%%%%%%%%%%%%%%%%%%%%%%%%%%%%%%%%%%%%%%%%
% Numerical simulation for infiltration rate based on Kfit
%%%%%%%%%%%%%%%%%%%%%%%%%%%%%%%%%%%%%%%%%%%%%%%%%%%%
h=0;                    %initialize height array [meters]
%select appropriate value for initial height based on time step
h(2)=sqrt((4*tfinal/(n^2-n))*K(1)/(e*mu)*(6*gamma*(1-e)/(D*e)));
for         i=2:n-1
   h(i+1)=h(i)+i*2*tfinal/(n^2-n)*K(i)/(h(i)*e*mu)*(6*gamma*(1-e)/(D*e)-rho*g*h(i));
end;



subplot(2,1,1);plot(t,100*h,'k--',0.05:0.05:t_end,hdata(1:20*t_end),'k-');
ylabel('Height (cm)');xlabel('Time (s)');
subplot(2,1,2);plot(t,K,'k--',N/20:0.05:t_end-N/20,Kdata(N:20*t_end-N),'k-');
ylabel('Permeability (m^2)');xlabel('Time (s)');
```

Appendix C: Properties of Multitherm 503 heat transfer oil

The Multitherm 503 oil used for permeability and infiltration tests is a product of:
Multitherm Corporation
125 South Front Street
Colwyn, PA 19023
1-800-225-7440
The physical properties are reported by the manufacturer at:
http://www.multitherm.com/503PP.html
and are summarized in the following table:

T [°C]	ρ [g/cc]	μ [Pa-s]
-18	0.819	40.9
10	0.800	10.2
38	0.782	4.15
66	0.764	2.25
93	0.746	1.39

Table C.1: Properties of Multitherm 503

The values at room temperature (20 °C) were interpolated from the nearest data points of 10°C and 38°C. This led to a density of 0.794 g/cc and a viscosity of 8.04 mPa·s. Because the viscosity is a non-linear function of temperature, it was also tested using a glass capillary viscometer and compared relative to water. This yielded an average value of 8.0 mPa·s, in agreement with the manufacturers specification and this value was used for all calculations.

When the oil is exposed to the air, it changes from clear to yellow in color over the course of several days. A slight increase of the viscosity accompanied the color change, but it is on the same order of the viscosity change due to variations in room temperature from day to day, between 20–22°C. Uncertainty in the viscosity measurement is estimated at ~3%.

Since the manufacturer did not specify a value for surface tension, it was measured using a Rosano Surface Tensionometer by Roller-Smith, employing the Wilhelmy Plate principle. It consists of a precision 500 mg balance with a thin platinum plate that is held at the surface of the test liquid. The surface tension decreased as the oil was exposed to air and began to turn yellow. Four samples of oil in different condition were tested, all at 21°C.

$\gamma = 0.030$ N/m – oil taken directly from 5 gallon container as supplied, clear
$\gamma = 0.029$ N/m – oil exposed for ~12 hours, clear/yellow
$\gamma = 0.027$ N/m – several days of exposure, stored in nalgene bottle, slightly yellow
$\gamma = 0.025$ N/m – several weeks of exposure, stored in open beaker, yellow

The measurements of oil infiltration into powder skeletons were each done using a fresh supply of oil, but typically lasted for several hours. A value of 0.029 N/m was used for all calculations, but there is significant uncertainty of ~5–10%.

Appendix D: Preparation for sintered skeletons of well-defined void fraction

Skeletons were generally prepared by sintering loose powder inside of a mold rather than by using Three-Dimensional Printing since only very simple shapes were required. Because the packing fraction of the skeleton plays an important role in many calculations such as predicting permeability, it is necessary to prepare samples consistently and with well-defined geometry. The packing fraction is calculated by measuring a skeleton's mass and volume and then comparing the apparent density to the solid density of the skeleton material.

For cylindrical skeletons, an alumina tube can be used as a mold by plugging the ends of the tube with packed alumina fiber blanket. Consistent packing fraction was achieved using the following steps:

1. Hold ceramic tube vertically with bottom end resting on lab bench.
2. Stuff alumina blanket into bottom ~1cm of tube and compress it using a metal rod of slightly smaller diameter than the tube ID (rod must be longer than the tube).
3. Use a paper funnel to pour powder into top of tube, tap along the side with metal rod to achieve consistent packing fraction, fill to desired height leaving at least 1 cm at top.
4. Stuff top of tube with additional alumina blanket and compress with rod.
5. Tube can now be held horizontally and transported to furnace for sintering.

Sintering cycles for both nickel and iron powder was 1 hour at 1200°C in an atmosphere of 95% Argon and 5% Hydrogen with 5 C/min heating and cooling rates. For smaller powder, there was sufficient shrinkage during the sintering cycle (a few percent) that the sintered skeleton would easily slide out of the ceramic tube. For powder larger than ~200 μm, this became a problem because the shrinkage was less than the manufacturing tolerance in the tube diameter and samples would be stuck inside the tube. For the larger powder, a slot was milled into a plate of alumina bisque ceramic (available from McMaster-Carr Supply Co.) to form five sides of the mold. A second ceramic plate is held against the first to form the final side of the mold. It is initially clamped in place leaving a small gap at one end to allow powder to be poured in with a funnel as before. Once the powder has filled the mold at tap density, the clamp can be removed and the assembly can be loaded into a furnace taking care not to separate the two halves of the mold.

Initially a thick plexiglass sheet was used as the second plate during the filling of the powder so that the powder was visible. If the plexiglass were lifted away from the powder, electrostatic forces would disturb the powder, so the sheet needed to be removed by sliding it along the top surface. Another ceramic plate would then need to be placed on top of the mold to prevent the powder on the top layer from rearranging while inside the furnace due to sintering forces. The interim step using the plexiglass sheet was cumbersome and eventually deemed unnecessary.

Sintered bars are strong enough for handling, but are still somewhat fragile and can be broken by hand easily. The short plugs for permeametry are broken from longer bar by placing the alumina tube over the two ends of the bar with a gap at the intended breaking point. This enables short segments to be made without any bending. The broken surface must be flattened to accurately the skeleton volume. This can be done with a coarse hand file (slightly more coarse than the powder) so the powder particles are torn loose rather than smeared. Smearing of the particles into the void space would cause additional flow restriction and invalidate any permeability measurements.

Appendix E: Physical properties of liquid metals at melting point[13]

Material	Melting Point [°C]	Density [g/cc]	Viscosity [mPa·s]	Surface Tension [N/m]	Density of solid at 20°C [g/cc]
Aluminum	660.0	2.385	1.30	0.914	2.70
Copper	1083	8.000	4.0	1.285	8.96
Iron	1536	7.015	5.5	1.872	7.87
Nickel	1454	7.905	4.90	1.778	8.89
Silicon	1410	2.51	0.94	0.865	2.34
Silver	960.7	9.346	3.88	0.903	10.5

Table E.1: Properties of liquid metals

Appendix F: Viscosity measurement of liquid metal by capillary method

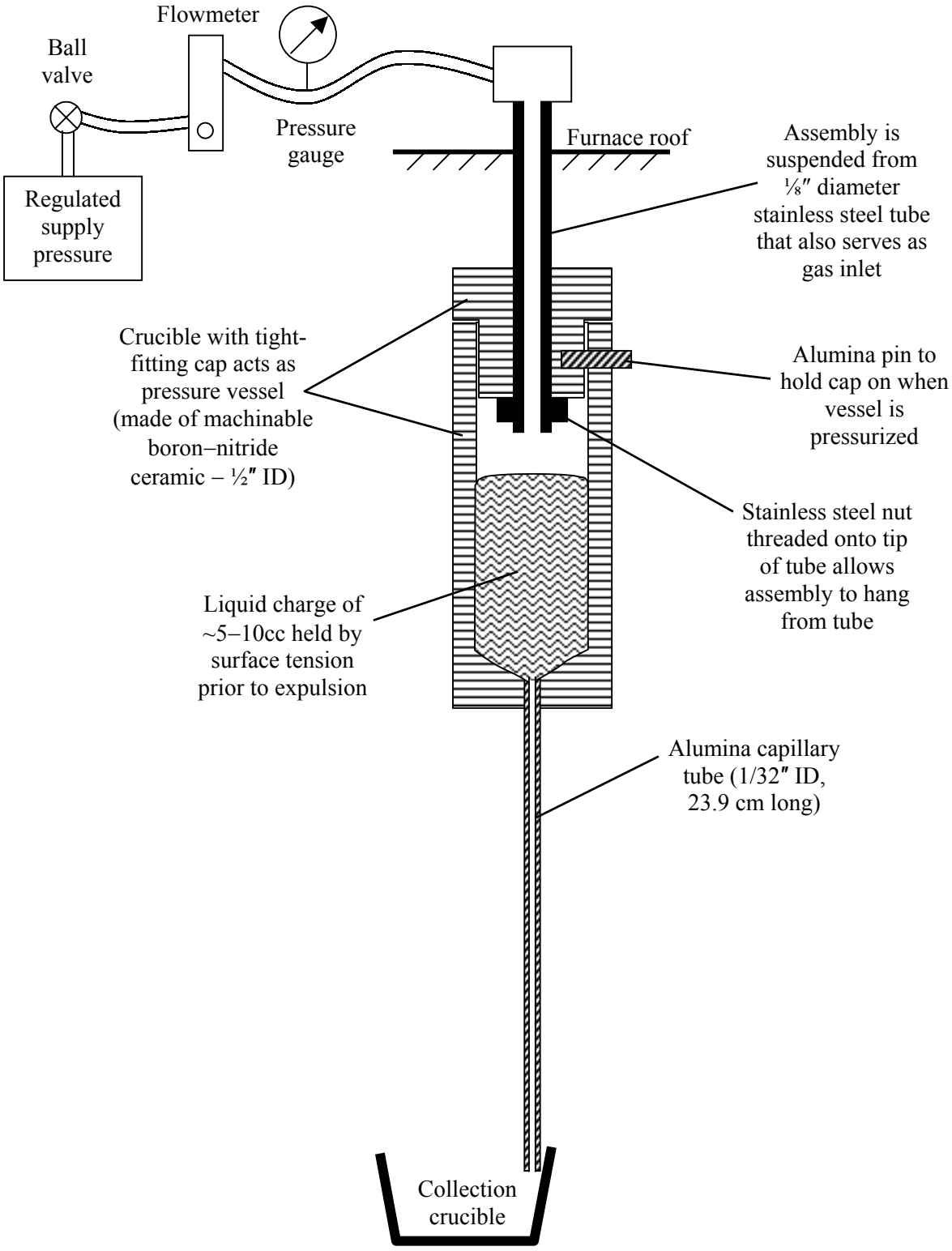

Figure F.1: Apparatus for measurement of viscosity of liquid metal.

This apparatus designed for the measurement of viscosity by the capillary method is very simple and fairly easy to construct, but requires careful selection of various design parameters to work properly. The crucible and capillary must be selected such that with no external pressure supplied, the surface tension of the liquid will be sufficient to prevent flow through the capillary. When the metal charge melts, the initial height in the crucible, h, must not allow the pressure due to gravitational head to exceed the capillary pressure:

$$\rho g h < \frac{4\gamma}{d} \tag{E.1}$$

where ρ is the liquid density, γ is the surface tension of the liquid and d is the diameter of the non-wetting capillary. To accommodate a large amount of metal, it therefore best to have a crucible with large cross-sectional area. For ease of construction and to minimize gas leakage, a crucible was machined from boron nitride with a ½″ inner diameter.

Next, the application of external pressure must be sufficient to drive the liquid into the capillary, but not too high that the flow becomes turbulent. For the measurement of eutectic liquid Ni–Si, the external pressure used was 2–5 psi, which fell within the appropriate range for the given capillary. The gas of 95% Argon / 5% Hydrogen was supplied from a low pressure regulator and rapidly introduced to the liquid metal in the pressure vessel by opening a ball valve and having a relatively small volume of gas that must change pressure (using small tube diameters). The time necessary for all of the liquid to flow through the capillary was determined by a marked increase in gas flow and a decrease in pressure once all of the liquid reached the collection crucible. The experimentally measured parameters for each experiment are the total mass of metal, m, time to flow through the capillary, t, and the pressure difference between the gas inside the vessel and ambient, ΔP_{gas}.

Several other factors affect the fluid pressure in addition to the pressure drop due to viscous drag. These must be accounted for before the viscosity is determined assuming Poiseuille flow.

$$\Delta P_{gas} - \frac{2\gamma}{r_{crucible}} + \rho g\left(\frac{h}{2} + L\right) - \rho\frac{V^2}{2} = \frac{128\mu L m}{\pi d^4 \rho t} \tag{E.2}$$

The second term corresponds to the small difference in pressure across the gas/liquid interface where $r_{crucible}$ is the radius of the crucible. The third term is the additional driving force due to the gravitational head of the liquid column where L is the length of the capillary and h is given by $m/\rho\pi r_{crucible}^2$. The fourth term is the pressure drop associated with accelarating the fluid as it enters the capillary, where V is the velocity of the liquid inside the capillary, given by $4m/\pi d^2\rho t$.

Because the calculation of viscosity is very sensitive to the diameter of the capillary, the apparatus was calibrated using water at room temperature to accurately determine the appropriate diameter for subsequent calculations. A pin was used to block the capillary tube prior to pressurizing the chamber because water wet the capillary and would have otherwise leaked. The water was at 23°C, corresponding to the fluid properties, $\gamma = 0.073$ N/m, $\rho = 0.997$ g/cc, and $\mu = 0.962$ mPa-s. The capillary diameter determined by the calibration was $d = 0.031''$, almost identical to the nominal 1/32″ ID specification. Variation was +/- 5% between the tests at different supply pressures.

Mass (g)	ΔP_{gas} (Pa)	Time (s)	$4\gamma/r_{crucible}$ (Pa)	$\rho g(h/2+L)$ (Pa)	$\rho V^2/2$ (Pa)	μ (mPa-s)	Reynolds number
9.013	7129	22.77	23	2688	331	0.943	678
9.647	7060	23.99	23	2712	342	0.923	704
9.79	7060	24.54	23	2718	337	0.932	692
8.818	7129	22.16	23	2680	335	0.937	687
9.208	7060	23.00	23	2695	339	0.926	699
9.262	12845	15.56	23	2698	749	0.978	984
9.804	12845	16.22	23	2719	772	0.963	1015
9.191	12845	15.2	23	2695	773	0.961	1017
9.62	12845	16.15	23	2711	750	0.979	984
9.686	12845	15.98	23	2714	777	0.960	1021
9.436	19347	11.58	23	2704	1404	0.998	1321
9.913	19347	12.43	23	2723	1345	1.023	1260
9.952	19485	12.12	23	2724	1426	0.996	1332
9.432	19278	11.66	23	2704	1384	1.003	1305
9.588	19209	12.02	23	2710	1345	1.015	1270

Table F.1: Viscosity measurement of water used to calibrate the diameter of capillary tube.

Using the same capillary tube diameter and estimated fluid properties of eutectic liquid Ni–Si of $\gamma = 1.4$ N/m and $\rho = 7.6$ g/cc, the following results were obtained. Note the density used for these calculations is slightly higher than the 7.2 g/cc used elsewhere — these calculations were done prior to careful analysis of the liquid density.

Mass (g)	ΔP_{gas} (Pa)	Time (s)	$4\gamma/r_{crucible}$ (Pa)	$\rho g(h/2+L)$ (Pa)	$\rho V^2/2$ (Pa)	μ (mPa-s)	Reynolds number
37.17	17306	34.32	441	19263	325	10.2	172
52.4	28407	37.02	441	19852	556	10.2	224
46.94	30890	33.61	441	19641	541	10.8	208

Table F.2: Viscosity measurement of liquid Ni – 11.3 wt% Si at 1200°C.

Bibliography

[1] Emanuel Sachs, *et al*: "Production of injection molding tooling with conformal cooling channels using the Three Dimensional Printing process" *Polymer Engineering and Science*, 2000, Vol. 40, No. 5, pp. 1232-1247.

[2] K. A. Thorsen, S. Hansen and O. Kjaergaard: "Infiltration of Sintered Steel with a Near-Eutectic Fe-C-P Alloy" *Powder Metallurgy International*, 1983, vol. 15, no. 2, pp. 91-93.

[3] S. Banerjee, R.Oberacker and C.G. Goetzel: "Experimental Study of Capillary Force Induced Infiltration of Compacted Iron Powders with Cast Iron" Modern Developments in Powder Metallurgy, Vol. 16. Metal Powder Industries Federation: Princeton, NJ, 1984, pp. 209-244.

[4] Merton C. Flemings: Solidification Processing, McGraw Hill: New York, 1974, pp. 219-239.

[5] Robert P. Messner and Yet-Ming Chiang: "Liquid-Phase Reaction-Bonding of Silicon Carbide Using Alloyed Silicon-Molybdenum Melts" *Journal of the American Ceramics Society*, May 1990, Vol. 73, No. 5, pp. 1193-1200.

[6] Yet-Ming Chiang, Robert P. Messner, Chrysanthe D. Terwilliger and Donald R. Behrendt: "Reaction-formed silicon carbide" *Materials Science and Engineering*, 1991, Vol. A144, pp. 63-74.

[7] Leszek Hozer and Yet-Ming Chiang: "Reactive-infiltration processing of SiC-metal and SiC-intermetallic composites" *Journal of Materials Research*, Sep 1996, Vol. 11, No. 9, pp. 2346-2357.

[8] H. Zhuang, J. Chen and E. Lugscheider: "Wide gap brazing of stainless steel with nickel-base brazing alloys" *Welding in the World*, 1986, Vol. 24, No. 9/10, pp. 200-208.

[9] F. Lenel, R. German, R. Heckel and P. Mirchandani: "Physical Fundamentals of Consolidation" Powder Metallurgy ASM Handbook Vol. 7, American Society of Metals: Metals Park, OH, 1984, pp. 308-321.

[10] Randall German: Powder Metallurgy Science, 2nd ed., Metal Powder Industries Federation: Princeton, NJ, 1994.

[11] S.F. Corbin: "Diffusion-Based Model for Isothermal Solidification Kinetics during Transient Liquid-Phase Sintering" *Metallurgical and Materials Transactions*, Jan 2002, Vol. 33A, pp. 117-124.

[12] H. Mehrer: Diffusion in Solid Metals and Alloys, Landolt-Bornstein New Series III/26, Springer-Verlag, pp. 1-29.

[13] Smithells Metals Reference Book, Seventh Edition, Edited by E.A. Brandes and G.B. Brook, Butterworth Heinemann: Oxford, England, 1992.

[14] G.H. Geiger and D.R. Poirier: Transport Phenomena in Metallurgy, Addison-Wesley: Reading, MA, 1980, pp. 473-496.

[15] Takamichi Iida and Roderick I.L. Guthrie: Physical Properties of Liquid Metals, Clarendon Press: Oxford, 1988, pp. 200,217.

[16] W.D. MacDonald and T.W. Eagar: "Isothermal Solidification Kinetics of Diffusion Brazing" *Metallurgical and Materials Transactions A*, Jan 1998, Vol. 29A, pp. 315-325.

[17] Alloy Phase Diagrams, ASM Handbook Vol. 3, American Society of Metals: Metals Park, Ohio, 1992, pp 2·318, 2·173, 2·110, 2·203.

[18] R.A. Tanzilli and R.W. Heckel: "Numerical Solutions to the Finite, Diffusion-Controlled, Two-Phase, Moving-Interface Problem (with Planar, Cylindrical, and Spherical Interfaces)" *Transactions of the Metallurgical Society of AIME*, Nov 1968, Vol. 242, pp. 2313-2321.

[19] James C. Baker and John W. Cahn: "Thermodynamics of Solidification" Solidification, American Society of Metals: Metals Park, Ohio, 1971, pp. 23-58.

[20] Merton C. Flemings: Solidification Processing, McGraw Hill: New York, 1974, pp. 263-288.

[21] Generated by Thermo-Calc, a Computational Thermodynamics program developed at the Royal Institute of Technology, KTH in Stockholm, using the Kaufman Binary Database.

[22] Isaac Tuah-Poku, M. Dollar, and T.B. Massalski: "A Study of the Transient Liquid Phase Bonding Process Applied to a Ag/Cu/Ag Sandwich Joint" *Metallurgical Transactions A*, March 1988, Vol. 19A, pp. 675-686.

[23] H. Kokawa, C.H. Lee and T.H. North: "Effect of Grain Boundaries on Isothermal Solidification during Transient Liquid Phase Brazing" *Metallurgical Transactions A*, July 1991, Vol. 22A, pp. 1627-1631.

[24] Y. Zhou, W.F. Gale and T.H. North: "Modelling of transient liquid phase bonding" *International Materials Reviews*, 1995, Vol. 40, No. 5, pp. 181-196.

[25] Kazuyoshi Saida, Yunhong Zhou and Thomas H. North: "Factors Affecting Isothermal Solidification during Transient Liquid Phase-Brazing of Nickel" *Journal of the Japan Institute of Metals*, 1994, Vol. 58, No. 7, pp. 810-818.

[26] Y. Nakao, K. Nishimoto, K. Shinozaki and C. Kang: "Theoretical Research on Transient Liquid Insert Metal Diffusion Bonding of Nickel Base Alloys" *Transactions of the Japan Welding Society*, April 1989, Vol. 20, No. 1, pp. 60-65.

[27] K. Ishizaki, S. Komarneni and M. Nanko: Porous Materials, Process Technology and Applications, Kluwer Academic Publishers: Boston, 1998, pp. 202-223.

[28] Annual Book of ASTM Standards Designation E 8 – 96a, American Society for Testing and Materials: Philadelphia, PA, 1997.

[29] W. D. Kingery, H.K. Bowen and D.R. Uhlmann: Introduction to Ceramics, Second Edition, John Wiley & Sons: New York, 1976, pp. 185.

[30] George W. Scherer: "Correction of "Drying Gels: I. General Theory"" *Journal of Non-Crystalline Solids*, 1987, Vol. 92, pp. 375-382.

[31] Donald A.Nield and Adrian Bejan: Convection in Porous Media, Second Edition, Springer-Verlag: New York, 1999.

[32] F.A.L. Dullien: Porous Media: Fluid Transport and Pore Structure, Second Edition, Academic Press, Inc: San Diego, CA, 1992, pp. 237-249.

[33] J. L. Lage: "The Fundamental Theory of Flow Through Permeable Media From Darcy to Turbulence" Transport Phenomena in Porous Media, Editors Derek B. Ingham and Ioan Pop, Elsevier Science Ltd: Oxford, UK, 1998, pp. 1-30.

[34] Stanley Middleman: Modeling Axisymmetric Flows: Dynamics of Films, Jets and Drops, Academic Press, San Diego, 1995, pp. 211-240.

[35] Adrian E. Scheidegger: The Physics of Flow through Porous Media, Third Edition, University of Toronto Press: Canada, 1974.

[36] George B. Thomas, Jr. and Ross L. Finney: Calculus and Analytic Geometry, 8th Ed., Addison-Wesley: Reading, MA, 1992, pp. 330,354.

[37] Peter J. Heinzer: "Permeametry" Powder Metallurgy, ASM Handbook Vol. 7, American Society of Metals: Metals Park, Ohio, 1984, pp. 263-265.

[38] "Operating Instructions for Rosano™ Surface Tensionometer", by Roller-Smith, Part no. 198120. Biolar Corporation: North Grafton, MA.

[39] Takamichi Iida and Roderick I.L. Guthrie, The Physical Properties of Liquid Metals, Clarendon Press: Oxford, 1988, pp. 47-77, 109-198.